AN EXPERIMENTAL STUDY OF FLAME LENGTHS AND EMISSIONS OF FULLY-MODULATED DIFFUSION FLAMES

by

James E. Usowicz

A Thesis

Submitted to the Faculty

of the

WORCESTER POLYTECHNIC INSTITUTE

in partial fulfillment of the requirements for the

Degree of Master of Science

in

Mechanical Engineering

by

May 2001

APPROVED:

Dr. James C. Hermanson, Major Advisor

Dr. Hamid Johari, Co-Advisor

Dr. Nicholas Dembsey, Fire Protection Engineering

Dr. Nikolaos Gatsonis, Graduate Committee Representative

Abstract

A pulsed fuel injector system was used to study flame structure, flame length, and emissions of ethylene jet diffusion flames over a range of injection times and duty-cycles with a variable air co-flow. In all cases the jet was completely shut off between pulses (fully-modulated) for varying intervals, giving both widely-spaced, non-interacting puffs and interacting puffs. Imaging of the luminosity from the flame revealed distinct types of flame structure and length, depending on the duration of the fuel injection interval. Flame lengths for isolated puffs (small injection times) were up to 83% less than steady state flames with the same injection velocities. With the addition of co-flow flame lengths grew to a maximum of 30% longer than flames without any co-flow. A scaling argument is also developed to predict the amount of co-flow that gives a 15% increase in mean flame length. Interacting flames with a small co-flow and small injection times (t_i = 5.475 ms) experienced flame length increases of up to 212% for a change in duty-cycle from a_{inj} = 0.1 to 0.5. For interacting flames with long injection times (t_i = 119 ms), essentially no change in flame length was noticeable over the same range of duty-cycles. Emission measurements suggest partial quenching of the reaction in isolated puffs with low duty-cycles and injection times ($t_i \leq$ 5.475 ms) resulting in high CO and UHC concentrations and low NO and NO_x concentrations. With an increase in duty-cycle, the puffs began to interact and CO and UHC concentrations decreased while NO and NO_x concentrations increased. For flames with $t_i \geq$ 5.475 ms emission concentrations seem to be reasonably constant, with a slight increase in NO and NO_x concentrations as the duty-cycle increased. Also the duty-cycle experienced in the vicinity of the probe is estimated and used as a scaling factor for the emission measurements.

Acknowledgements

First and foremost this work would not have been possible without support of advisors Dr. James Hermanson and Dr. Hamid Johari, whose guidance and support were crucial in the completion of this work. A special thanks goes to Dr. Ravikiran Sangras, whose background, support, and help with experiments was also significant in the successful completion of this research. Thanks also go to Dr. Nikolaos Gatsonis and Dr. Nicholas Dembsey for taking their time to serve on the thesis committee.

Many people across the WPI campus also deserve recognition for their willingness to help in this project: W.P.I. Fire Science Laboratories (Scott Ayers and Dr. Nicholas Dembsey), M.E. Department (Barbara Furman), M.E. Shops (Steve Derosier, Bob Taylor, Todd Billings, and Jim Johnston), and the E.E. Shop (Gary). Additional thanks goes to Frank Weber, Ken Desabrais, and Nate Demmons for their advice and support during this research.

The financial support from The Microgravity Research Division of NASA (Cooperative Agreement NCC3-673) is gratefully acknowledged as well as advise and support from Mr. D.P. Stocker and Dr. U.G. Hegde.

Finally, I would like to thank my family and friends, whose support and understanding throughout my time at W.P.I. is greatly appreciated.

Table of Contents

List of Tables

CHAPTER 2

CHAPTER 3

CHAPTER 6

List of Figures

CHAPTER 2

CHAPTER 3

CHAPTER 4

CHAPTER 5

CHAPTER 6

APPENDIX A

APPEDNDIX B

APPENDIX C

APPENDIX D

APPENDIX E

Nomenclature

English Symbols

A_d	Jet exit area
a	Slope of flame length increase
d_{jet}	Jet exit diameter
F	Air / Fuel ratio
F_B	Total buoyancy of flame puff
f	Pulsing frequency
g	Gravitational constant
g'	Effective gravitational constant or $g(1-T_a / T_{puff})$
H	Idealized pulse cylinder height
k	Experimental constant for co-flow scaling argument
L	Flame length
N_D	Total number of dry moles
N_W	Total number of wet moles
P	Pulse parameter
P'	Pulse parameter combined with stoichiometric ratio
Re_{cof}	Co-flow Reynolds number
Re_{jet}	Jet exit Reynolds number
r	Puff radius
S_F	Celerity of a flame
S_T	Celerity of a thermal
s	Puff celerity or speed
T_a	Ambient temperature
T_{puff}	Flame puff temperature
U_{cl}	Centerline velocity
U_{cof}	Co-flow velocity
U_{jet}	Jet exit velocity
u	Measured puff velocity
V_o	Jet injected volume per pulse
V_T	Total injected volume over 1 second
d_{honey}	Honeycomb cell size
z	Axial distance along jet

Greek Symbols

α_{act}	Duty-cycle relevant to probe
$\alpha_{Calculated\ Speed}$	Duty-cycle determined from analytically calculating pulse speed
$\alpha_{Frame\ Method}$	Duty-cycle determined from frame counting method
α_{inj}	Pulse injection duty-cycle
$\alpha_{Measured\ Speed}$	Duty-cycle determined from measuring pulse speed
Δt_1	Injection pulse time
Δt_2	Probe pulse time
δ	Puff diameter

C_{CO_2D}	Dry carbon dioxide molar fraction
C_{iW}	Wet molar fraction of species i
$C_{i15\%}$	Molar fraction of species i at 15% oxygen
C_{O_2D}	Dry oxygen molar fraction
C_{O_2M}	Measured oxygen molar fraction
P	Interaction parameter
p	Pi (3.14159)
t_{CS}	Flame-on time from calculating pulse speed
t_{FM}	Flame-on time from frame counting method
t_i	Pulse cycle injection time
t_{MS}	Flame-on time from measuring pulse speed
t_o	Pulse cycle off time
t_T	Total pulse cycle time
r_{jet}	Cold jet gas density
r_a	Co-flow air density
r_{puff}	Flame puff hot density
Y	Stoichiometic constant
x_L	Buoyancy parameter

1. Introduction

Pulsed combustion has the potential for high combustion and thermal efficiencies, excellent heat transfer characteristics and low CO, NO_x and soot emissions.[1] With these characteristics pulsed combustion has a wide variety of practical applications including domestic furnaces, hot water heaters, industrial dryers, and waste incinerators. A significant amount of research has been performed on pulse combustors, including examination of the overall system characteristics, such as heat transfer, efficiency, frequency of operation, and pollutant formation.[2]

Most pulsed combustors studied to date involve the premixing of fuel and air prior to the entering the combustion chamber.[3] In some of these practical pulsed combustors, such as the well known Helmholtz combustor, the fuel and air enter through separate valves, which control the supply of reactants to the combustor.[4] In all pulsed combustors there is a strong coupling between the combustion processes and the acoustic field due to flapper valves that pulse the fuel air mixture. The fluid mechanics of the process are further complicated by the confinement due to the combustor chamber walls, thus leading to a fundamentally different problem than free (open air) flames. Both the acoustic coupling and confinement effects experienced in these combustors make the fundamental fluid mechanics governing the flow very difficult to understand. In recent years the understanding of the fundamental fluid mechanics behind these processes have been of interest and is a central focus of the current effort.

1.1 Background

Much of the research conducted in unsteady reacting and non-reacting jet flows to date has involved direct forcing of the jet with a specified acoustic input. In isothermal jets, such forcing has been shown by many researchers to result in increased spreading rates and enhanced mixing over unforced jets.[5-7] These studies show that noticeable changes in non-reacting jet growth and entrainment can be affected even at relatively low pulsation frequencies (of the order of 10 Hz). The effects of acoustic forcing have been seen as far out as seventy nozzle diameters downstream, with an increase in local entrainment of as much as a factor of three.[8] In addition to non-reacting jets, turbulent flames have also been seen to be sensitive to acoustic-level pulsing of the fuel stream.[9] Forcing with low frequency (again approximately 10 Hz) can produce a strong coupling with the buoyant structure in the far field, with a significant impact on the flame length and fuel/air mixing. Other research involving acoustic excitation or feedback has been conducted with both non-premixed and premixed flames in ramjets,[10] pulsed combustors,[4,11] and other ducts.[12,13] Each of these combustor configurations is, however, characterized by a strong coupling between the combustion process and the acoustic field.

A fundamentally different approach to unsteady combustion is to fully-modulate the fuel jet flow, that is, to completely shut off the fuel flow between pulses. This type of flow control can give rise to drastic modification of the combustion and flow characteristics of flames, leading to enhanced fuel/air mixing mechanisms not operative for the case of acoustically excited or partially-modulated jets.[14,15] Although full modulation of the flow can be realized in pulsed combustor configurations,[4,16] this pulsing is necessarily accompanied by the very strong acoustic coupling noted previously, the properties of which (such as frequency) are strongly facility-dependent and can be difficult to vary over a wide range without hardware modification.

Flame tests that exclude acoustic coupling or other confinement effects have been conducted and these works represent a useful step towards understanding the complicated combustion behavior in pulsed combustion systems. Experiments on unconfined, widely separated buoyant fuel puffs by Johari & Motevalli[14] showed a decrease in mean flame length of fully-modulated flames of up to 70% compared with a steady, turbulent jet at low Reynolds number ($Re_{jet} \approx 2000$). That work examined not only the effects of pulsing frequency on flame length and structure but also those due to the duty-cycle (i.e., the jet-on fraction of each pulsation cycle). Also developed in that work was a dimensionless parameter that characterizes the effect of the duty-cycle:

$$\Pi = V_O^{\frac{2}{3}} \left(\frac{\left(1 - \alpha_{inj}\right)}{A_d \alpha_{inj}} \right), \qquad \textbf{(1.1)}$$

where A_d is the fuel exit area, V_o is the injected fuel volume, and α_{inj} is the duty-cycle. This parameter characterizes the transition from isolated puff behavior to ‘interacting’ puff behavior[14] where puffs do not completely burn out before another puff of fuel is injected. This parameter was developed by relating the convection time scale of the injected fuel puffs in the near-nozzle region to the interval between the pulses. It should be noted that this parameter was only intended to characterize whether structures can be considered interacting or not, not to predict either the resulting value of the flame length or the rate of the fuel/air mixing.

Subsequent work by Hermanson *et al.*[15] demonstrated a flame length reduction of fully-modulated flames of approximately 50% for Reynolds numbers of up to Re_{jet} = 20,000. This work also revealed two distinct types of flame structures for fully-modulated flames. For short injection times (small injected volume), puff-like flame structures with a roughly spherical shape and a very short flame length were observed. For relatively longer injection times, more elongated flames resulted. The flame lengths of the elongated flames were generally comparable to those of the corresponding steady-state cases.

The transition from compact, puff-like to elongated flame behavior can be characterized in terms of the parameter

$$P \equiv \left(\frac{H}{d_{jet}}\right)^{\frac{1}{3}} = \sqrt[3]{\left(\frac{t_{inj}U_{jet}}{d_{jet}}\right)} = \sqrt[3]{\frac{4V_O}{p\,d^3}}, \qquad \textbf{(1.2)}$$

where H is the height of the injected slug (as described in Fig. 2.1), and d_{jet} is the exit jet diameter. This parameter was developed[15] by taking the volume of injected gas to be a cylinder having the same volume as that of the injected fuel and with a base diameter equal to the nozzle diameter, d_{jet}. The height of the cylinder, H, is computed by dividing the total volume of gas injected by the nozzle exit area. The aspect ratio of this volume, H/d_{jet}, can reasonably be expected to be related to whether a fully-modulated flame puff will be compact, or more elongated in structure. By comparing the visual description of the pulsed flames with their characteristic P value, it is possible to correlate elongated structures with large values of P (long cylinders) and puff-like structures with small values of P (flat cylinders). Generally, puff-like behavior is seen for values of P less than approximately $P = 8$ for ethylene/air flames. In addition, for isolated, puff-like structures, the parameter P is directly related to the mean flame length, since the latter has been shown previously[14,15] to scale with the cube root of the injected volume. Temperature measurements also made by Hermanson *et al.*[15] suggested that the temperature associated with the puff-like flame structures rises more rapidly with downstream distance than for the corresponding steady-state flame. The temperature characteristics of the elongated structures were more similar to those of the steady-state flame.

1.2 Current Work

The focus of the current work is the extension of previous research in fully-modulated, turbulent, diffusion flames to include the effects of an air co-flow of variable strength, duty-cycle effects with a small co-flow, and emissions measurements to help characterize the fuel/air mixing in these flames. This is part of a larger study by WPI and NASA Glenn Research Center of fully-modulated, turbulent, diffusion flames under microgravity conditions. The overall goal of that effort is to improve the fundamental understanding of turbulent diffusion flames (both steady and pulsed) by removing the impact of buoyancy on the development of fluid instabilities and the subsequent formation, evolution, and interaction of the large-scale coherent structures that play a central role in fuel/air mixing. The importance of understanding the impact of co-flow on fully-modulated diffusion flames stems both from the need to be able to conduct experiments on a space platform in which the volume of oxidizer available may be strictly limited as well as to contribute to the understanding of configuration effects in pulsed combustion systems. The emission characteristics of the flames provides impartial information on the completeness of combustion and the fuel/air mixing.

The questions of interest for this investigation include: 1) what amount of co-flow is required to give a similar mean flame length for confined flames as is observed for free flames, 2) what is the impact of varying amounts of co-flow on the mean flame length and structure, 3) how does the addition of a co-flow effect duty-cycle changes in the flames, and 4) what are the concentrations of UHC, NO_x, CO, CO_2, and O_2 at the flame tip in flames over a range of injection times, duty-cycles, and Reynolds numbers.

For steady, turbulent diffusion flames, the strength of an air co-flow can potentially have a noticeable effect on the flame length.[17,18] As the strength of the co-flow is increased, for a given jet velocity, the flame tends to spread slower[17] and the combustion length can increase.[18] Dahm & Dibble,[19] in the context of the examination of co-flow effects on flame blowout, related the growth and entrainment characteristics of turbulent jet diffusion flames with co-flow to those of non-reacting jets. Using non-reacting jet data[20] they illustrated that steady flames become more wake-like with increasing co-flow, leading to a slower rate of flame spreading.

Emissions for steady, turbulent diffusion flames in open air have previously been studied for a variety of fuels. For ethylene flames with an $Re_{jet} \approx 5{,}000$ and $d_{jet} = 5$ mm, Turns & Bandaru[21] found CO emissions to be around 33.7 ppm and CO_2 production at 3.74% both at a 15% O_2 concentration. Turns[22] also reported for flames with similar injection parameters NO_x production on the order of 32 ppm. Emission measurements and effects of co-flow for the case of fully-modulated jet flames have not yet been fully established.

2. Experimental Apparatus

The experimental apparatus in the work consisted of a co-flowing combustor combined with different diagnostic techniques. Flame length and structure information were obtained using a CCD camera and image processing computer. Emissions were determined using a wide range of emissions equipment, which include a collection probe, sample and vacuum pumps, and emission analyzers. Each of these systems are described in detail in the following sections.

2.1 Combustor

The combustor setup consisted of a single fuel nozzle attached to a fast response solenoid centered in a square duct (20 × 20 cm in cross section) through which co-flow air was supplied, as shown schematically in Figs. 2.2 and visually in Fig. 2.3. Both the co-flow section and the injector sections are described in detail in the following subsections.

2.1.1 Fuel Injector Section

The fuel gas nozzle consisted of a 2 mm inner diameter stainless steel tube with a length to diameter ratio of 38. The solenoid was positioned in the center of the combustor by plumbing the fuel line through the center of the plenum section. Stainless steel was used for the fuel line piping material inside the combustor and a combination of brass and stainless steel was used outside of the combustor.

An electrically heated *Kanthal* wire coil of 0.24 mm diameter situated within one nozzle diameter of the nozzle exit served as a continuous ignition source. A special support was designed to hold the ignition wire in place and to allow power to be supplied to the ignition wire, while positioned in the center of the combustor. Power was supplied to the igniter via a 0-100 % Variac, which had an input voltage of 120VAC. Details of the igniter are shown in Appendix B.

A fast-response solenoid valve (Parker Hannifin Series 9) was used to modulate the fuel flow. The nominal response time of the valve was approximately 500 μs. In all cases the jet was fully-pulsed, that is, 100% modulated, at frequencies of up to 220 Hz. The valve cycling was controlled by a Parker Hannifin Iota One control unit**.** The actual gas discharge during the injection interval was somewhat different from the square wave solenoid input produced by the timing circuit due largely to the hydraulic response of the system. The unsteady flow characteristics of the injector system were surveyed using a hot-wire placed immediately downstream of the nozzle exit. The hot-wire anemometer signal was sampled at 6 kHz and low-pass filtered at 3 kHz. Fig. 2.4 shows an ideal pulse cycle where the flow is completely shut on and off and Fig. 2.5 shows actual traces of the measured velocity, U_{jet}, versus time for two different injection times. Since the span of the hot wire in fact exceeded the diameter of the jet nozzle exit, the velocity recorded by the hot wire was somewhat lower than the actual mean nozzle velocity.

The velocity traces indicate a certain amount of velocity overshoot at the beginning of each pulse and show that the trailing end of each pulse was often accompanied by flow oscillations. For the longer injection time ($t_i = 40\ ms$), a reasonable approximation to the desired square-wave injection velocity profile was achieved. For injection times greater than 6 ms, the injected volume associated with the overshoot and oscillations amounted to not more than 3% of the total. The hot wire data also indicate that the average velocity (and Reynolds number) during injection was not greatly impacted by the length of the injection interval for a given supply pressure.

The actual value of the jet injection velocity was determined using a FMA 1700/1800 series OMEGA mass flow meter under steady flow conditions. Since the pulses were repeatable and sufficiently close to a standard square wave the pulse flow conditions were set from an in-line pressure measurement that was determined under steady flow conditions. For example, if an in-line pressure of 40 psig was found for a steady flow of Re_{jet} = 5000, then a pressure setting of 40 psig would be set during the on time of the pulse cycle to obtain an Re_{jet} = 5000 for the pulse flow. Pressures could be set accurately to ± 1 psig and this was equivalent to a flow velocity accuracy of approximately 5%.

2.1.2 Co-flow Section

The co-flow section consisted of two sections, the flow conditioning section and the co-flow duct. The co-flow duct was 67 cm in length and had walls of glass to facilitate flow visualization. The co-flow conditioning section was 34.8 cm in length and was constructed mainly of aluminum in order to give the combustor a rigid base. Co-flow air was supplied to the combustor through a shop-air source, which passed through a 1-inch (2.54 cm) diameter PVC tube to with a rotameter and pressure gauge attached inline. To ensure the proper flow profile entered the rotameter ten diameters of straight tube were situated upstream of the rotameter. The PVC tube was constricted down to ½ inch (1.27 cm) copper tubing which was routed around the combustor to inject air into the combustor bottom from four points, one in the midpoint of each side. Special attention was paid to the lengths of copper tubing used so that there was a fairly even distribution of air flowing into each of the four ports. A honeycomb/screen combination and two perforated plates were situated upstream of the injection nozzle, as shown in Fig. 2.2, with the distance between the nozzle and the top surface of the honeycomb held at 4.1 cm. The honeycomb used had a mesh size of d_{honey} = 0.125 in (0.3175 cm) and the screen had a mesh size of 40 per linear inch. Both were constructed out of stainless steel. The perforated plates had hole diameters of 0.125 inches (0.3175 cm) and an open area of about 60 percent. The absence of a contraction is unorthodox, but was necessary since the next stage of these experiments will be completed on a microgravity platform at NASA Glenn Research Center, where space limitations preclude a more conventional contraction setup. By using the unconventional method of only perforated plates, screen, and honeycomb it was possible to match the flow conditions that will be seen on the microgravity platform.

Standard shop air and breathable air was used for the co-flow fluid. The flow velocities were controlled via an OMEGA FL7412 rotameter. Pressures were monitored downstream of the rotameter and the flows were corrected by using a standard rotameter correction factor based on these pressures.

To perform experiments for the free flame, the co-flow duct was removed and a flat plate mounted 5.3 cm below the jet nozzle exit as seen in Fig. 2.6. In this case the fuel jet was discharged into still laboratory air with no applied co-flow. The flame in this case was surrounded by a cubical screen enclosure 1.07 m on a side, to prevent room disturbances.

2.2 Flame Length Diagnostics

A schematic of the setup used for flame length measurements is shown in Fig. 2.7. The luminous flame emission was recorded visually using a commercial camcorder and Panasonic interlaced color CCD camera model WV-650CP at a framing rate of 30 frames per second. In the case of the CCD camera a Tamron wide angle lens was used and images were grabbed using a Mu-tech MV-1000-10 analog acquisition board with a

MV-1350 color module attached. The luminous portion of the flames corresponded to the presence of soot particles, which, in turn, can be roughly associated with the local reaction surfaces.[23] In order to reduce blooming in the images a shutter speed of 1/250 was used in combination with varying the lens aperture and the room lighting. Reflections were reduced by placing a thin sheet of aluminum painted black with high temperature paint on the inside of the back wall of the test section.

2.2.1 Uncertainty In Flame Length Measurements

The video images were used to qualitatively examine the flame structure and to quantitatively determine the flame length. For the fully-modulated flames, determining the flame length by identifying and locating the most extreme downstream parcel of the luminous flame is relatively more straightforward than in steady flames, where flame parcels become separated from the bulk flow in the flame tip region.[24] In order to determine an average value for flame length, typically approximately 30-150 images were analyzed for each injection case.

Determining the flame lengths by video imaging relies strongly upon the sooting nature of the flame and the framing rate of the video device. Flames with low injection times were not in a sooting state long enough to allow the video imaging to capture the final point of extinction. In addition, the camera was not synchronized with the fuel injection cycle, thus the individual images were sampled at different stages of puff development. The case that was effected the most by these limitations was the case of $P = 4$ due to a very small injection time of $t_i = 5.75$ ms. The $P = 4$ flames were not very sooty and were visible only for three frames or less in each cycle, corresponding to a maximum of 120 ms. However, the quantitative value of flame length in all cases except

P = 4 is reasonably consistent with the previous results of Hermanson et al.[15] (see Fig. 4.5) for which case all flames were strongly sooting. In any case, the sooting/non-sooting characteristics of the flames did not appear to be strongly impacted by the strength of the co-flow in these experiments and the visual measurements provide a reasonable estimate of the relative effects of co-flow on the mean flame length. The mean flame length measurements were made with a ruler with the lowest increment of 0.25 inches, so measurement could be made to ±0.125 inches. With this scale the measurement uncertainty was estimated to be ±4% for P = 4, ±1.5% for P = 6, ±1% for P = 4, ±8% for P = 4, and ±0.6% for P = 11, 15, and steady flames.

General fluctuations in the flame length due to the nature of the flames were another source of error. Table 2.1 shows the random flame length uncertainty for non-interacting flames and Table 2.2 shows random flame length uncertainties for interacting flames.

Table 2.1: Non-interacting flame length uncertainties

Re_{jet} = 3,000		Re_{jet} = 5,000	
P	**% Error**	***P***	**% Error**
4	7.02	4	6.71
6	4.37	6	5.09
8	4.56	8	4.53

Table 2.2: Interacting flame length uncertainties

$P = 4$		$P = 6$		$P = 8$		$P = 11$		$P = 15$	
a_{inj}	% Error	a_{inj}	% Error	a_{inj}	% Error	a_{inj}	% Error	a_{inj}	% Error
0.10	5.14	0.10	4.20	0.10	4.64	0.10	4.78	0.10	6.22
0.17	5.55	0.17	5.86	0.17	4.93	0.17	3.08	0.17	6.53
0.23	7.57	0.23	6.77	0.23	4.32	0.23	3.67	0.23	6.34
0.30	6.80	0.30	5.30	0.30	4.19	0.30	4.20	0.30	5.31
0.33	8.10	0.33	6.50	0.33	N/A	0.33	N/A	0.33	N/A
0.40	8.20	0.40	6.70	0.40	5.5	0.40	3.10	0.40	5.91
0.50	6.30	0.50	4.60	0.50	5.5	0.50	4.17	0.50	7.63

2.3 Emissions Diagnostics

Five different species of emissions were measured and they included unburned hydrocarbons (UHC), nitric oxide concentrations including NO_x and NO, carbon monoxide (CO), carbon dioxide (CO_2) , and oxygen (O_2). Sampling was done with an uncooled stainless steel probe and a collection tube inside diameter of 3 mm. The modified test section had one side wall constructed out of aluminum with a slot milled down the centerline so the probe tip could extend into the test section and sample on the centerline of the flame. The probe was positioned ten probe diameters downstream of the maximum flame length for each flame series. This gave a consistent location to sample so dilution effects between the flame tip and the probe would be comparable for each flame case studied. Most flame lengths were measured as will be seen in later chapters, but for the cases that did not have measured flame length data, flame lengths were interpolated from known measurements. A series of brackets were used to allow the probe end to be moved vertically along the test section. This allowed sampling to be done at the set distance downstream of the measured flame tip.

Unburned hydrocarbons were measured using a flame-ionization gas analyzer (Series 8800, Baseline Industries). Ultra zero-air with a UHC concentration of less than

0.1 ppm was used to zero the analyzer and also as an oxidizer for the hydrogen flame. A span gas with 4650 ppm of UBHC mixed with an ultra–zero air base was used to span the analyzer. Readings were taken visually from a digital display on the machine. A schematic of the setup can be seen in Fig. B-1 in Appendix B.

To conduct NO_x and NO measurements a Model 10AR chemiluminescence analyzer, Thermo Environmental Instruments Inc., was used. Ultra-zero air was used to zero the analyzer and as the ozone production gas. A span gas of 30 ppm NO with a nitrogen base was used to span the analyzer. All fittings used for this setup were stainless steel and the tubing was made of Teflon so that NO would not be absorbed in the lines. Readings were relayed to a data acquisition system and data was sampled a 1 Hz. A schematic of this setup can be seen in Fig. B-2 in Appendix B.

A cone calorimeter containing a Servomex 1400 O_2 analyzer and Siemens Ultramat 22 CO and CO_2 analyzer were used to make CO, CO_2, and O_2 measurements. The Servomex analyzer had a range of 0 – 25% volume of O_2 and the Siemens analyzer had a range of 0 –10% volume for CO_2 and 0 – 3000 ppm for CO. The Servomex O_2 analyzer had a filter that scrubbed out all CO and CO_2 before the species entered the analyzer. Samples for each machine were filtered through a fiber filter to remove soot and then sent into a cold trap and dryerite to remove the moisture from the sample. The flames in this investigation did not produce significant amounts of soot in the exhaust. Analog outputs from both analyzers were connected to a data acquisition board and were recorded using LabView and sampled at 1 Hz.. Typical sample periods were about 100 seconds in duration with the reaction. The analyzers had a base response time of around 10 – 30 seconds, which was prolonged due to the amount of filters and tubing the flow needed to travel through, so the readings stabilized in about one minute at which point the data recording begun.

2.3.1 Emission Measurement Scaling

After the emissions data were collected, a series of corrections depending on the type of analyzer used were made. UHC, NO, and NO_x were collected wet (with water vapor present) and did not need to be corrected, but the remaining species needed to be corrected from dry to wet molar fractions. Also, since O_2 was collected by the Servomex analyzer, O_2 measurements needed to be corrected for having CO, and CO_2 scrubbed or filtered out. Finally, UHC, CO, and NO_x species were corrected to 15% O_2 concentrations, which are used as an industry standard for comparing emission level.

2.3.1.1 O_2 Correction For Scrubbing of CO and CO_2

The Servomex 1400 O_2 analyzer used to collect O_2, scrubbed out all carbon-based species in the flow. In this case the UHC, CO, and CO_2 that were present in the flow did not enter the analyzer and it was necessary to correct the measured O_2 values to account for this. Since UHC and CO concentrations were extremely low they were ignored and only CO_2 was taken into account. This scaling factor is determined by examining the mole fractions of the species in the combustion oxidation reaction with and without CO_2 involved. Oxygen was sampled dry so H_2O can be ignored along with trace species, CO, and UHC. The oxidation reaction is thus,

$$C_2H_4 + F\left(0.21O_2 + 0.79N_2\right) \rightarrow pO_2 + qN_2 + mCO_2 + hH_2O. \qquad \textbf{(2.1)}$$

From Eq. (6.1) dry molar fractions for O_2 (X_{O_2D}), O_2 (X_{O_2M}), and CO_2 (X_{CO_2D}) can be determined. These quantities are expressed below as,

$$\mathrm{X}_{O_2D} = \frac{p}{p+m+q}, \quad \mathrm{X}_{CO_2D} = \frac{m}{p+m+q}, \ and \quad \mathrm{X}_{O_2M} = \frac{p}{p+q}. \qquad \textbf{(2.2a,b,c)}$$

These molar fractions can be combined and algebraically reduced to form an expression for the molar fraction of dry O_2 (X_{O_2D}), which is expressed by:

$$\mathrm{X}_{O_2D} = \mathrm{X}_{O_2M}\left(1-\mathrm{X}_{CO_2D}\right). \qquad \textbf{(2.3)}$$

This value is the dry molar fraction of O_2 and is used in order to correct the measured O_2 value to the dry O_2 value. This correction is small, but small changes in the O_2 concentration do have a significant effect on the overall analysis. These are dry molar fractions and the next step is to convert all dry concentrations to wet concentrations, as described in the following section.

2.3.1.2 Correction of Species to Wet Molar Fractions

The gas samples for all measurements except for UHC, NO and NO_x were dried to remove moisture as a requirement of the analyzers. It was desired to perform the final analysis of the species in wet molar form so dry concentrations needed to be converted to wet concentrations. In order to determine a universal expression for this correction the oxidation chemical reaction needed to be re-examined. Equation (2.1) implies that m = 2 and q = 4 to give the following expression,

$$C_2H_4 + F(0.21O_2 + 0.79N_2) \rightarrow 2CO_2 + 2H_2O + pO_2 + 0.79FN_2. \qquad \textbf{(2.4)}$$

From Eq. (2.4) the total number of moles on a wet and dry basis can be determined and are expressed as:[25]

$$N_W = m + \frac{q}{2} + p + 3.76F, \quad N_D = m + p + 3.76F. \qquad \textbf{(2.5a,b)}$$

These two relations can be reduced, after conserving elements, to further obtain a ratio of wet to dry, (total number of moles) (N_W/N_D), which can be expressed as:[25]

$$\frac{N_W}{N_D} = 1 + \frac{q}{2\left(4.76F - \frac{q}{4}\right)}, \quad where \quad F = \frac{m + \left(1 + \mathrm{X}_{O_2 D}\right)\frac{q}{4}}{1 - 4.76\mathrm{X}_{O_2 D}}. \qquad \textbf{(2.6a,b)}$$

Since the mole fraction ratio of dry to wet concentration is equivalent to the total mole ratio of dry to wet concentration an expression for the molar fraction of wet species can be formed and is expressed as:[25]

$$\mathrm{X}_{iW} = \frac{N_D}{N_W}\mathrm{X}_{iD}, \qquad \textbf{(2.7)}$$

where i represents the specific species being converted. This conversion can also be reversed in order to convert species from wet molar fractions to dry molar fractions. The conversion to 15% O_2 is also completed using the same idea of equating the molar fractions to the total number of moles in the reaction and is described next.

2.3.1.3 Correction of Species to 15 % O_2 concentrations

As an industry standard pollutant species measured in flames are usually converted to 15% O_2 concentrations. In this case CO, UHC, NO_x, and NO were converted to 15% O_2 concentration following a similar procedure as the correction from wet to dry concentrations.[25] An expression for this conversion can be determined by changing the subscripts slightly and an expression for this is shown below:[25]

$$\mathrm{X}_{i15\%} = \frac{N_{O_2 W}}{N_{O_2 15\%}}\mathrm{X}_{iW}. \qquad \textbf{(2.8)}$$

Where,

$$N_{O_2 W} = 4.76\left[\frac{m + \left(1 + \mathrm{X}_{O_2 W}\right)\frac{q}{4}}{1 - 4.76\mathrm{X}_{O_2 W}}\right] + \frac{q}{4}, \quad N_{O_2 15\%} = 4.76\left[\frac{m + \left(1 + \mathrm{X}_{O_2 15\%}\right)\frac{q}{4}}{1 - 4.76\mathrm{X}_{O_2 15\%}}\right] + \frac{q}{4}. \qquad \textbf{(2.9a,b)}$$

These relations can also be used to convert to any other percentage of O_2 by substituting the desired correction percentage value into Eq. (6.9b). A more detailed derivation of these relations for the conversion to dry or wet molar fractions and the conversion to 15% O_2 concentrations can be found in Turns.[25]

2.3.2 Uncertainty in Emission Measurements

In this section uncertainties in the measurements taken will be discussed. The concentrations of CO, CO_2, and O_2 were collected with a data acquisition program so very accurate readings could be obtained. The concentrations of UHC were recorded by reading a digital output connected to the analyzer. Emission measurements were also affected by the accuracy that the flame length could be measured, as discussed in Section 2.2.1.

For CO, CO_2, and O_2 concentrations the average percent error was found by computing the standard deviation of a data set then dividing it by the average value computed for that set. The table below shows average measurement percent errors for the concentrations of CO, CO_2, and O_2 for different P numbers.

Table 2.3: Errors For CO, CO_2, O_2, NO_x, and NO

P	O_2	CO	CO_2	NO_x	NO
15	0.08	20.23	4.63	3.11	4.23
11	0.07	21.24	5.31	3.74	5.25
8	0.09	14.82	5.16	3.85	4.89
6	0.09	6.34	4.09	4.16	4.34
5	0.08	9.91	4.17	3.89	4.40
4	0.10	5.53	4.13	6.27	4.82
3.5	0.10	5.82	3.21	3.91	5.06
3	0.21	6.59	3.37	4.26	7.69

As this chart indicates O_2 percent errors remain rather low throughout the cycling of P values, but errors for CO and CO_2 concentrations tend to rise with increasing P

values. This is consistent with the tendency of the standard deviations not to decline with lower values of average values seen in the higher *P* number cases. The Siemans CO and CO analyzer had an accuracy of about 0.04% for CO_2 and 0.2 ppm for CO. The Sevomex O_2 analyzer had an accuracy of around 0.1%.

For UHC, emission values were recorded off of a digital display on the front panel of the analyzer. It is estimated that the recorded values were accurate to about ± 1 ppm. Adding to this error was another 2 – 3 ppm from the sample pump due to the rubber baffles used inside. Obviously these errors will affect the results heavily for low measurements of emissions and much less for high measurements of emissions.

Probe positioning also had an effect on the uncertainty involved with the emission measurements. The probe position repeatability was approximately $\pm 2 - 3$ nozzle diameters, which corresponds to about ± 6 mm. The concentrations were found to vary with vertical distance above the flame tip. This variation was found to be about 12% over a range of five nozzle diameters (1 cm) for the unburned hydrocarbons.

2.4 Temperature Diagnostics

A 2 mm diameter metal shaft OMEGA type K thermocouple was used to obtain temperature data. The thermocouple was attached onto the side of the emissions probe and was positioned approximately 1 cm upstream of the emissions collection tube. The response time of the thermocouple was 200 ms and data was captured with a data acquisition card and sampled at 1 Hz. Measurement errors ranged from 1.5% to 5.45%. Temperatures were recorded as mean temperatures and no radiation corrections were made.

3. Experimental Conditions

There were a large number of flow characteristics that could be varied in these experiments and they included, but were not limited to t_i, a_{inj}, V_o, and U_{cof} / U_{jet}. The injection time or "on time" is represented by t_i and was held constant for each P number and Re_{jet} used. Essentially this parameter controls the amount of injection volume, V_o, injected each pulse cycle. The injection duty-cycle (a_{inj}) and pulse injection time (t_i) were constant for a given flow condition with the off time defined in respect to the injection parameters. The parameter that defined the amount of co-flow used is U_{cof} / U_{jet}, which expresses the co-flow velocity over the injected jet velocity. This ratio could be changed either by changing the jet velocity or, more commonly, by changing the co-flow flow rate. A summary of selected test conditions may be found in the following section.

3.1 Fuel Jet

In this study the fuel was ethylene and in most cases was injected into a co-flowing stream of air. The exit conditions were standard temperature and atmospheric pressure. The injection Reynolds number, based on the velocity of the jet during the injection interval, the cold fuel viscosity and the exit nozzle diameter, was between $3{,}000 \leq Re_{jet} \leq 5{,}000$, which corresponds to $13.36 \leq U_{jet} \leq 22.26$ m/s.

The injection parameter P was in the range between 3 and 15 (P is infinitely large for a steady flame) with the duty-cycle a_{inj} varying from $a_{inj} = 0.0125$ to $a_{inj} = 0.5$. The duty-cycle is related to the injection frequency, f (0.5 Hz – 220 Hz), and injection time, t_i (2.42 ms – 304 ms), by $a_{inj} = t_i / (t_i + t_o) = ft_i$. This implies, for example, that increasing the frequency for a fixed injection time directly leads to an increase in the value of the duty-cycle. With a change in the duty-cycle there is an inherent change in the off time, t_o, of the pulse. Changing these conditions has dramatic effects on the flames studied and will be discussed in detail in the results section. The tables below show for two different Reynolds numbers and duty-cycles run, (where a_{inj} = 0.05 and 0.3) the corresponding values of V_o, V_T, t_i, t_o, and U_{jet} for varying P numbers.

Table 3.1: Pulse characteristics for a_{inj} = 0.05

Re_{jet} = 3000 , U_{jet} = 13.36 m/s

P	t_i (ms)	t_o (ms)	V_o (cc)	f_i (Hz)	V_T (cc)
3	4.04	76.80	0.17	12.37	2.10
3.5	6.42	121.95	0.27	7.79	2.10
4	9.58	182.04	0.40	5.22	2.10
5	18.71	355.54	0.79	2.67	2.10
6	32.34	614.37	1.36	1.55	2.10
8	76.65	1456.29	3.22	0.65	2.10
11	199.25	3785.78	8.36	0.25	2.10
15	505.24	9599.55	21.21	0.10	2.10

Re_{jet} = 5000 , U_{jet} = 22.28 m/s

P	t_i (ms)	t_o (ms)	V_o (cc)	f_i (Hz)	V_T (cc)
3	4.04	76.80	0.17	12.37	3.50
3.5	3.85	73.13	0.27	12.99	3.50
4	9.58	182.04	0.40	5.22	3.50
5	18.71	355.54	0.79	2.67	3.50
6	32.34	614.37	1.36	1.55	3.50
8	76.65	1456.29	3.22	0.65	3.50
11	199.25	3785.78	8.36	0.25	3.50
15	505.24	9599.55	21.21	0.10	3.50

Table 3.2: Pulse characteristics for a_{inj} = 0.3

***Re_{jet}* = 3000 , *U_{jet}* = 13.36 m/s**					
P	***t_i (ms)***	***t_o (ms)***	***V_o (cc)***	***f_i (Hz)***	***V_T (cc)***
3	4.04	9.43	0.17	74.22	12.59
3.5	6.42	14.96	0.27	46.74	12.59
4	9.58	22.36	0.40	31.31	12.59
5	18.71	43.66	0.79	16.03	12.59
6	32.34	75.45	1.36	9.28	12.59
8	76.65	178.84	3.22	3.91	12.59
11	199.25	646.92	8.36	1.51	12.59
15	505.24	1178.89	21.21	0.59	12.59
***Re_{jet}* = 5000 , *U_{jet}* = 22.28 m/s**					
P	***t_i (ms)***	***t_o (ms)***	***V_o (cc)***	***f_i (Hz)***	***V_T (cc)***
3	2.42	5.66	0.17	123.78	21.00
3.5	3.85	8.98	0.27	77.95	21.00
4	5.75	13.41	0.40	52.22	21.00
5	11.22	26.18	0.79	26.74	21.00
6	19.39	45.24	1.36	15.47	21.00
8	45.96	107.24	3.22	6.53	21.00
11	119.48	278.79	8.36	2.51	21.00
15	302.96	706.91	21.21	0.99	21.00

These tables illustrate how the pulse characteristics change with P, Re_{jet}, and a_{inj}. These variables were changed depending on the particular test that was desired. In order to help give an understanding on how these parameters effect the current experiments four examples are described. If P is held constant and a_{inj} is varied from low to high it is expected that the flames will go from non-interacting state to an interacting state. If t_i is varied (which inherently changes P) and a_{inj} is kept low then the pulses are expected to be non-interacting for an entire range of P, which give individual pulses allowing the flame structure to be examined. When t_i, P, and a_{inj} are held constant and U_{cof} / U_{jet} is varied co-flow effects come into play and flame changes depending on the co-flow amount can be observed. If Re_{jet} is changed, t_i needed to be changed to keep P constant (the Reynolds number appears to have little impact on the flame characteristics for flames with $Re_{jet} > 3{,}000$). One other condition that needs to be highlighted is the steady jet condition. In this case the pulse technically had a duty-cycle of $a_{inj} = 1$, which means the valve is always open during a given time injection time. In this report for the purpose of graphical representation the steady state flames are expressed as $\alpha_{inj} = 0.6$, $a_{act} = 1$, and $P = 16$..

3.2 Co-Flow

In this study the co-flow used was standard compressor air mixed in with breathable air from compressed gas cylinders when flow rates above $U_{cof} / U_{jet} = 0.015$ were desired. Co-flow strengths were generally referred to as co-flow to fuel velocity ratios or U_{cof} / U_{jet}. These ratios varied from $0 \le U_{cof} / U_{jet} \le 0.035$ depending on the particular test conducted. Appendix C contains a table that shows the velocity ratios and their corresponding co-flow flow rates for three different jet Reynolds numbers. For the case where the co-flow duct was in place but no co-flow air supplied, the air required for combustion was drawn in through the combustor exit. In order to test free flames the co-flow duct was removed and the flame entrained air from the surroundings, as mentioned previously.

The turbulence levels and mean velocities in the co-flowing stream were surveyed using a Dantech 2 axis LDV system (Laser Doppler Velocimetry). LDV surveys of the co-flow indicated a wake velocity defect of 25% in the immediate vicinity of the nozzle, and an overall turbulence level of less than 5% at a location 2 cm downstream of the nozzle exit. The LDV velocity trace of this defect is shown in Fig. 3.1. Since the jet exit velocity exceeds the maximum co-flow velocity in all cases by at least a factor of 50, the co-flow turbulence level is not believed to have a significant effect on the behavior of the flame.

3.3 Buoyancy Effects

An important consideration in the case of fully-modulated diffusion flames is whether the flow is buoyancy or momentum-driven. The scaling laws for the velocity decay in buoyancy-driven cases differs significantly from the momentum-driven case, even in the limit of small heat release. Following the scaling used by Becker &Yamazaki,[26] if the value of the parameter $x_L = (r_a d_{jet} g / r_{jet} U^2_{jet})^{1/3} (L / d_{jet})$ for a steady diffusion flame is less than approximately 2, the flame is momentum-driven and when it is greater than roughly 10, it is buoyancy-driven. Here r_a and r_{jet} are the density of the co-flow and the jet fuel, respectively, g is the gravitational acceleration, L is the flame length, and d is the jet nozzle diameter. For the steady flames in the present experiments $x_L \approx 8.4$, thus indicating that the steady flames are likely primarily buoyancy-driven. This argument would not be expected to necessarily hold for fully-modulated flames. It has been argued[15] that in these flames, if anything, the transition to momentum-dominated flow would require significantly lower values than $x_L = 2$ owing to the loss of jet momentum due to the rapid entrainment and mixing of ambient air that occurs for widely-spaced puffs. Similar reasoning suggests that the transition to the fully buoyancy-dominated regime is complete for values of x_L less than 10. Alternatively, a Richardson number can be determined based on the average buoyancy within the puff (from temperature measurements), the puff diameter, and the puff celerity. This calculation was performed for puffs in an earlier study,[15] and the resulting values of the Richardson number were around unity, indicative of the puffs being fully buoyancy-driven. Therefore, we expect that the majority of the flames considered in the results of this study are buoyancy-driven.

4. Isolated Flame Puff Results

This section describes fully-modulated flames that are non-interacting, which means that each flame has sufficient time to completely burn out before the next flame is injected. The compactness of a puff is related to the injection parameter expressed by Eq. 2.1. For C_2H_4 fuel, puffs are considered to be compact for $P \leq 8$ and elongated or steady flame like for $P \geq 9$.[15]

As mentioned previously a co-flow will be used to ventilate these flames on a space platform where the amount of co-flow used is critical and the smallest amount is desired. It is however important that the co-flow ventilation be sufficient to ventilate the flame by providing enough fresh oxidizer to the combustion process so flames can burn uninhibited by the by-products left in the combustion chamber. Since a small combustor is also desired for a space platform the co-flow also ensures that the flame does not contact the combustor walls. The co-flow must also be sufficiently weak so the flame structure dos not change from the ideal free flame or open air flame structure.

4.1 Flame Structure

Figure 4.1 shows a sequence of images exhibiting an unducted free flame puff with $P = 8$ from injection to extinction. The entire cycle lasts about 165 ms and is shown in 15 ms intervals. The camera used was only capable of imaging at 30 frames per second, but since the images were interlaced they were filtered and interpolated using video editing software in order to obtain 15 ms intervals. From left to right and top to bottom, frame 1 shows the igniter and the combustion chamber with no flame. Frames 2-5 show the injection period and the beginning of the pulse development. In frames 6-9 the injection period has just ended, the tail has just burned out, and the puff has lifted off the injection nozzle. In frames 10-12 the end of the pulse can be seen with the flame turning into a vortex ring structure as the last remnant to burn out. It should be noted that there is, especially for flames near flame burn-out, structure consisting of combustion products that is not visible.

4.1.1 Flame Structure with Constant Co-flow

Images of four representative flames (one steady and three fully-modulated) are shown in Fig. 4.2 for the case where the co-flow duct was present and a normalized co-flow velocity of $U_{cof} / U_{jet} = 0.005$ was supplied to the combustor. Figure 4.2a shows a steady turbulent flame; Figs. 4.2b-d show fully-modulated flames with three different injection times (P = 15, t_i = 303 ms; P = 8 t_i = 46 ms; P = 4, t_i = 5.75 ms). The steady flame exhibits the well-known fluctuations in flame length due to the burnout of large flame structures at the flame tip.[23] From the visual analysis of the fully-modulated flames, at least two distinct types of flame structure are apparent. For the relatively long injection time corresponding to Fig. 4.2b, an elongated flame structure is produced. In this case the flame is generally similar in appearance to the steady state flame, except for the flame tip region, where oscillations in flame length are generally not observed in this case. The burnout length of these flames is comparable to those for steady flames, as suggested by the figure. For shorter injection times (and smaller injection volume), the flame length becomes noticeably shorter than that of the steady flame. An example image is shown in Fig. 4.2c for an injection time of t_i = 46 ms or P = 8. In this case, a vortex structure is generally apparent in the region of the flame near the flame tip, with a “tail” attached to the trailing portion of the burning fuel puff. This is similar to the results observed previously for free flames.[15] For the case of the shortest injection time (Fig.

4.2d), the puff-like vortex structure typically exhibits a blue luminescence and appears to contain very little soot. Unlike the vortex region in this case, the tail region evidently contains considerably more soot, as indicated by a more intense, yellow-orange emission. The blue, relatively soot-free vortex structure was not observed in previous investigations of puff-like behavior with larger nozzle sizes and injection times, but with similar jet Reynolds number.[15] Johari & Motevalli,[14] however, did observe some regions of blue emissions for fully-modulated flames for sufficiently short injection times for a Reynolds number of approximately 2000.

4.1.2 Flame Structure with Varying Co-flow

Co-flow was added in increments giving velocity ratios from $0 \leq U_{cof} / U_{jet} \leq 0.026$ for $Re_{jet} = 5000$ and $0 \leq U_{cof} / U_{jet} \leq 0.045$ for $Re_{jet} = 3{,}000$ for flames with $P = 4, 6, 8, 11, 15$, and ∞ (steady state case). The flame structure was then examined to determine the effects of co-flow on the flames.

For steady flames, the addition of co-flow in the range of velocity employed here appears to have relatively little systematic effect on the flame, both in terms of the mean flame length and flame structure. There was a slight narrowing of the flame accompanied by a small increase in mean flame length that was less than 5%. For the fully-modulated flames, the effect of co-flow generally appeared to become proportionally more pronounced for lower values of the injection time (lower injection volume and smaller value of the parameter P).

Representative images of flame puffs for $P = 8$ with three different co-flow conditions are shown in Fig. 4.3a-c. Each image was taken near the jet cut-off point and it should be noted that the burn-out length of these flames is longer, but the flames are reasonably representative of the flame length in each case. The first image, Fig. 4.3a, shows a fully-modulated flame with no co-flow supplied. In this case, the necessary air for combustion was drawn in through the exit of the co-flow duct. The fully-modulated flame portrayed in the second image, Fig. 4.3b, had a co-flow strength of $U_{cof} / U_{jet} = 0.005$. The relatively longer flame length in the image is evident in comparison to the case without co-flow. Other than the change in flame length, there does not appear to be significant changes in the flame structure. Finally, the free flame (no co-flow duct attached see Fig. 2.6) for the same injection conditions is shown in Fig. 4.3c. For free flames, this value of P was shown to be within the "puff-like" regime, where the mean flame length scales linearly with the injection volume. The free flame appears generally similar in structure to the flames with co-flow (Fig. 4.3b), with a flame length comparable to the case without co-flow (Figure 4.3a). The flame for this condition is still strongly sooting, as expected.[15]

For the most compact, puff-like flames considered here (t_i = 5.7 ms, P = 4), however, two distinct changes in flame behavior are apparent. Three such flames are shown in Fig. 4.4a-c, again for the case without co-flow, for a co-flow, and a free flame. As for the case of P = 8 shown previously, the visible flame length is increased by the presence of the co-flow. However, in this case the flame structure also appears to be influenced by the co-flow, with the vortex structure evidently becoming lost as the amount of co-flow increases. For these short injection times, the leading region of the flame (approximately the upper half of the flame shown in Fig. 4.4b) remains relatively soot-free, while the tail region contains soot. The relatively soot-free region may be due to the very rapid mixing associated with a compact puff, which may not allow for a residence time sufficient for complete combustion or the generation of significant amounts of soot. Similar behavior is also observed for free flames, as can be seen in Fig. 4.4c. In each of these cases the oxidizing flow or entrainment is coming from two different sources. In Figs. 4.4a and c there is no co flow present so the entrainment air is coming from the ambient air that surrounds the flame, whereas in Fig. 4.4b the entrainment air is coming from the co-flow that has a vertical velocity component. For the more elongated pulsed flames (P = 11 and P = 15), relatively little change in flame length and flame structure compared with the corresponding flame without co-flow is apparent.

It should be noted that the images presented here are only single, representative images for each of the flames shown. To determine quantitatively the changes in mean flame length brought about by co-flow, multiple images were considered. The results of this analysis are presented in the following section.

4.2 Flame Length

A majority of the flame length measurements were made with a Panasonic CCD camera with only a few cases imaged with a standard video camera. Ensemble averages of between 30 and 75 flames were taken to determine an average flame length. The current results are compared against each other and with previous results for fully-modulated flames with larger values of d_{jet} and larger injected volumes. A scaling argument is also developed in this chapter to predict the amount of co-flow necessary for a given change in flame length.

4.2.1 Flame Length Scaling Comparison With Previous Results

The flame lengths of the ducted flames in this investigation were compared with results from previous work with fully-modulated free flames completed by Hermanson *et al.*[15] The measured average flame length, normalized by the nozzle diameter, is shown in Fig. 4.5 for fully-modulated flames with various co-flow strengths. The Reynolds numbers of the flames of Hermanson *et al.* were $3,500 \leq Re_{jet} \leq 20,000$. The case of the free flame, which has no co-flow and no duct, is included as a special case and used as the comparison set in this data. The x-axis is the parameter $P' = P(1 + y)^{1/3}$, where y is the air to fuel volumetric ratio at stoichiometric conditions. The scaling with the 1/3 power of y originates from a scaling argument developed for buoyant puffs,[14] and allows comparison between fully-modulated experiments using different fuel gases to the case of free flames.[15] Since the free flame case is considered the ideal flame environment in this study this serves as a good comparison for the current flames that utilize a duct and a co-flow. For the ethylene fuel used in the current study the air to fuel ratio, $y = 14.3$, so that the parameter P' in this case is $P' = P(1 + y)^{1/3} = 2.48P$.

For values of the injection parameter less than approximately $P = 8$ (corresponding to $P' = P(1 + y)^{1/3}$ » 20) the normalized flame length data generally appear to be reasonably consistent with the linear scaling of the free flame values versus the parameter P'. An exception seems to be the point $P = 4$ ($P' = 10$), but in this case ms a consistent mean flame length was difficult to obtain given the very short pulse duration ($t_i = 5.745$ ms) compared with the framing rate of the camera (33.33 ms / frame). It was thus difficult to determine the exact moment of extinction of the flame in this case. Therefore the actual mean flame length of these flames are likely larger than those shown in Fig. 4.5 for the $P = 4$ case.

The normalized flame length appears to approach the steady-state value for large values of $P' \geq 28$ ($P \geq 11$). The knee in the flame length data in the figure corresponds roughly to the transition point between puff-like and elongated flame structures as discussed earlier in the P parameter discussion in Section 2.1. This data suggests that, for a sufficiently large injected volume, the flame length of fully-modulated flames reaches a value that is independent of the injection volumes and comparable to average normalized steady-state flame length of L / d_{jet} » 240. The trends for normalized flame lengths of the current results, for both the free flame with a smaller d_{jet} and V_o than previous experiments and the ducted flame case with and without co-flow, are in reasonable agreement with previous results[15] for free flames.

4.2.2 Co-flow Effects On Flame Length

In general flame length increased with increasing co-flow for a given injection volume. The amount of the increase depended on the amount of co-flow supplied and on the volume of fuel injected. This section quantitatively discusses these phenomena and also presents a scaling argument to characterize the effects of co-flow on flame length.

For the puff-like flames where P £ 8 the mean normalized flame length increases as the strength of the co-flow increases, as can be seen in Figs. 4.5, 4.6, and 4.7. The normalized mean flame length vs. U_{cof} / U_{jet} for different values of P are shown in Figs. 4.6 and 4.7 for a $Re_{jet} = 3{,}000$ and for $Re_{jet} = 5{,}000$, respectively. The data sets are for ducted flames except for the free flame points shown for reference. The mean flame length of the ducted flames without co-flow slightly exceeds those of the corresponding free flames. Thus it appears that, for the injection conditions of this study, there is no co-flow strength which gives the same mean flame length for a ducted flame as observed for the free flame case.

On a fractional basis, the greatest increase in flame length for increasing co-flow strength is for $P = 6$ where $Re_{jet} = 3{,}000$, in this case the mean normalized flame length increases by 30% as the co-flow strength increases from $0 \leq U_{cof} / U_{jet} \leq 0.044$. The amount of flame length increase is comparable for the $P = 8$, $Re_{jet} = 5{,}000$ case, amounting to approximately 27%. For values of P in excess of $P = 8$, the sensitivity of the flame length, on a fractional basis, decreases substantially. For $P = 11$ (P' » 28) the mean flame length increases no more than 13% for $U_{cof} / U_{jet} = 0.026$ compared to the no co-flow case. The impact of co-flow for $P = 15$ is much less, amounting to no more than 1% for $Re_{jet} = 5{,}000$, which is within the uncertainty of the measurement of ± 5%. Thus as the P value increases, and more elongated flames result, the sensitivity of flame length to co-flow decreases significantly, leading to essentially no impact on flame length for $P > 11$. The mean steady-state flame length for $Re_{jet} = 3{,}000$ and 5,000 was seen to vary by less than 4% (again, within the measurement uncertainty) for the maximum co-flow strengths of $U_{cof} / U_{jet} = 0.026$ and 0.044 as compared with the free flame case and the no co-flow case. Fluctuations seen for the flames where $P \geq 11$ can be attributed to fluctuations in the flame tip which are characteristic of steady flames.

The sensitivity to co-flow of fully-modulated flames with values of the pulsing parameter P£ 8 is apparent in these figures. The mean flame length evidently increases with the addition of even the smallest amount of co-flow employed here, $U_{cof} / U_{jet} = 0.001$. It should be noted that there is necessarily a fundamental change in the flow field in rising from no co-flow to even a very weak co-flow. In the case were there is no co-flow supplied ventilation air flow is primarily in the opposite direction to the fuel flow, except in the vicinity of the jet nozzle exit, where the air flows radially inwards towards the combustor centerline. In the case with co-flow, by contrast, the air flow throughout the combustor, including the region near the fuel nozzle exit, is in the same axial direction as the fuel flow. The significance of changes in mean flame length for compact flame puffs in switching between no co-flow and co-flow regimes is unclear at present since the smallest value of co-flow studied was $U_{cof} / U_{jet} = 0.001$, but there seems to be minimal deformation of the flame structure up to values of $U_{cof} / U_{jet} \approx 0.01$. It can also be noted that there appears to be no values of U_{cof} / U_{jet} at which the free-flame flame lengths are equal to the flames with confinement and co-flow.

4.2.3 Scaling Argument for Co-flow Effects

To assess the effects of co-flow on the flame length of widely-separated puffs, an argument based on the relative strength of the co-flow and the puff core velocity may be invoked. It is hypothesized that the degree to which the co-flow velocity affects the mean flame length depends on the strength of the co-flow relative to an appropriate characteristic velocity for the burning fuel puff. A given change in the mean flame length is expected for $U_{cof} = U_{cl} / k$, where U_{cl} is the centerline velocity of the gas in the puff and $k>1$ is a constant to be determined from experimental data. To continue this argument, scaling laws based on the puff centerline velocity, U_{cl}, are required. Previous experiments[14,15] have shown that the scaling for celerity of puff diffusion flames is approximately the same as isothermal buoyant puffs in the Boussinesq limit where the celerity can be expressed as, $S_T = 2.8F_B^{1/2}z^{-1}$. Data from Hermanson *et. al.*[15] suggest that for flames the celerity is more accurately expressed as $S_F = 6.17 F_B^{1/2} z^{-1}$. The centerline gas velocity is roughly twice the celerity,[27,29, 28] so:

$$U_{cl} \approx 2(6.17\, F_B^{1/2}\, z^{-1}), \tag{4.1}$$

where z is the vertical distance from the source and F_B is the total buoyancy of the puff given by,

$$F_B = g\,\frac{r_a - r_{puff}}{r_a}\,V \tag{4.2}$$

where r_{puff} and V are respectively the average puff density and volume, and r_a is the ambient density. In the Boussinesq limit, F_B is conserved whereas in puff-like diffusion flames, F_B is expected to vary due to the heat release and the accompanying density changes.

The density ratio in the expression for F_B can be found from the temperatures in the puff and the co-flow air assuming uniform pressure. Moreover, the puff volume increases as its radius cubed, V » $3r^3$, with the proportionality constant of 3 taken from previous isothermal experiments.[30] Strictly speaking, the co-flow velocity would enter the scaling of puff width with downstream distance. Since the evaluation of co-flow effects considered here only considers the mean flame length, the discussion is not critically dependent on the precise determination of the flame structure. However, in this case, the scaling argument regarding co-flow effects is no longer relevant. On dimensional grounds, the puff radius r must scale with the distance z from the source in the far field of turbulent puffs. Previous research has shown that, up to the point of puff burn-out, the puff size increases with distance.[14] The flame puff radius can be expressed as r » $0.155z$.[29] Thus, F_B can be estimated for puff-like diffusion flames based on these scaling relationships to obtain

$$F_B \approx g\left(1 - \frac{T_a}{T_{puff}}\right)(0.0112 \;\; z^3). \qquad \textbf{(4.3)}$$

Subsequently, the puff centerline velocity can be found and is

$$U_{cl} \approx 1.31\left[g\left(1 - \frac{T_a}{T_{puff}}\right) z\right]^{1/2} = 1.31 \;\; [g'(z) \;\; z]^{1/2}, \qquad \textbf{(4.4)}$$

where $g' = g(1 - T_a/T_{puff})$ and T_{puff} and T_a is the mean temperature near the flame tip and the temperature of the co-flow, respectively. By requiring that the co-flow velocity be a fraction of the puff centerline velocity at the flame tip, $z = L$, the co-flow velocity for a given increase in mean flame length can be determined and is described by $U_{cof} = U_{cl}(z=L)/k \approx 1.31 \; [g'(z=L)L]^{1/2}/k$, where k is a constant evaluated from experimental results. Finally, the above expression can be non-dimensionalized by the velocity at the source, U_{jet}, to give

$$\left.\frac{U_{cof}}{U_{jet}}\right)_{char} = \frac{4.11}{k}\left[g'(z = L) \; \frac{L}{U_{jet}^2}\right]^{1/2}. \qquad \textbf{(45)}$$

Thus, the characteristic value of U_{cof} / U_{jet} depends on the flame length, average temperature at the flame tip, and the jet source velocity. The quantity in the brackets is essentially a Richardson number based on the flame length and the jet injection velocity. Temperature measurements in previous experiments[15] with isolated puff diffusion flames have indicated that the mean puff temperatures near the flame tip are generally around 400 C, regardless of the puff injection conditions. The flame tip temperature is based on previously reported measurements in fully-modulated, puff-like flames.[15] That temperature is an average in the puff region, where there has been substantial entrainment of excess air, and is not representative of a flame sheet or stoichiometric surface. Lastly, the flame length of widely-separated puffs is expected to scale linearly with P, so that $L/d_{jet} = a(1+y)^{1/3}P$, where a is a constant. This scaling assumes that the flame length asymptotes to zero in the limit of $P = 0$ (zero injected fuel volume). The current results for $6\ £\ P\ £\ 11$ suggest the value $a = 9.84$ for a co-flow strength of $U_{cof}\,/\,U_{jet} = 0.01$. Substituting for L/d then allows the direct determination of the expected characteristic co-flow velocity as a function of injection conditions for a given fuel:

$$\left.\frac{U_{cof}}{U_{jet}}\right)_{char} = \frac{4.11}{k}\left[\frac{g d_{jet}}{U_{jet}^{2}}\left(1 - \frac{T_a}{T_{puff}(L)}\right)\left(1 + y\right)^{1/3} P\right]^{1/2} . \tag{4.6}$$

The utility of the preceding argument in determining a threshold for the onset of co-flow effects in fully-modulated, turbulent, diffusion flames can be determined from a systematic examination of the flame length results for the full range of co-flow strengths employed in this investigation.

The observed threshold data based on the mean flame lengths shown in Fig. 4.6 and 4.7 are compared in Fig. 4.8 with the predicted values of the characteristic co-flow strength. The data points shown correspond to an increase in the mean flame length of 15%, with the upper and lower error bars corresponding to flame length changes of 18% and 12%, respectively. The curves, for several values of Reynolds number, were generated for ethylene fuel using the scaling arguments developed above by Eq. (5.6). The experimentally determined values of the characteristic co-flow velocity are seen to be in reasonable agreement with those suggested by the scaling argument for a value of k

= 8.54. The value of this constant would naturally be different for a different fractional change in mean flame length than the 15% considered here. It should be emphasized that the proposed scaling argument is only expected to be valid for compact, puff-like structures, which require a value of P £ 8 for ethylene fuel. A threshold value of co-flow strength for the more elongated structures corresponding to higher values of P is not yet established (the co-flow also appears to have a less marked impact on flame length in these cases).

The threshold value of the normalized co-flow strength, U_{cof} / U_{jet} , does have a Reynolds number dependence, as shown in the preceding scaling argument, with in fact a lower co-flow strength being required for the onset of co-flow effects as the Reynolds number increases.

With this argument it is possible to estimate at what co-flow value a particular flame puff will require to exhibit an increase in mean flame length of 15% from the corresponding no co-flow case. All the flames studied in this section are non-interacting, which means that each flame completely burns up before the next flame is injected. These flames have very low duty-cycles that do not exceed $a_{inj} = 0.05$. As the duty-cycle is increased significant modifications to both the flame length and structure can occur. The effects of the duty-cycle are presented in the following section.

5. Interacting Flame Puff Results

Interacting fully-modulated flames are flames that have not had enough time to completely burn out before the next flame is injected. Interacting flames can appear in one of two ways. The first way and the most common is where two flames interact with each other as shown in Fig. 5.1, in this case the individual structures cannot be distinguished from each other. The second type is where the individual structures can be distinguished and these are shown in Fig. 5.2. Increasing the duty-cycle α_{inj}, which is accomplished by decreasing the off time of each cycle for a given injection time, controls this interaction. As noted previously $\alpha_{inj} = ft_i$ and was varied from $\alpha_{inj} = 0$ to $\alpha_{inj} = 0.5$ in the current discussion. This change in duty-cycle can cause a noticeable change in the combustion process as seen in the changes in flame structure and flame length.

5.1 Flame Structure

Increasing the duty-cycle can cause the flame structure to change significantly such that all puff characteristics can be lost, as seen in Fig. 5.1. The greatest structural change seen for flame with $P \leq 8$ is with an increase of duty-cycle to $\alpha_{inj} = 0.5$. As seen before the $P = 11$ ($t_i = 119$ ms) and $P = 15$ ($t_i = 303$ ms) cases are not effected noticeably by this change. In the $P = 4$ case as the duty-cycle is increased the blue puff like structures seen in the non-interacting flames are lost. This effect can be seen in Fig. 5.1 for $\alpha_{inj} = 0.3$. In this case the flame structure quickly turns from the blue compact puff structure to a flame that resembled an undersized steady flame. The same is seen with $P = 6$ and 8, where the vortex and tail structure seen in these flames for the non-interacting cases quickly resembles a more steady-like flame structure. The changeover occurs later for the $P = 6$ and 8 case than for the $P = 4$ case, but by $\alpha_{inj} = 0.5$ the distinct head and tail regions are gone and a more steady flame appearance prevails. This drastic change in structure directly relates to a change in flame length, which is qualitatively described in the next section.

5.2 Effect Of Duty-Cycle On Flame Lengths

As with the non-interacting case a Panasonic Color CCD camera was used to capture images for the interacting flame case. In order to obtain average values for flame lengths, ensemble averages of between 50 – 75 frames were used. The measured average flame length is normalized by the nozzle diameter for all cases shown in this section.

5.2.1 Flame Length Scaling Comparison With Previous Results

Figure 5.3 shows the mean flame lengths for a fully-modulated flames with a small co-flow ratio of $U_{cof} / U_{jet} = 0.005$ at a duty-cycle of $a_{inj} = 0.1$ and free flames by Hermanson *et al.*[15] On this plot the *x*-axis is the *P'* parameter that is described in Section 5.2.1 and the *y*-axis is the normalized flame length.

For values of the injection parameter less than approximately $P = 8$ (corresponding to $P' = P(1 + y)^{1/3}$ » 20) the normalized flame length data for flames with $a_{inj} = 0.1$ appear to be reasonably consistent with the linear scaling versus the parameter $P(1 + y)^{1/3}$. The normalized flame length appears to approach the steady-state value for $P(1 + y)^{1/3}$ » 28, which for the ethylene fuel employed here corresponds to a value of $P = 11$. The trends in normalized flame length of the current results of $a_{inj} = 0.1$ are in reasonable agreement with previous results by Hermanson *et al.*[15]

5.2.2 Flame Length Characterization

Representative normalized mean flame length results are presented in Fig. 5.4 for several values of duty-cycle. In almost all cases considered here, increasing the value of the duty-cycle, for a fixed value of injected volume (or P) leads to a longer flame length, as shown in the figure. These structures exhibit mixing and combustion characteristics more similar to those of steady-state flames. As the P number increases into the regime where the transition to elongated flame structures is complete ($P \sim 13$), the flame length is generally less impacted by duty-cycle, and ceases to exhibit the clear dependence on duty-cycle shown in Fig. 5.4.

The amount of increase in mean normalized flame length with duty-cycle is most apparent for values of $P < 8$, with the maximum change seen for $P=4$ or $P'=10$. In this case the flame length increase is about 212% as the duty-cycle is changed from 0.1 to 0.5. As P increases, the dependence of flame length on duty-cycle appears to weaken substantially. This suggests a substantially lower impact of neighboring structures on the entrainment and mixing for cigar-shaped flames than for their puff-like counterparts.[15] The longer shape of the elongated flames implies that the bulk of the entrainment comes from the flanks of the flame structures, where little interaction effects with neighboring structures are possible. By contrast, the much more compact puffs (which occur for lower values of P) entrain a larger fraction of their air appetite from the trailing ends of the structures, where interaction between neighboring puffs could be expected to be more substantial. In any case, the linear scaling of mean flame length with P number, derived for widely-spaced puffs represents a lower limit on the mean flame length. As the duty-cycle increases, the interaction between puffs becomes strong and the assumptions of widely-spaced puff-like pulsed jets used in fitting the linear scaling law are no longer satisfied.

The extent of interaction between neighboring structures for puff-like flames can be characterized in terms of a dimensionless parameter $P = V_0^{2/3}(1-\alpha_{inj})/A_d\alpha_{inj}$, where A_d is the cross sectional area at the fuel nozzle exit. This parameter was developed by Johari & Motevalli[14] by relating the convection time scale of the injected fuel puffs in the near-nozzle region to the interval between the pulses. It should be noted that this parameter was only intended to characterize whether structures can be considered interacting or not, not to predict either the resulting value of the flame length or the rate of the fuel/air mixing.

The parameter P can be used to characterize the transition from isolated puff behavior to 'interacting' puff behavior where low values of this parameter represent interacting flames.[14] This parameter appears to have some utility in collapsing the flame length data presented in Fig. 5.4 above, as shown in Fig. 5.5. Here the flame length of each case is normalized by the corresponding injection volume to the 1/3 power and also by the corresponding flame length and injection volume of a reference puff for the same injection time and at the lowest value of duty-cycle. This normalization removes from consideration variations in flame length arising solely from variations in injected volume. This normalization also forces all of the data to the value of unity for the shortest duty-cycle. A substantial increase (up to 212%) in the normalized flame length begins to become apparent with a decrease in the parameter P amounting to roughly two orders of magnitude. The data shown are all for puff-like structures in this case except the last case ($P = 11$, $t_i = 119\ ms$) which can be considered to be transitional. The corresponding change in normalized flame length for elongated structures is noticeably less, amounting to roughly 13% for a decrease in P of two orders of magnitude. This is consistent with the decreasing sensitivity of elongated flame structures to the interaction between adjacent structures as the duty-cycle increases.

These results suggest that increasing the amount of co-flow would not be expected to bring dramatic changes in the mean flame length of elongated flames whose lengths are not greatly impacted by the duty-cycle. For the shorter flames however, increasing the amount of either the co-flow or the duty-cycle increases the flame length significantly. Thus it may be expected that the combined effects of high duty-cycle and a large value of co-flow would result in a larger increase in flame length for the shorter flames ($P = 4$ and $P = 6$) would be relatively larger than would occur due to changes in duty-cycle or co-flow individually.

It should be noted that there is similar uncertainty in flame lengths of the interacting flames as was presented in Section 5.2.3 for the non-interacting flames. However the framing rate plays less of a role in this case, since for $a_{inj} \geq 0.1$ every flame tends to be highly sooting, even for the $P = 4$ case. There is however a strong fluctuation in the burn-out length of these flames due to the cyclic nature of the flames that compounds the error in these measurements not thought to be more than ±5%.

6. Emission and Temperature Results

Better understanding of the combustion process in fully-modulated flames may be obtained by examining their emission characteristics. The following discussion characterizes UHC, NO_x, NO, CO, CO_2, and O_2 concentrations and how they vary with injection parameters including injection time (t_i), injection duty-cycle (α_{inj}), co-flow velocity ratio (U_{cof} / U_{jet}) and the pulse parameter (P).

One major problem with fully understanding the emissions of fully-modulated flows with a co-flow is the large dilution they experience due to air entrainment into the flame. One way to compensate for the entrainment dilution effects on an average basis is to convert the relative emissions to 15% oxygen concentrations. This is an industry standard and is used to compare different types of combustors that have different amounts of dilution air. In addition to entrainment differences, duty-cycle effects complicate this problem even further. Fully-modulated flames characteristically have a flame-on period and a flame-off period that contribute and reduce the emission concentrations measured. In the interest of understanding the air entrainment and fuel / air mixing associated with these fully-modulated flames it is desirable to remove the duty-cycle effect in an attempt to expose mixing characteristics of individual pulses. This cannot be accomplished by analyzing the raw emissions data since the gas analyzers respond too slow (typically 30 – 40 seconds) to accurately capture the concentrations of the flame-on periods. Instead a time averaged concentration is measured and then scaled by duty-cycle in order to evaluate concentrations of individual pulses.

6.1 O_2 and CO_2 Concentrations

The oxygen and carbon dioxide concentrations in the exhaust gases are indicative of the total amount of fuel consumed. In stoichiometric combustion, O_2 concentrations are zero and CO_2 concentrations are relatively high (2 moles of CO_2 in a stiochiometric burn) indicating the complete burning of fuel. In the cases studied here there is significant dilution due to entrainment of excess air, which makes individual pulse behavior difficult to expose. This dilution makes O_2 and CO_2 concentrations difficult to examine on a purely quantitative level so these concentrations are discussed on a more qualitative level.

6.1.1 O_2 Concentrations

Shown in Fig. 6.1 is the O_2 concentration vs. the injection duty-cycle for a series of different injection parameters. For P = 3, 3.5, and 4 average oxygen values initially decrease with duty-cycle when $a_{inj} \leq 0.2$ to between 17.25% and 18.25%. The concentrations then rise to become comparable to the concentrations present in the rest of the test cases, $P \geq 5$ and the steady case, the steady flame ($a_{inj} = 1$) is shown at $a_{inj} = 0.6$ for reference. This trend suggests that the oxygen consumption for these cases, $P \leq 4$, are the highest. Due to excess dilution experienced by the flames, the average O_2 concentrations never decrease below 17.25% for any condition. For P = 5 to 15 there is a constant increase in oxygen consumption from the low duty-cycle case to the fuller or higher duty-cycle cases. This is due to the fact that increasing the duty-cycle for a constant P number there is inherently an increase in overall flame-on time, which necessarily increases the average O_2 consumption. Fig. 6.2 shows average oxygen percent as a function of the pulse parameter, P. This plot suggests similar trends as Fig.

6.1 in that there is more oxygen consumption in the low P number, low duty-cycle flames than in the larger ones. There also appears to be a transition region from relatively high consumption to low consumption for P = 4.5 - 6. This is reasonable since average values are measured and when a_{inj} is increased the flame takes up a higher percentage of the total cycle time. The steady flame (shown here at P = 16 for reference) consumption of oxygen is comparable to the percentages measured for the low P number regime.

6.1.2 CO_2 Concentrations

Average concentrations of CO_2 were measured and are presented in Figs. 6.3 and 6.4. These two figures show $[CO_2]$ plotted against a_{inj} and P, respectively. Carbon dioxide production seems greatest for $P \leq 4$ with the steady flame value comparable to these values. As seen in Fig. 6.4 the carbon dioxide concentrations appear to become nearly constant for a given a_{inj} when $P \geq 6$. A similar trend with oxygen consumption was seen in the previous section. It is important to note that all these are average values of emissions and are masked by entrainment dilution and duty-cycle effects and are not emissions corresponding to individual pulses.

One way to remove entrainment dilution and duty-cycle effects is to plot the normalized O_2 concentrations, $[\Delta O_2] / [CO_2]$, defined here as $[\Delta O_2] = [O_{2\text{Ambient}}] - [O_{2\text{measured}}]$. This is similar and proportional to the more commonly used emission index which is expressed in grams of emissions / kg of fuel. This ratio removes entrainment dilution and duty-cycle effects since both O_2 and CO_2 experience the same entrainment dilution and duty-cycle. This approach is also used with the remaining emission species measured, i.e. $[UHC] / [CO_2]$ etc. To make certain that corrections for the conversion of dry to wet molar fractions also do not affect these results, the dry concentrations are used for this data set. Fig. 6.5 shows $[\Delta O_2] / [CO_2]$ as a function of a_{inj}. As seen in the other figures, flames with P = 3, 3.5, and 4 are indeed the highest consumers of O_2 since the $[\Delta O_2] / [CO_2]$ value is small for these cases. The trends for all other cases also are similar in this plot validating the trend seen in the other figures.

In order to help understand the entrainment and combustion characteristics of these flames, pollutant formation such as UHC, CO, NO, and NO_x must be examined. These are discussed in the following sections.

6.2 UHC and CO Emissions

The concentrations of unburned hydrocarbons (UHC) and carbon monoxide (CO) are presented in this section. By studying the concentrations of these two species, which usually tend to have similar trends for lean flames, it is possible to determine how completely flames are burning. In stoichiometric combustion both species are converted into CO_2 and H_2O leaving a very low concentration levels of UHC and CO. If the concentrations of UHC and CO are high, then two possibilities are that the combustion process is being quenched (cooled off) or the mixture is fuel-rich.

As mentioned previously there is a large amount of dilution in the flames studied due to entrainment effects complicated by duty-cycle effects that create a time-varying concentration. Entrainment dilution can be removed on an average basis by converting measurements to a 15% O_2 concentration. The next way to examine these species is to analyze the flames as individual puffs, essentially giving an instantaneous view of a puff. To acquire this instantaneous view, it is necessary to scale the emissions by some duty-cycle that is effectively experienced at the probe location. Average emissions and the effective instantaneous measurement of individual pulses are described in the following sections.

6.2.1 UHC Emissions

The average UHC concentrations are shown in Fig. 6.6. These results suggest that for $a_{inj} \geq 0.3$ there is little or no dependency of the concentration of UHC on the P number for all test cases. It also shows that for $P \geq 6$ there is only a small variation in UHC concentration for all values of a_{inj} and the variation is comparable to the steady state case concentration of 3.5 ppm. For $P \leq 5$ totally different trends are exhibited. Each of these cases display a definite rise and fall of the UHC concentration for $a_{inj} \leq 0.2$. The rise in the data set here may be attributed to the increasing of the injection duty-cycle of incompletely burning non-interacting puffs, since a greater volume of fuel is being injected over a given time. The peaks range from 66 times greater than steady state for $P = 3$ to 11.5 times greater for $P = 5$. These peaks may correspond to the points at which the flames start to interact. When this interaction effect becomes significant the flames are injected close enough together so the excess UHC are consumed and amount of UHC left over falls off significantly. By $a_{inj} = 0.3$ the peak values have decreased to a value comparable to those of steady state flames.

Fig. 6.7 shows the UHC concentrations at 15% O_2 as a function of the injection duty-cycle. The measurements show similar trends to those of Fig. 6.6, except that the magnitudes are larger and the peaks for $P \leq 4$ collapse onto each other at about 94 times the steady state value. Also a peak for $P = 5$ is present here at a value of 31 times the value of the steady state case. There also appears to be a slight decrease in the average UHC concentration as a_{inj} is increased for $P = 6$ and 8, which was not seen in the uncorrected average emissions. The following table summarizes the peaks and the location of the peaks with respect to the injection duty-cycle:

Table 6.1: UHC concentrations

Average UHC Concentrations			**Average UHC Concentrations at 15% O_2**		
P	*Peak Value (ppm)*	*Location of Peak (a_{inj})*	*P*	*Peak Value (ppm)*	*Location of Peak (a_{inj})*
3	225	0.043	3	569	0.025
3.5	170	0.050	3.5	586	0.025
4	158	0.075	4	569	0.050
5	40	0.125	5	165	0.100

Figures 6.6 and 6.7 both suggest that flames with $3 \leq P \leq 5$ when $a_{inj} \leq 0.2$ do not burn completely, but begin to burn better as a_{inj} increases. These figures suggest that flames burn more complete and independent of the duty-cycle for cases where $P \geq 6$.

6.2.2 CO Emissions

Average CO concentrations follow similar trends as the UHC measurements discussed above. Figure 6.8 shows average CO concentrations vs. the injection duty-cycle. All values shown in this figure are averages, so entrainment dilution and duty-cycle effects are fully relevant. For values for $a_{inj} \geq 0.2$, all average CO emission measurements were essentially constant and below the steady state flame value of 45.5 ppm. For $P \geq 5$ the average CO concentrations were reasonably constant for all values of a_{inj}. For $P \leq 4$ when $a_{inj} \leq 0.2$, there is a significant rise and fall in the CO concentrations as seen in the figure. The rise could be from increasing the duty-cycle of incompletely burning flames, resulting in a trend similar to the trends seen in the UHC measurements discussed previously. Then, as the puffs begin to interact, the concentration of CO falls. The peak concentrations of CO range from 7 times greater than steady state value for P = 3 to 4.25 times the steady state value for P = 4.

Figure 6.9 shows average CO concentrations corrected to 15% O_2 concentrations vs. injected duty-cycle. Carbon monoxide concentrations for $a_{inj} \geq 0.2$ are relatively constant and comparable or lower than the steady state value of 75.5 ppm. As seen before for $P \geq 6$ values are reasonably constant for the entire range of a_{inj} except for a small peak seen for P = 5. A rise and fall is still present for $P \leq 4$ cases with the peaks concentrated between $0 \leq a_{inj} \leq 0.1$ ranging from 7.5 times to 2 times the steady state value. Table 6.2 summarizes the peaks and the location in terms of the injection duty-cycle for average concentrations of CO:

Table 6.2: CO concentrations

Average CO Concentrations			**Average CO Concentrations at 15% O_2**		
P	*Peak Value (ppm)*	*Location of Peak (a_{inj})*	P	*Peak Value (ppm)*	*Location of Peak (a_{inj})*
3	271	0.050	3	607	0.038
3.5	195	0.075	3.5	530	0.050
4	170	0.100	4	586	0.050
5	36	0.150	5	196	0.100

Both the CO and UHC concentrations presented here are wet average values corrected to 15% O_2 concentrations. In order to understand the emissions of a single puff and try to interpret some of the flow dynamics driving these flows it is desirable to attempt to find a correction factor that will allow for the estimation of the emissions associated with each individual puff.

6.2.3 Effective (actual) Duty-cycle

Average emission concentrations need to be scaled by a new duty-cycle to remove duty-cycle effects and obtain an estimation of the emission concentrations of individual puffs. The injected duty-cycle, a_{inj}, cannot be used for this purpose since it represents the duty-cycle at the nozzle exit and does not necessarily reflect the duty-cycle at points downstream in the flow, particularly at the flame tip. Figure 6.10 is a graphic explanation of the reason why a_{inj} is different from the duty-cycle in the vicinity of the probe. In the figure (figure not to scale), the thin dotted line represents the injection cycle, a_{inj}, and the heavy line represents the actual duty-cycle in the vicinity of the emissions probe. The reason that $Dt_2 > Dt_1$ is because after the puff is injected the velocity decreases along with an increase in the puff diameter as it travels downstream. This accounts for a fuller (larger "on time" percentage) duty-cycle in the vicinity of the probe. The shift in the start of the pulse is attributed to the time it takes for the leading edge of the puff to reach the probe location. The horizontal dashed line on this plot represents the time-averaged values that are measured. This value is reasonably constant because any highs and lows in the measured concentrations from the fully-modulated flow are damped due to the slow response time of the gas analyzers. By scaling the time-averaged concentrations by the new duty-cycle, now referred to as a_{act}, the peaks of the pulses on Fig. 6.10 emerge and are more representative of the concentration values for individual puffs. The point at which a_{act} becomes unity corresponds to the point when flames in the vicinity of the probe are totally interacting (no spaces between pulses). It is important to remember that there may still be an off-time (period of no injected fuel) at the nozzle exit but in the vicinity of the probe the flame appears to be steady. The next step is to determine this new duty-cycle. The next sections describe three possible ways of physically describing a_{act}.

6.2.3.1 Actual Duty-Cycle Based on Frame Counting

The first method attempted used frame counting and is referred to as the $a_{Frame\ Method}$. Recorded image sequences for P = 4, 6, 8 were examined and frames that had any flame visible in them were counted for each case. The number of frames counted was multiplied by the framing interval of 33.33 ms. This gave an estimate of the flame on-time for each case (represented as t_{FM}). The times determined from this procedure were 93.3 ms for P = 4, 166.7 ms for P = 6, and 193.3 ms for P = 8. The duty-cycle $a_{Frame\ Method}$ is determined by dividing t_{FM} by t_T, where t_T is the standard total time calculated dependent upon the corresponding a_{inj}:

$$a_{FrameMethod} = \frac{t_{FM}}{t_T}. \tag{6.1}$$

It is valid to use t_T as the total cycle time since the total time of a cycle is always the same at any point in the flow. Since there is a time delay from the initial injection of a flame until the probe begins seeing any of the injected products, as shown in Fig. 6.10, this method estimates an upper limit for a_{act}.

6.2.3.2 Actual Duty-Cycle Based on Measured Celerity

This method is referred to as $a_{Measured\ Speed}$ and is based on the celerity of the flame determined from measuring the forward progress of a flame front between two successive captured images. This was done for values of P = 4, 6, and 8. The velocities were as follows: 372.5 mm/s for P = 4, 665.8 mm/s for P = 6, and 1056.8 mm/s for P = 8. These velocities were measured as close as possible to the burn out point of the flame to give the closest estimate of the velocity of the flame puff at the probe. To find an $a_{Measured\ Speed}$

a flame on time, t_{MS}, needs to be determined. This is found by considering the flame to be a spherical structure with a diameter *d* as it passes the probe. The puff diameter *d* was determined to be 0.31*L* from work done by Johari *et al.*[29] These variables can be combined together to form an expression for t_{MS}:

$$t_{MS} = \frac{d}{u} = \frac{0.31L}{u} = 0.31\left(\frac{L}{d_{jet}}\right)\left(\frac{d_{jet}}{u}\right), \tag{6.2}$$

where *u* is the measured velocity as described above. With an effective on-time, τ_{MS}, determined it is now possible to express the $a_{Measured\,Speed}$ as:

$$a_{MeasuredSpeed} = \frac{t_{MS}}{t_T}. \tag{6.3}$$

Here t_T is the total cycle time, which is calculated from the injection parameters and is independent of the distance away from the source when puffs are not interacting.

6.2.3.3 Calculated Celerity Based Duty-Cycle

This method of determining an effective duty-cycle is a more analytical one than the two previous methods and is expressed by $a_{Calculated\ Speed}$. Although, like the measured speed method explained above, this method also considers the fluid in the vicinity of the probe to be a buoyant spherical thermal. The time that it takes this thermal to pass the probe is the effective on time or in this case t_{CS} and is expressed below,

$$t_{CS} = \frac{d}{S_F}, \tag{6.4}$$

where *s* is the celerity or the speed of the spherical structure and *d* is the diameter of the sphere and equal to 0.31*L*.[29] Celerity expressed here as S_F is defined as:

$$S_F = 2.8b\frac{\sqrt{F_B}}{L} = 6.17\frac{\sqrt{F_B}}{L} = 0.11\sqrt{gd_{jet}\left(1-\frac{T_a}{T_{puff}}\right)\left(\frac{L}{d_{jet}}\right)^{\frac{1}{2}}}, \tag{6.5}$$

where b is a constant that is equal to 2 and is found from previous results of Hermanson *et al.*[15]. The total buoyancy, F_B, is formed by assuming the spherical thermal is isothermal, buoyant and in the Boussinesq limit. The duty-cycle can be expressed as,

$$a_{CalculatedSpeed} = \frac{t_{CS}}{1/\,f}, \quad where \quad f = \frac{a_{inj}}{t_i} \quad and \quad t_i = \frac{P^3 d_{jet}}{U_{inj}}, \qquad \textbf{(6.6)}$$

where P is the pulse parameter for the particular flow, a_{inj} in the corresponding injection duty-cycle, U_{inj} is the injected velocity, and t_{inj} is the injection time. Combining the expressions and the known constants such as d_{jet}=0.002 m, T_a = 23 C, T_{puff} = 400 °C[15], and U_{inj} = 22.6 m/s gives an expression for the duty-cycle:

$$a_{CalculatedSpeed} = 102.9\frac{\left(L/d_{jet}\right)}{P^3}a_{inj}. \qquad \textbf{(6.7)}$$

In this method it is necessary to know the flame length of each flame in order to obtain an accurate estimation of the actual duty-cycle.

6.2.3.4 Discussion of Actual Duty-Cycle Estimation Methods

The three duty-cycle corrections discussed above are compared in Fig. 6.11 as a function of the injection duty-cycle. In the figure $a_{Frame\ Method}$ is represented on the plot by the curves named frame method plots, $a_{Measured\ Speed}$ is represented by the curves named Measured S and the $a_{Calculated\ Speed}$ is represented by the curve Predicted S. As seen in the figure the frame based duty-cycles are indeed an upper limit as none of the other estimated a_{act} exceeds this estimation. The two other methods as seen in the plot are relatively close to one another, which suggests that either one of these methods gives a reasonable estimate of the duty-cycle in the vicinity of the probe. For the purpose of this study the duty-cycle values found from calculating the speed (analytical approach) are used in the final corrections of the emissions to account for duty-cycle effects. The main reason for this choice is because the method can be easily extended to case in which flame lengths were not found experimentally. Flame lengths in these cases are easily interpolated to give reasonable flame lengths to use in this correction. It is important to remember that this is only an estimate of the true duty-cycle experienced close to the probe and gives reasonable values and definite trends of individualized pulses.

This method suggests that for a $P = 4$ flame when the injection duty-cycle reaches a value of about $\alpha_{inj} = 0.075$, the flames are considered interacting in the point of view of the probe. This means that for any $P = 4$ flame at $Re_{jet} = 5{,}000$ with values of $\alpha_{inj} \geq 0.075$, the flames are essentially interacting and have a $\alpha_{act} = 1$. This level of interaction for $P = 6$ is close to $\alpha_{inj} = 0.2$ and is close to $\alpha_{inj} = 0.35$ for $P = 8$. This new α_{act} approach can now be used to scale average CO and UHC values in order to estimate the emissions of individual pulses. Figure E-1 in Appendix E shows α_{inj} compared to α_{act} in tabular form.

6.2.4 UHC and CO with Corrected Duty-cycle

The duty-cycle corrections discussed above allows the estimation of the emission content of individual puffs where the flames are non-interacting in the vicinity of the probe. When using this correction there is only a change in the non-interacting flames. In cases where the flame is interacting near the probe, $\alpha_{act} \approx 1$, no correction is made. The corrections for UHC and CO for $\alpha_{act} \leq 1$ and $\alpha_{inj} \leq 0.5$ are discussed next.

Figures 6.12 and 6.13 shows [UHC] / α_{act} and [CO] / α_{act} as a function of α_{inj}. As discussed in the previous section only low values of α_{inj} (where $\alpha_{act} \leq 1$) actually are corrected by the new duty-cycle in this case. These two plots can be compared to Figs.

6.6 and 6.8 in order to realize what flames are affected by this correction. Dividing by a_{act} is logical in this case since actual emission concentrations should be higher than the measured values because of the period that the flame is off and ambient air is being sampled. These plots illustrate the entire range of non-interacting or individual pulses and interacting pulses. If these plots are compared to Figs. 6.6 and 6.8 no changes are visible in the data for $a_{act} = 1$, but changes are noticeable for values where $a_{act} < 1$. It is important to notice here that the overall trends are preserved in that flames with $P \leq 4$ with $a_{inj} \leq 0.1$ burn less efficiently than flames with $P \geq 5$ throughout the range of a_{inj}.

Figures 6.14 and 6.15 show [UHC] / a_{act} and [CO] / a_{act} as a function of a_{act}. This way of presenting the data emphasizes the non-interacting or individual puffs. The same trends as seen before for UHC and CO concentrations are apparent for these non-interacting puffs, in that for $P \leq 4$ the UHC and CO concentrations are much larger than the rest of the flames studied.

6.2.5 Normalized CO and UHC Concentrations

One last way to compare this data is by expressing the concentrations in the form of an emission index. The emission index is normally expressed as gm(emission) / kg (fuel). In this case we are assuming that all fuel goes to CO_2, which is a relevant assumption since CO and UHC concentrations are in the ppm range. With this assumption it is possible to express an equivalent emission index as [UHC] / [CO_2] and [CO] / [CO_2]. In this case the dry concentrations of CO and CO_2 are used and the wet concentrations of UHC and CO_2 are used, respectively, to form these normalizations. These ratios are fully independent of entrainment dilution and duty-cycle effects since both species are affected the same. Fig. 6.16 and 6.17 show normalized concentrations of

UHC and CO, respectively for the entire range of a_{inj}. The trends in these plots are consistent with trends that flames with $P \leq 4$ are not burning completely. The normalizations are also plotted in Figs. 6.18 and 6.19 against $a_{act} \leq 1$, which emphasizes the trends for individual pulses. These trends also agree with the previous trends found for UHC and CO emissions.

UHC and CO concentrations have been examined in several different ways and each time the similar overall trends have emerged. These data sets suggest flames that with $P \leq 4$ and $a_{inj} \leq 0.1$ have higher UHC and CO concentrations signifying that they are not completely burning the injected fuel. One possible reason for the high concentrations of UHC and CO in these cases is that the flame is entraining so rapidly that the flame is being quenched out, not allowing all of the fuel to be burned. There also appears to be a transition in the range of $4 \leq P \leq 6$ where the combustion process seems to become independent of the duty-cycle and emissions become reasonably constant throughout the entire range of a_{inj}.

6.3 Air / Fuel Ratio

The air/fuel ratio relates the amount of oxidizer at a point in the flame to the amount of fuel assuming that no combustion has taken place. The stoichiometric air/fuel ratio of ethylene is 14.2, which means 14.2 times as much air than fuel is required for complete combustion. The lean flammability limit of ethylene is 34.6, which means that if there is more than 34.6 times the amount of air than fuel then the mixture is too dilute and combustion initiation cannot occur. The air/fuel ratio (F) in this study was determined by simplifying chemical terms and the combustion oxidation chemical reaction to form,

$$F = 2.53\left(\frac{1 - \mathrm{X}_{O_2D} - \mathrm{X}_{CO_2D}}{\mathrm{X}_{CO_2D}}\right), \qquad \textbf{(6.8)}$$

where X_{O_2D} is the measured dry molar fraction of oxygen and X_{CO_2D} is the measured dry molar fraction of carbon dioxide.

Figure 6.20 shows the average air/fuel ratio as a function of P and Fig. 6.21 portrays the average air/fuel ratio as a function of a_{inj}. Fig. 6.20 suggests that for $P \geq 5$ air/fuel ratio decreased as the duty-cycle increases. This might be expected because as the duty-cycle increases the puffs are spaced closer together, which gives a smaller percentage of time when no flame is present. For $P \leq 4$ this trend seems to reverse itself for reasons unclear at present. Figure 6.21 shows similar trends and for all values of P examined the air/fuel ratio decreases as the duty-cycle increases. The figure also exhibits that there is a sudden increase in F for values of $a_{inj} \leq 0.1$ when $P \leq 5$. This trend becomes reasonably constant after $a_{inj} \leq 0.1$ for these same P values. For all other P numbers studied there is a monotonic decrease in the air/fuel ratio as the duty-cycle increase to $a_{inj} = 0.5$. These results are all based on average measurements and entrainment dilution as well as duty-cycle effects are present. Although, with the use of the actual duty-cycle discussed previously, it is possible to reveal the trends of individual pulses.

When the air/fuel ratio is multiplied by a_{act} and is plotted against a_{inj}, as in Fig. 6.22, the entire range of corrected non-interacting pulses and interacting pulses is apparent. This figure can be compared with Fig. 6.21 to realize what flames are affected by this correction. In Fig. 6.23, $F{*}a_{act}$ is plotted as a function of a_{act}, which highlights the non-interacting flames. The data seem to suggest here that all pulsing flames with P

≤ 8 have higher air/fuel ratios than the steady state or $P = 11$ and $P = 15$. This suggests that fully-modulated flame puffs with low volumes have entrainment values 2 – 4 times higher than the steady state case. This seems to be consistent with the trends seen earlier for UHC and CO concentrations for puffs when $P \leq 4$. In these trends UHC and CO concentrations were larger for these flames. This supports the theory that these low volume flames where $P \leq 4$ and $a_{inj} \leq 0.1$ are being quenched by high entrainment and are not completely burning.

6.4 Temperature Measurements

Time averaged temperatures were measured 1 cm upstream of the emissions probe and are presented in Figure 6.24. The average temperatures are highest for $P \leq 4$. In these three cases the temperature rises to a maximum and then decreases to a value comparable to the rest of the flames where $P \geq 5$. For the high P number cases ($P \geq 5$) cases the temperature is lower but steadily rises to a maximum as the duty-cycle increases and reaches a maximum at $a_{inj} = 0.5$. This plot also exhibits similar trends to Fig. 6.3 where CO_2 is plotted against the injection duty-cycle. This is to be expected since CO_2 is indicative of the amount of heat released in the combustion process.

Fig. 6.25 shows temperature / a_{act} as a function of the injection duty-cycle. This plot displays the entire range of both corrected individual pulses as well as interacting pulses where $a_{act} = 1$. It seems that flames with $P \leq 4$ the temperatures are comparable to the flames with longer injection periods, where $P = 11$ and 15. The temperatures for flames with $P = 5$, 6, and 8 seem to be correspondingly lower. For flame where $P \leq 4$ temperatures seem to start lower and rise to a maximum beyond $a_{inj} = 0.1$.

Figure 6.26 is a plot of the temperature as a function of a_{act}, showing the temperature values for single non-interacting flames only. The same trend is present here as seen in Fig. 6.25, for puffs with $P \leq 4$. The temperatures are also comparable to flames with $P = 11$ and 15. When $P = 5$, 6, and 8 the temperatures are also correspondingly lower.

Since the temperatures are higher in the P = 3, 3.5, 4, 11, and 15 cases it might be expected that the NO and NO_x values will also be higher in these cases as well. This is discussed in the next section.

6.5 NO_x and NO Emissions

NO and NO_x emissions are highly controlled in industrial combustors including boilers, vehicles engines and jet aircraft engines. Low NO and NO_x emissions are desirable since they are harmful to the atmosphere. As with UHC and CO emissions NO and NO_x emissions need to be understood in these flames before these systems can be utilized in an industrial application.

Figures 6.27 and 6.28 show NO and NO_x average concentration values converted to 15% O_2 concentrations (refer to Appendix E for average concentration plots). In both cases it appears that flames with $P \leq 4$ produce considerably more NO and NO_x on an average basis than the other conditions. For low injection duty-cycles, the NO concentrations for these flames average 20 ppm and rise to an average peak of 85 ppm for $a_{inj} > 0.1$. The NO_x concentrations rise similarly but rise from an average of 17 ppm to an average of 110 ppm for $a_{inj} > 0.1$. When $P \geq 5$, NO production has an average of 10 ppm, then rises with increasing a_{inj} to an average concentration of about 35 ppm at $a_{inj} =$ 0.5. NO_x concentrations in this range have an average of 30 ppm and rise to an average of 44 ppm when a_{inj} = 0.5. All concentrations are below the steady state values of 114 ppm for NO and 117 ppm for NO_x measured. Both of these figures show trends similar to that of the temperature shown in Fig. 6.24, which is consistent with the expectation that the higher temperature flames would produce more NO and NO_x.

Figures 6.29 and 6.30 show [NO] / a_{act} and [NO_x] / a_{act} as a function of a_{act}. As explained previously, by plotting against a_{act}, individual pulse concentrations and trends become apparent. It appears that flames with injection parameters of P = 11 and 15 produce the highest NO and NO_x concentration output for these non-interacting cases. Where the NO and NO_x production for all other P cases are similar with lower NO and NO_x production.

In order to explain trends seen in these NO and NO_x measurements it is necessary to consider the NO and NO_x concentrations normalized to CO_2. Figures 6.31 and 6.32 show [NO] / [CO_2] and [NO_x] / [CO_2] plotted as a function of a_{inj}. These plots show the entire range of interacting and non-interacting individual pulses. The trends here follow the trend seen in the average figures for NO and NO_x concentrations. From this data it is difficult to differentiate the flame puffs that are individual (non-interacting) and interacting in the vicinity of the probe. Figs. 6.33 and 6.34 show the same combustion normalizations but plotted against a_{act}. There are no clear trends apparent in this plot, except perhaps that flames with P = 11 and 15 produce larger amounts of NO and NO_x when the flames are non-interacting. A maximum for flames with $P \leq 4$ is not apparent in these figures as was seen in Figs. 6.27 and 6.28 previously. This suggests that the maxima are not present while the puffs are non-interacting and might be present when the puffs become interacting. The next two figures shown are Figs. 6.35 and 6.36, which show the [NO] / [CO_2] and [NO_x] / [CO_2] plotted as a function of a_{inj}, but only where a_{act} = 1, hence these graphs represent interacting flames only. In examining these plots it is apparent that a maximum in the data occurs for $P \leq 4$ at around 0.3% [CO_2] at about $0.1 \leq a_{inj} \leq 0.2$. The data approach a constant value as $a_{inj} = 0.5$. This suggests that flames with $P \leq 4$ produce high NO and NO_x values when they are interacting, unlike the high CO and UHC concentration apparent for non-interacting flame puffs. All other values of P seem to climb slightly with increasing duty-cycle and reach a maximum of 0.14% CO_2 at $a_{inj} = 0.5$. If Fig. 6.31 is compared with Fig. 6.16 it appears that the NO_x and NO concentrations reach a maximum at about the same a_{inj} at which the UHC and CO concentrations decrease rapidly. These trends follow both air/fuel and temperature trends since as the flames entrain more air the temperatures are lower and CO and UHC are higher indicating incomplete combustion. As flame become interacting the air/fuel ration increases, temperature increases, NO and NO_x increase and UHC and CO decrease. This change in characteristics suggests a significant change in the entrainment and pulse structure as the transition occurs.

7. Conclusions

A pulsed fuel injector system was used to study the flame structure, flame length, and emissions of fully-modulated jet diffusion flames over a range of injection times with a variable air co-flow. In all cases the jet was completely shut off between pulses (fully-modulated) for varying intervals, sometimes to ensure widely-spaced, non-interacting puffs, others to ensure interacting puffs. The fuel consisted of ethylene at one atmospheric pressure and the oxidizer was standard shop air. Imaging of the luminosity from the flame revealed distinct types of flame structure, depending on the length of the injection interval. For short injection times (small injected volume) and short duty-cycle, puff-like flame structures were observed. The burnout length of the puffs was at least 83% less than the steady-state flame length. For relatively longer injection times, a more elongated shaped flame resulted. The flame lengths of the elongated flames were generally comparable to those of the corresponding steady-state cases. For compact puffs, the addition of co-flow for ducted flames generally resulted in an increase in the mean flame length, amounting to an increase in flame length of up to 30% for a co-flow strength of $U_{cof} / U_{jet} = 0.045$. The effect of co-flow on the normalized flame length of pulsed flames with longer injection times, as well as steady flames, was much less significant. The mean flame length for flames in the ducted combustor generally exceeded that of the corresponding free flames, even for the case where no co-flow air was supplied. A characteristic value for the co-flow strength at which a specified change in flame length occurs is developed, and is seen to be in good agreement with the experimental results.

Interacting flames studied showed dramatic increase in flame lengths with increasing duty-cycles. The flame lengths became less effected by increases in duty-cycle as the P number increased. A maximum change of 220% in flame length was seen in flames with $P = 4$ as the duty-cycle increased to $a_{inj} = 0.5$. The minimum change in flame length was around 5% for flames with $P = 15$.

Average emission measurements were completed for a wide range of interacting and non-interacting puffs with a low co-flow. In order to remove duty-cycle effects and estimate emission concentrations for non-interacting or individual puffs, scaling arguments were formed to estimate the actual duty-cycle experienced in the vicinity of the probe. These data suggest that there is a change in flow dynamics for puffs going from $P \leq 4$ to puffs where $P \geq 5$ and a transition region is present between $4 \leq P \leq 6$. The puffs with low P (3, 3.5, and 4) exhibited high O_2 consumption and high CO_2 production, but also showed high CO and UHC production in comparison with the other cases. Air/fuel ratios were higher in puffs where $P \leq 8$ as compared the steady state case and flames with $P = 11$ and 15. With this information it is hypothesized that flames where $P \leq 4$, which also have a very small fuel volume, are being partially quenched out rapid entrainment. For NO and NO_x emissions it seems that when $P \leq 4$, NO and NO_x emissions are also higher than the rest of the cases studied. The difference is that these flames seem to produce high NO and NO_x after the flames become interacting whereas the high CO and UHC concentrations are mainly for non-interacting flames. These trends also correlate well with temperature trends found for the entire range of flames studied. The non-interacting partially quenched flames have lower temperatures consistent with incomplete burning and excess CO and UHC, but lower NO and NO_x As a_{inj} increases and the flames begin to interact and there is a change in the air entrainment of the flames, as air is then mainly pulled in through the outside boundary of the flame (similar to a steady flame) rather than up from the bottom of the flame as seen in puffs with $P \leq 4$ and $a_{inj} \leq 0.1$. The relatively less entrainment gives rise to an increase in temperature and an increase in the NO and NO_x production as well as the more complete burning of CO and UHC. Flames where $P \geq 6$ seem to have reasonably constant CO and UHC concentrations and slightly rising NO and NO_x concentrations as the duty-cycle increases to $a_{inj} = 0.5$.

7.1 Future Work

Several recommendations for future work can be made and are discussed next. First, future studies in flame length and structure with co-flow may explore the initial jump in flame length from cases with no co-flow to a small co-flow value of $U_{cof} / U_{jet} = 0.001$. Also imaging capabilities using a faster camera (60 frames per second or more) would make imaging flames with $P \leq 4$ easier give a more accurate mean flame length.

Emission measurements of flames with different Reynolds numbers would be insightful in understanding how the flame behavior changes with varying injection velocities. Also, testing emissions for flames with varying amounts of co-flow may assist in learning how the entrainment characteristics of the flames change with different amounts of co-flow. On the hardware side, the mechanism that is used to move the probe along the axis of the flame could be improved to make probe placement repeatability more accurate. This mechanism could also incorporate a traverse mechanism so emission profiles perpendicular to the flame axis can be made.

Finally, the present experiments are to be continued in a microgravity environment. Tests are currently being conducted in the 2.2 Second Drop Tower at NASA Glenn Research Center in Cleveland, Ohio. Microgravity experiments remove the effects of buoyancy that are present in all normal –gravity experiments and will help reveal the fundamental fluid dynamics of these flames. Many specifications for the combustion rig used in the drop tower tests were determined from the current hardware designs and experimental results. The comparison of normal-gravity results to results from the microgravity tests is very crucial in the effort to completely understand the fluid mechanics of these fully-modulated flames.

References

[1]Tang, Y.M., Ku, S.H., Daniel, B.R., Jagoda, J.I., and Zinn, B.T., "Controlling the rich limit of operation of pulse combustors," *23rd Symposium (International) on Combustion*, 1995, pp. 1005-1010.

[2]Keller, J.O. and Hongo, I., "Pulse combustion: The mechanisms of NO_x production," *Combustion and Flame* 80, 1990, pp. 219-237.

[3]Keller, J.O., Westbrook, C.K., "Response of pulse combustor to changes in fuel composition," *21st Symposium (International) on Combustion*, 1986, pp. 547-555.

[4]Tang, Y.M., Waldherr, G., Jagoda, J.I., and Zinn, B.T., "Heat Release Timing in a Nonpremixed Helmholtz Pulse Combustor," *Combustion and Flame* 100, 1995, pp. 251-261.

[5]Crow, S.C. and Champagne, F.H., "Orderly structure in jet turbulence," *J. Fluid Mech.* 48, 1971, pp. 547-591.

[6]Long, D. F., Kim, H., and Arndt, R.E.A., "Controlled suppression or amplification of turbulent jet noise," *AIAA Journal* 23, 1985, pp. 828-833.

[7]Bremhorst, K. and Hollis, P.G., "Velocity field of an axisymmetric pulsed, subsonic air *AIAA Journal* 28, 1990, pp. 2043-2049.

[8]Vermeulen, P.J., Ramesh, V., and Yu, W.K., "Measurement of entrainment by acoustically pulsed axisymmetric air jets," *Journal of Engineering Gas Turbines and Power* 108, 1986, pp. 479-484.

[9]Lovett, J.A. and Turns, S.R., "Experiments on axisymmetrically pulsed turbulent jet *AIAA Journal* 28, 1990, pp. 38-46.

[10]Reuter, D.M., Hedge, U.G., and Zinn, B.T., "Flowfield measurements in an unstable *Journal of Propulsion and Power* 6, 1990, pp. 680-865.

[11]Reuter, D.M., Daniel, B.R., Jagoda, J.I., and Zinn., B.T., "Periodic mixing and combustion processes in gas fired pulsating combustors," *Combustion and Flame* 65, 1986, pp. 281-290.

[12]Chen, T.Y., Hegde, U.G., Daniel, B.R., and Zinn, B.T., "Flame radiation and acoustic intensity measurements in acoustically excited diffusion flames," *Journal of Propulsion and Power* 9, 1993, pp. 210-216.

[13]Hegde, U.G., Reuter, D.M., and Zinn, B.T., "Sound generation by ducted flames," *AIAA Journal* 26, 1988, pp. 532-537.

[14] Johari, H. and Motevalli, V., “Flame length measurements of burning fuel puffs,” *Comb. Sci. Tech.* 94, 1993, pp. 229-245.

[15] Hermanson, J.C., Dugnani, R., and Johari, H., “Structure and flame length of fully-modulated diffusion flames,” *Combustion Science and Technology*, 155, 2000, 203-225.

[16] Jones, H.R.N. and Leng, J., “The effect of hydrogen and propane addition on the operation of a natural gas-fired pulsed combustor,” *Combustion and Flame* 99, 1994, pp. 404-412.

[17] Montgomery, C.J., Kaplan, C.R. and Oran, E.S., “Effect of coflow velocity on a lifted methane-air jet diffusion flame,” *Twenty-Seventh Symposium (International) on Combustion*, The Combustion Institute, Pittsburgh, PA, 1998, pp. 1175-1182.

[18] Thring, M.W. and Newby, M.P., “Combustion length of enclosed turbulent jet flames,” *Fourth Symposium (International) on Combustion*, The Combustion Institute, Pittsburgh, PA, 1953, pp. 789-796.

[19] Dahm, W.J.A. and Dibble, R.W., “Coflowing turbulent jet diffusion flame blowout,” *Twenty-Second Symposium (International) on Combustion*, The Combustion Institute, Pittsburgh, PA, 1988, pp. 801-808.

[20] Biringen, S., “An Experimental Study of a Turbulent Axisymmetric Jet Issuing into a Co-flowing Air Stream,” *VKI Tech. Note 110*, 1975.

[21] Turns, Stephen R. and Bandaru, Ramarao V., “Carbon Monoxide Emissions from Trubulent Nonpremixed Jet Flames,” Combustion and Flame 94, 1993, pp. 462-468.

[22] Turns, Stephen R., “Understanding NO_x Formation in Nonpremixed Flames: Experiments and Modeling,” *Progress in Energy and Combustion Science* 21, 1995, pp. 361-385.

[23] Haynes, B.S. and Wagner, H.G., “Soot formation,” *Progress in Energy and Combustion Science* 7, 1981, pp. 229-273.

[24] Mungal, M. G., Karasso, P. S., and Lozano, A., “The visible structure of turbulent jet diffusion flames: Large-scale organization and flame tip oscillation,” *Combustion Science and Technology* 76, 1991, pp. 165-185.

[25] Turns, Stephen R., An Introduction to Combustion, Concepts and Applications McGraw-Hill, Inc., 1996.

[26] Becker, H.A. and Yamazaki, S., “Entrainment, momentum flux and temperature in vertical free turbulent diffusion flames,” *Combustion and Flame* 33, 1978, pp. 123-149.

[27] Turner, J.S., “Buoyant plumes and thermals,” *Annual Rev. Fluid Mech.*, 1, 1969, pp. 29-44.

[28] Turner, J.S. *Buoyancy Effects in Fluids*, Cambridge University Press, 1973.

[29] H. Johari, K.J. Desabrais, J.C. Hermanson, “Experiments on Impulsively Started Jet Diffusion Flames,” AIAA 35, 1997, pp. 1012-1018.

[30] Scorer, R.S., “Experiments on convection of isolated masses of buoyant fluid,” *J. Fluid Mech.* 2, 1962, pp. 583-594.

[31] Keller, J.O. and Hongo, I., “Pulse Combustion: The Mechanisms of NO_x Production,” *Combustion and Flame* 80, 1990, pp. 219-237.

Figures

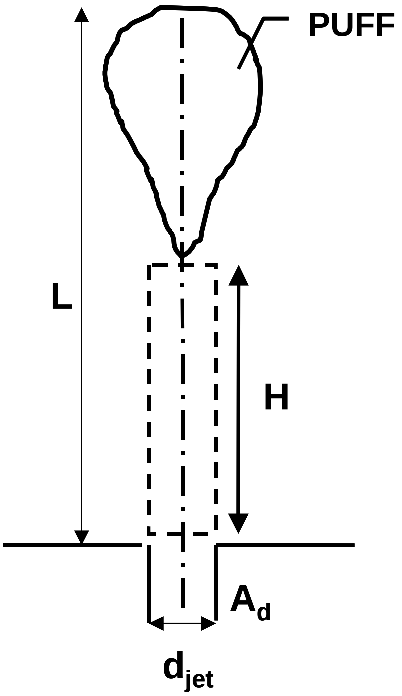

- **The “P number” is used to characterize puffs and is defined as**

$$P = (H/d_{jet})^{1/3} = 1.08\, V_0^{1/3}/d_{jet}$$

- **Scaling arguments for non-interacting puffs show**

$$L/d_{jet}\ \alpha\ (1+\Psi)^{1/3} P$$

Ψ = stoichiometric air to fuel ratio

- **Duty cycle effects on puff interactions can be characterized by the parameter Π**

$$\Pi = V_0^{2/3} (1 - \alpha_{inj}) / A_d\, \alpha_{inj}$$

Figure 2.1: Injection parameter *P* and visual description

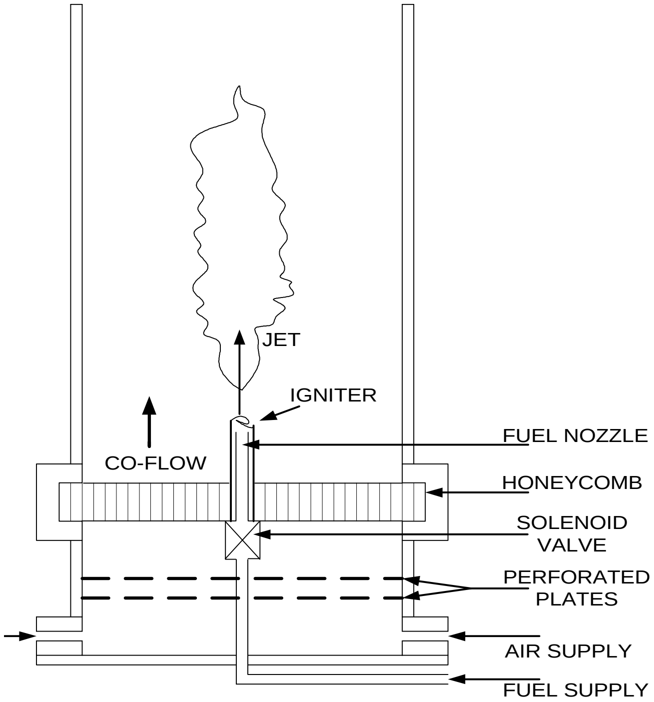

Figure 2.2: Combustor schematic

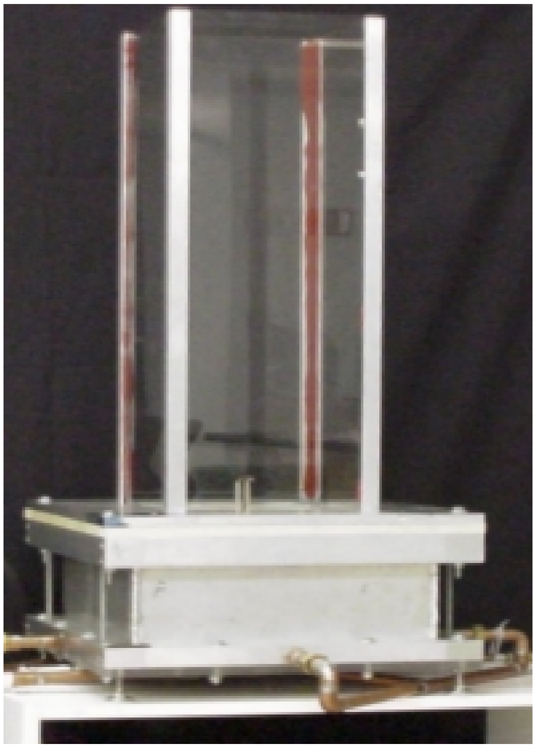

Figure 2.3: Combustor photograph

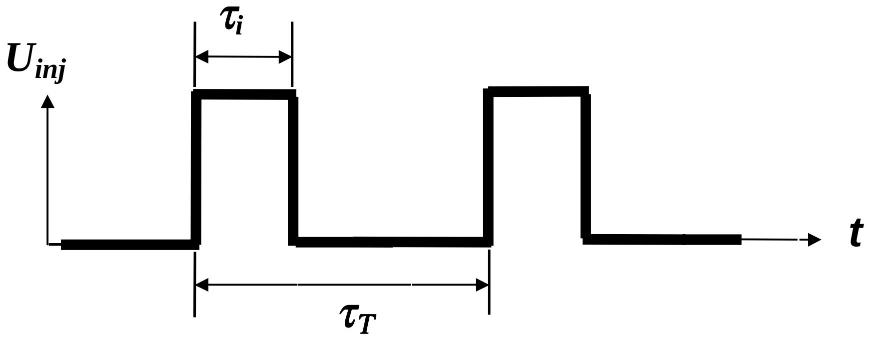

Figure 2.4: Ideal pulse cycle

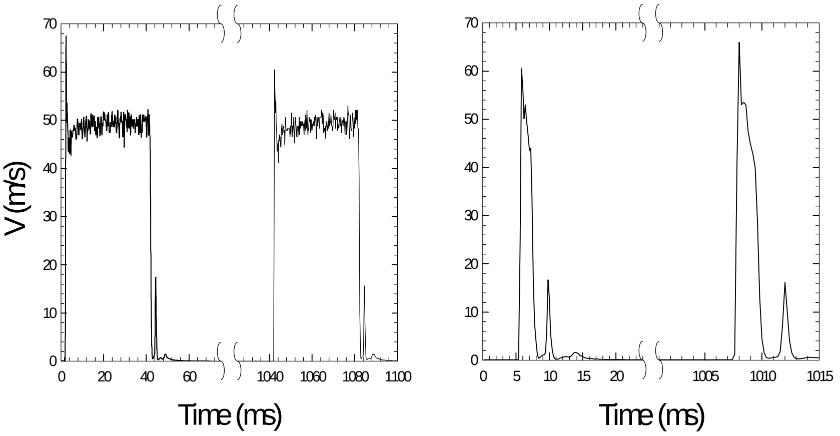

Figure 2.5: Actual pulse cycle

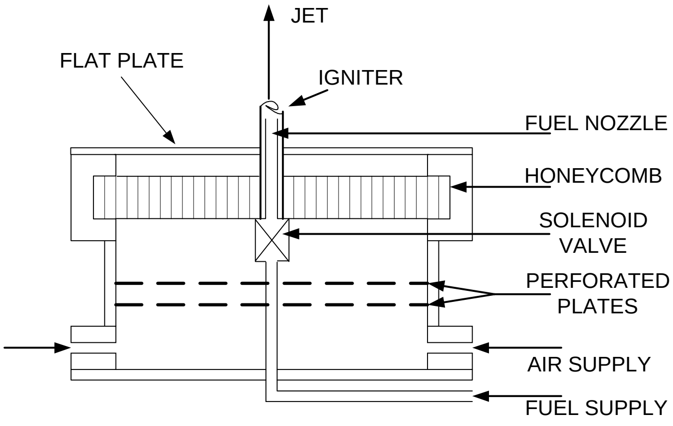

Figure 2.6: Combustor schematic for free flames

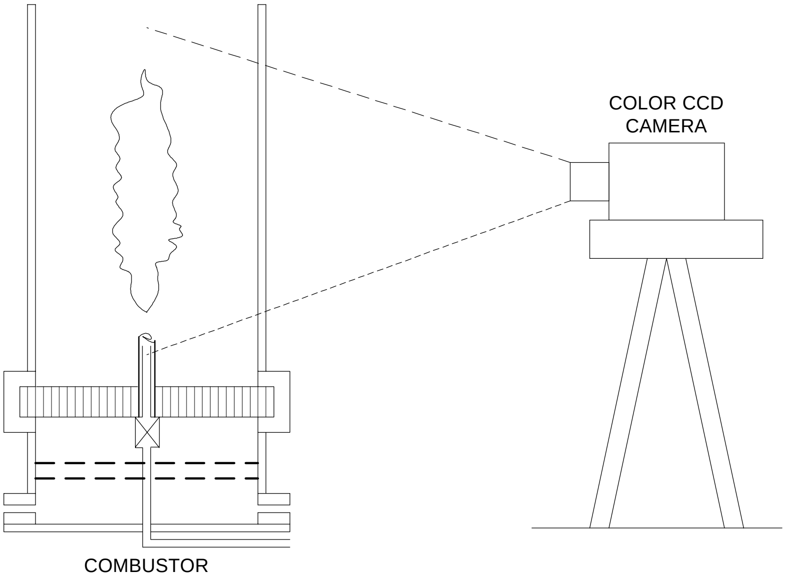

Figure 2.7: Flame length imaging setup

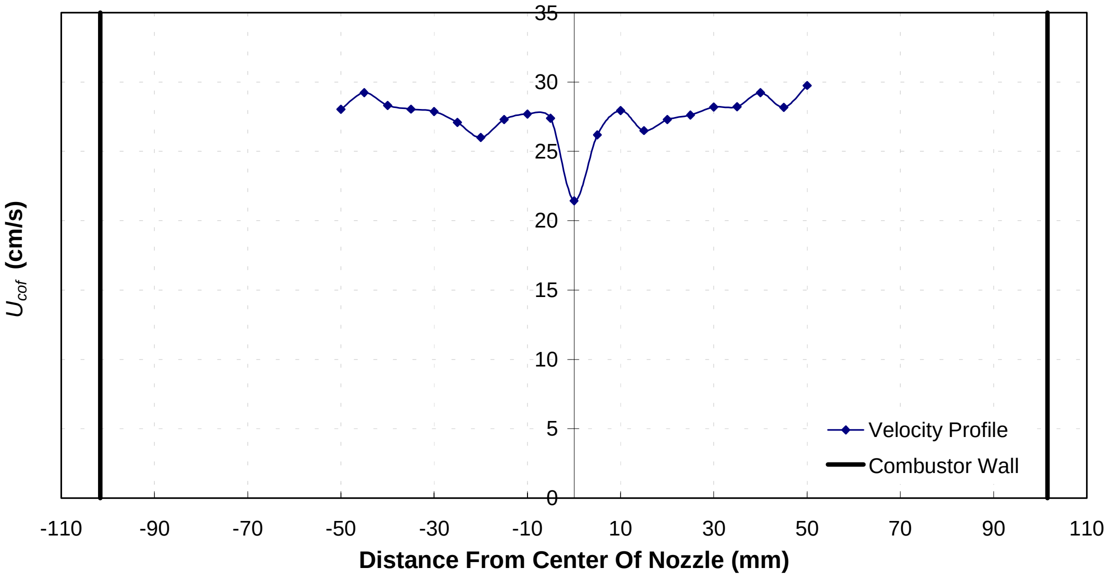

Figure 3.1: LDV co-flow velocity profiles, x_{jet} = 20 mm,

Average U_{cof} = 27.5 cm/s

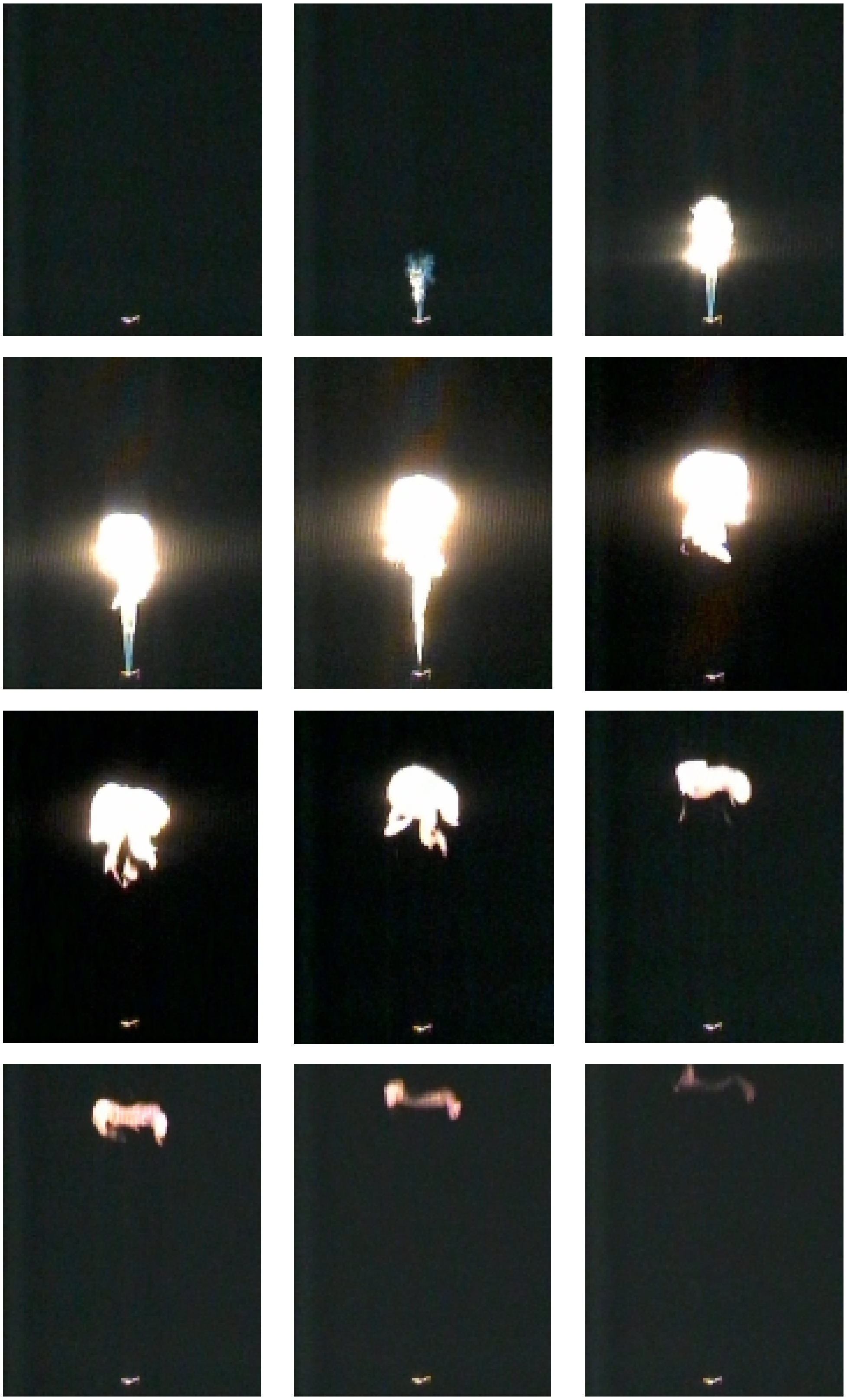

**Figure 4.1: *P*=8 pulsed flame image sequence,
Image Height = 38 cm**

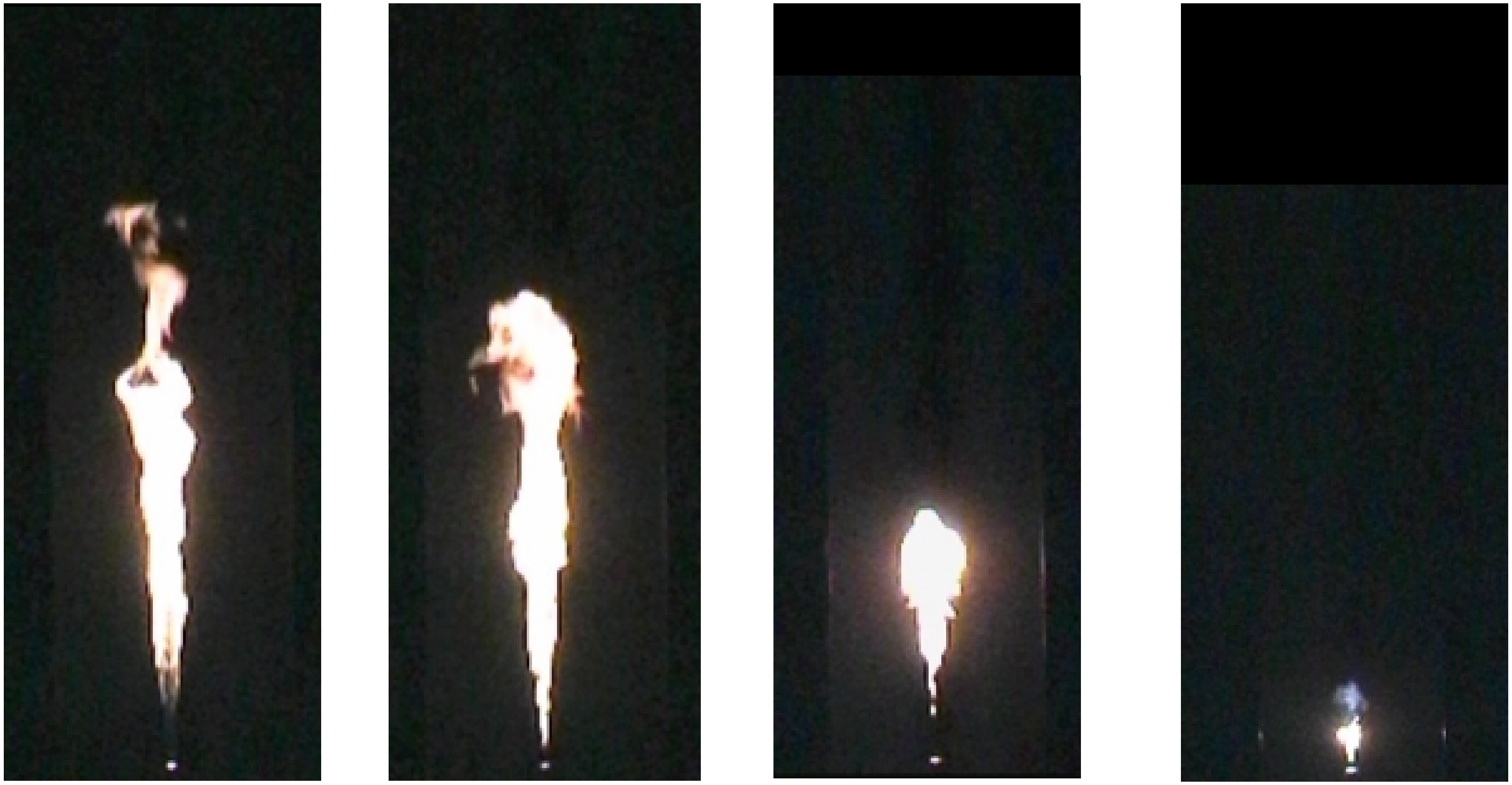

a) Steady Flame, $\tau_i = \infty$ **b) $P = 11, \tau_i = 119$ ms** **c) $P = 8$, $\tau_i = 46$ ms** **b) $P = 4$, $\tau_i = 5.745$ ms**

Figure 4.2: Flame comparison, $Re_{jet} = 5,000$, $U_{cof} / U_{jet} = 0.005$, Image Height = 58.4 cm

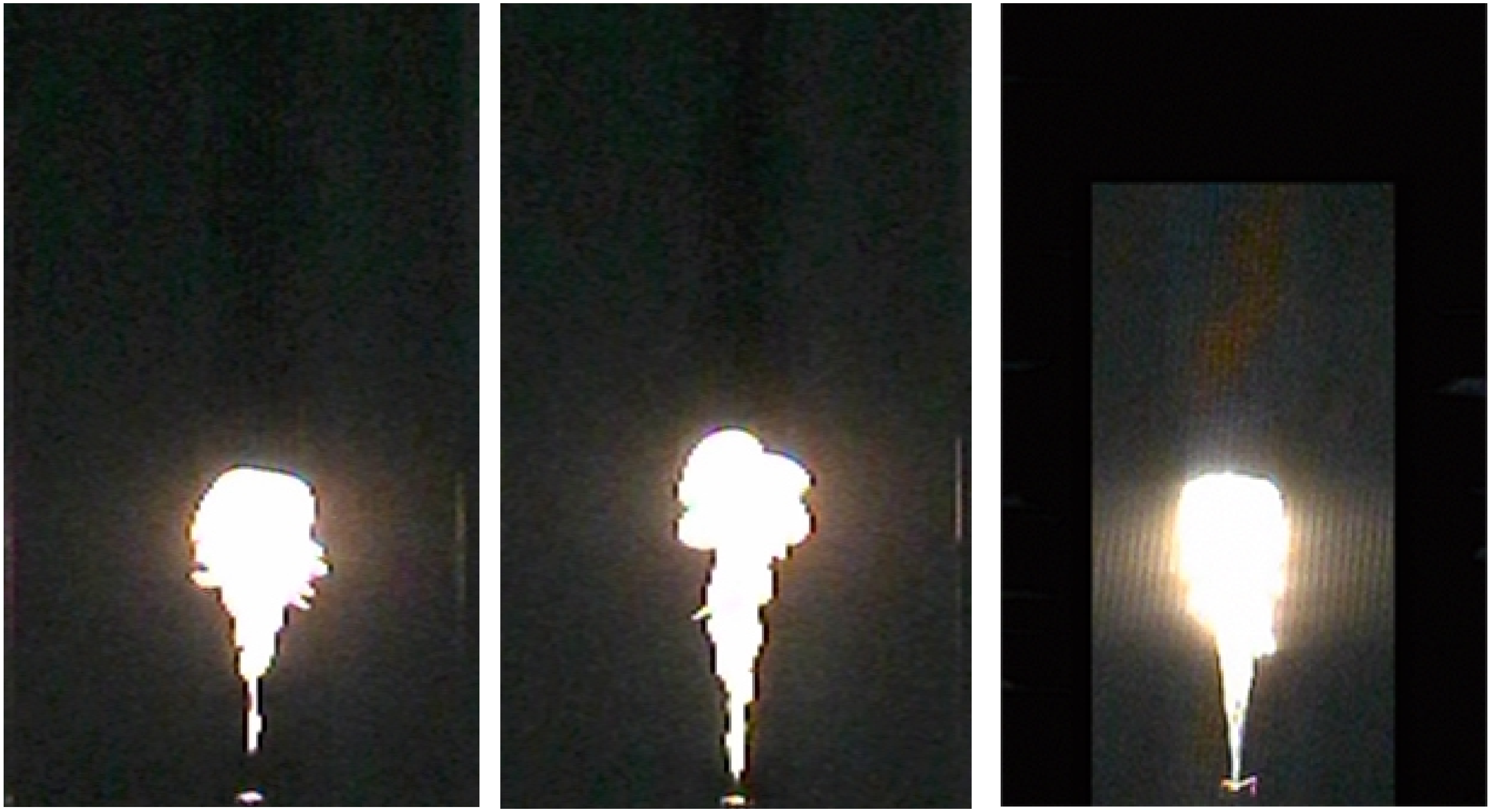

a) $U_{cof} / U_{jet} = 0$ b) $U_{cof} / U_{jet} = 0.005$ c) Free Flame

Figure 4.3: $P = 8$ flame puff comparison, $\tau_i = 46$ ms, $Re_{jet} = 5{,}000$, Image Height = 45.7 cm

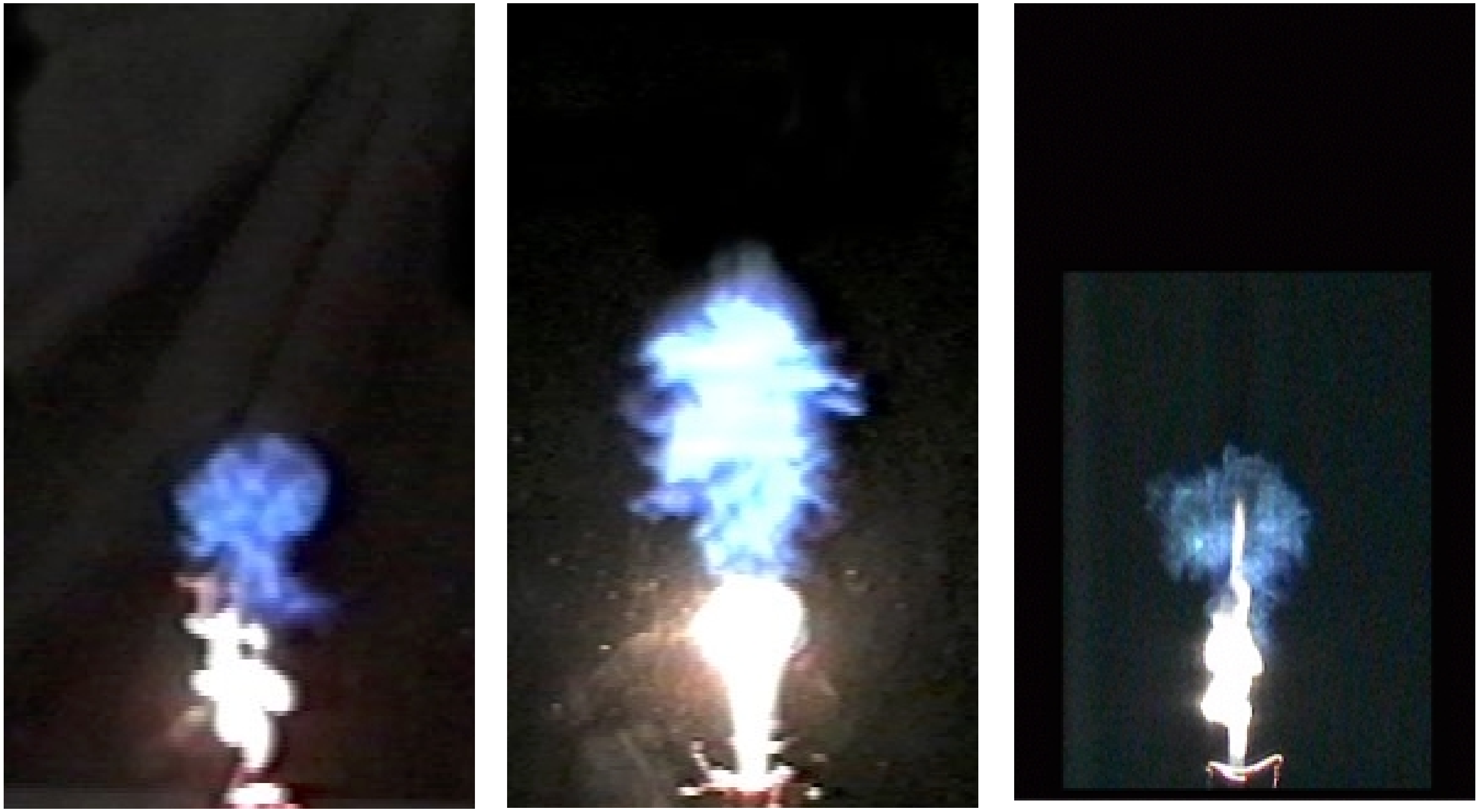

a) $U_{cof} / U_{jet} = 0$ **b)** $U_{cof} / U_{jet} = 0.026$ **c) Free Flame**

Figure 4.4: $P = 4$ **flame puff comparison,** $\tau_i = 5.745$ **ms,** $Re_{jet} = 5{,}000$**, Image Height = 25 cm**

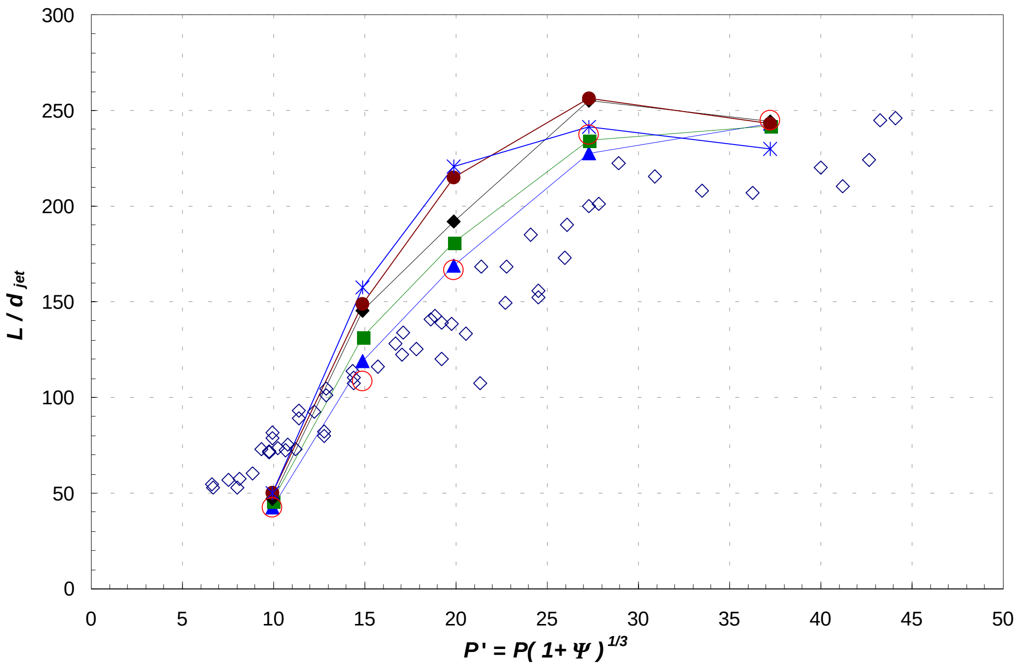

Figure 4.5: Flame length linearity with $V^{1/3}$ for non-interacting flame puffs

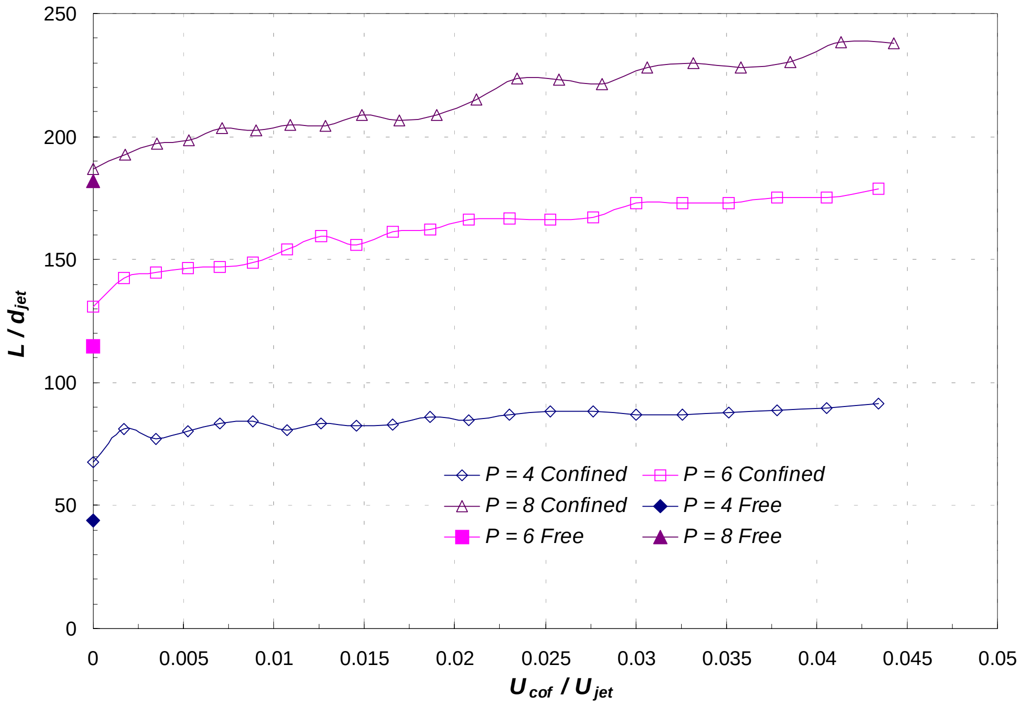

Figure 4.6: Normalized flame lengths for Re_{jet} = 3,000

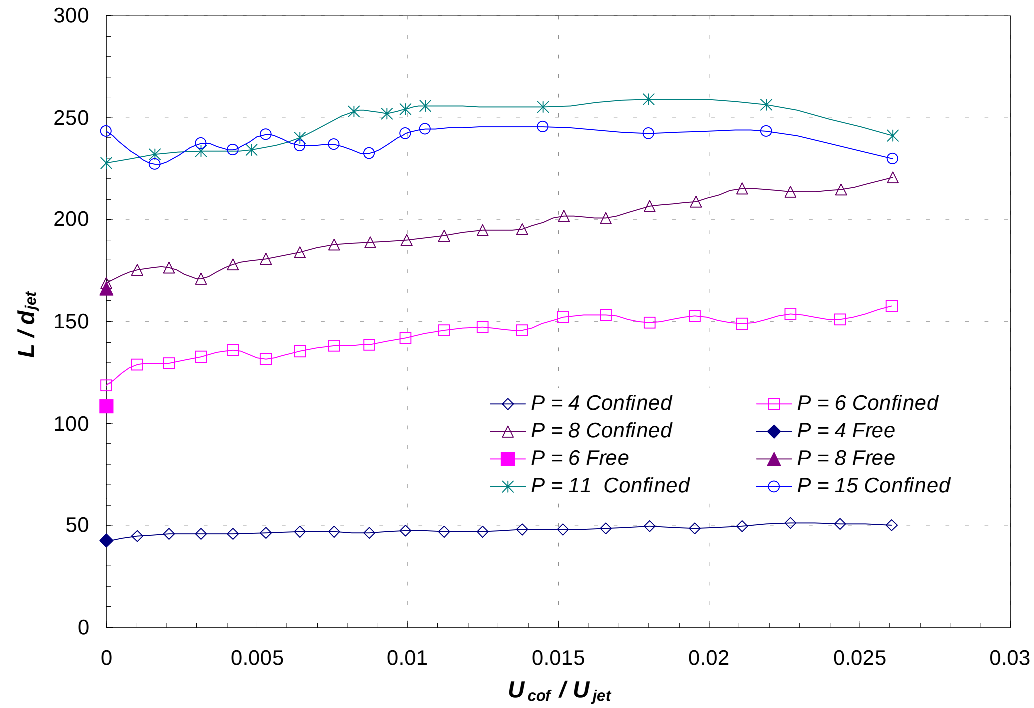

Figure 4.7: Normalized flame lengths for Re_{jet} = 5,000

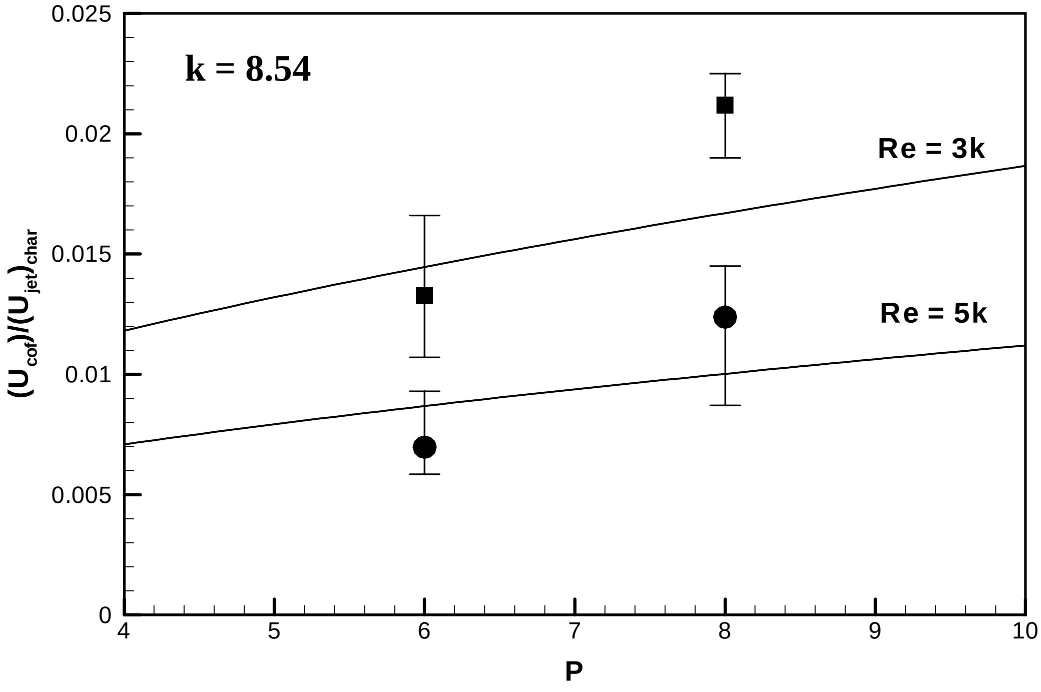

Figure 4.8: Co-flow scaling plot for non-interacting flames

***P* = 4, α_{inj} = 0.1** **_P_ = 4, α_{inj} = 0.3** **_P_ = 4, α_{inj} = 0.5**

Figure 5.1: *P* = 4 interacting flame series, τ_i = 5.745, Image Height = 40.3 cm

***P* = 5, α_{inj} = 0.15**
Height = 32 cm

***P* = 6, α_{inj} = 0.2**
Height = 33.3 cm

***P* = 8, α_{inj} = 0.4**
Height = 49 cm

Figure 5.2: *P* = 5, 6, and 8 double flame puffs

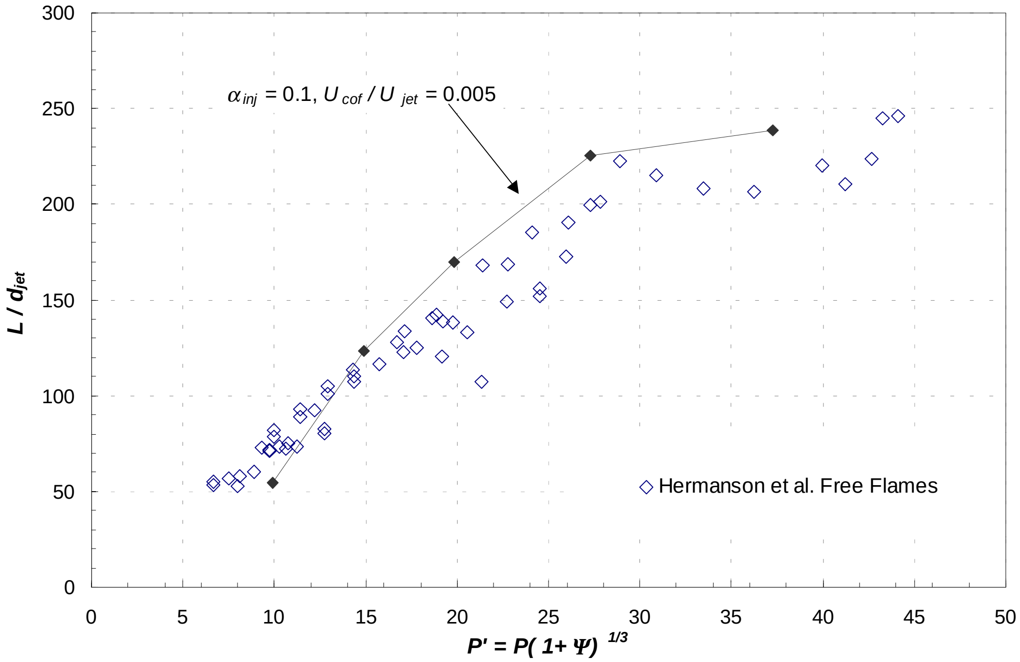

Figure 5.3: Flame length linearity with $V^{1/3}$ for interacting flame puffs

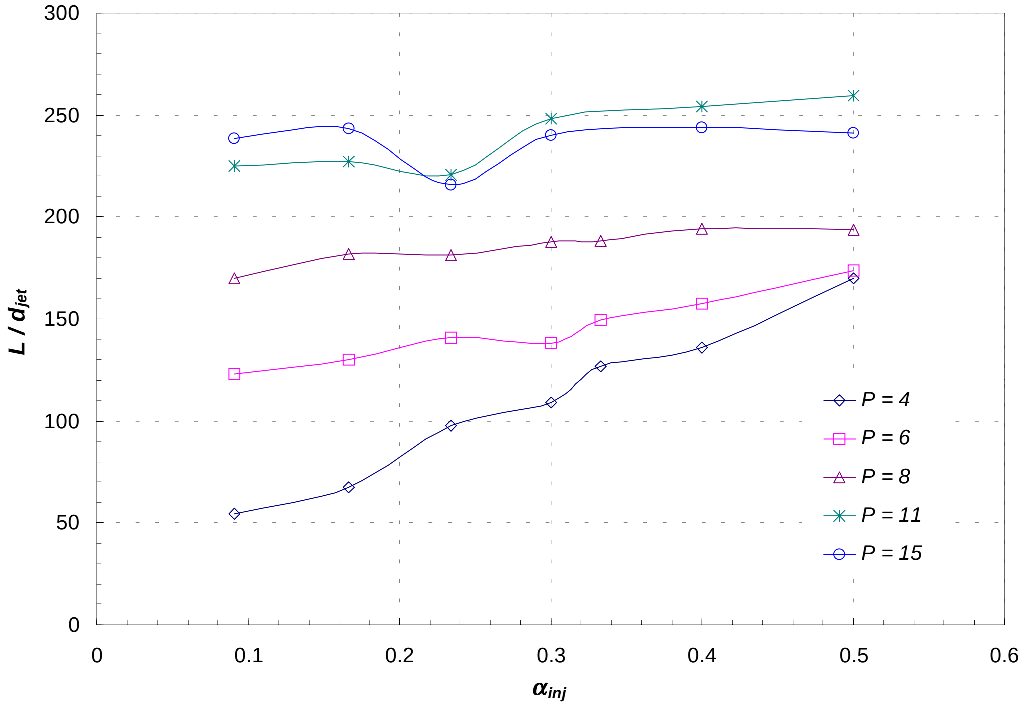

Figure 5.4: Normalized flame length for Re_{jet} = 5,000 and U_{cof} / U_{jet} = 0.005

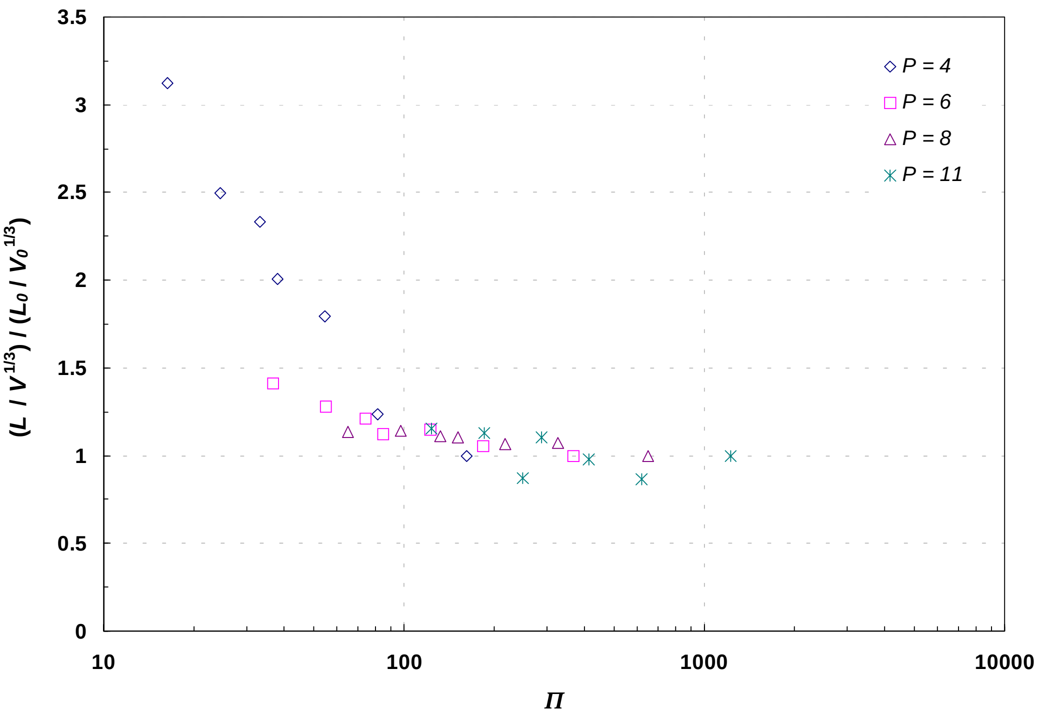

Figure 5.5: Normalized flame length vs. interaction parameter

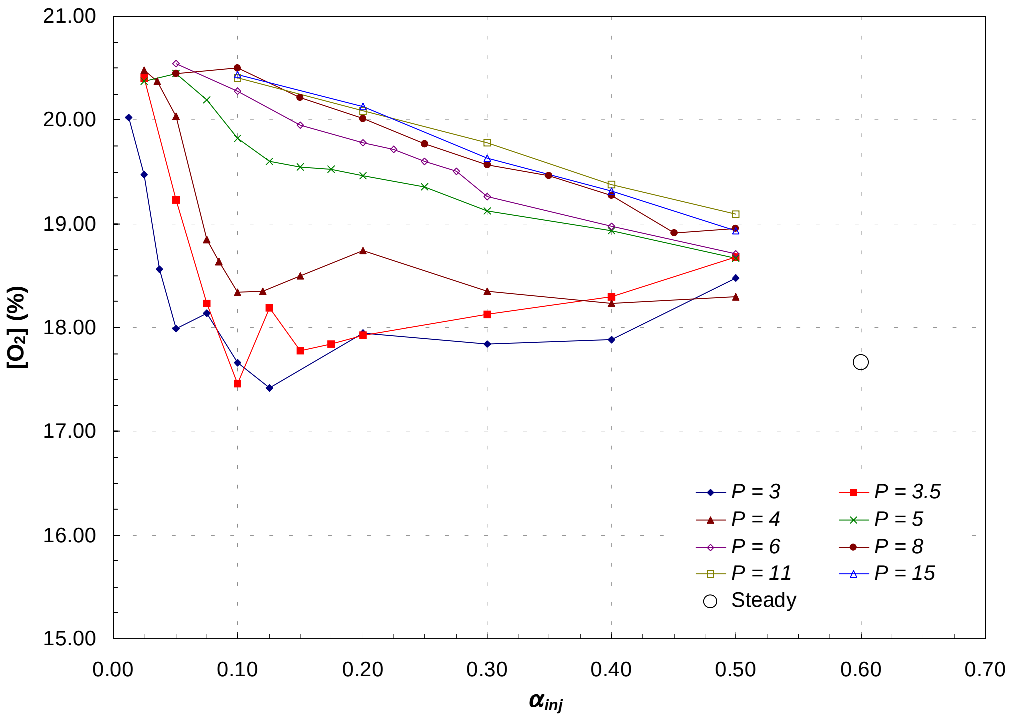

Figure 6.1: Average O_2 concentrations

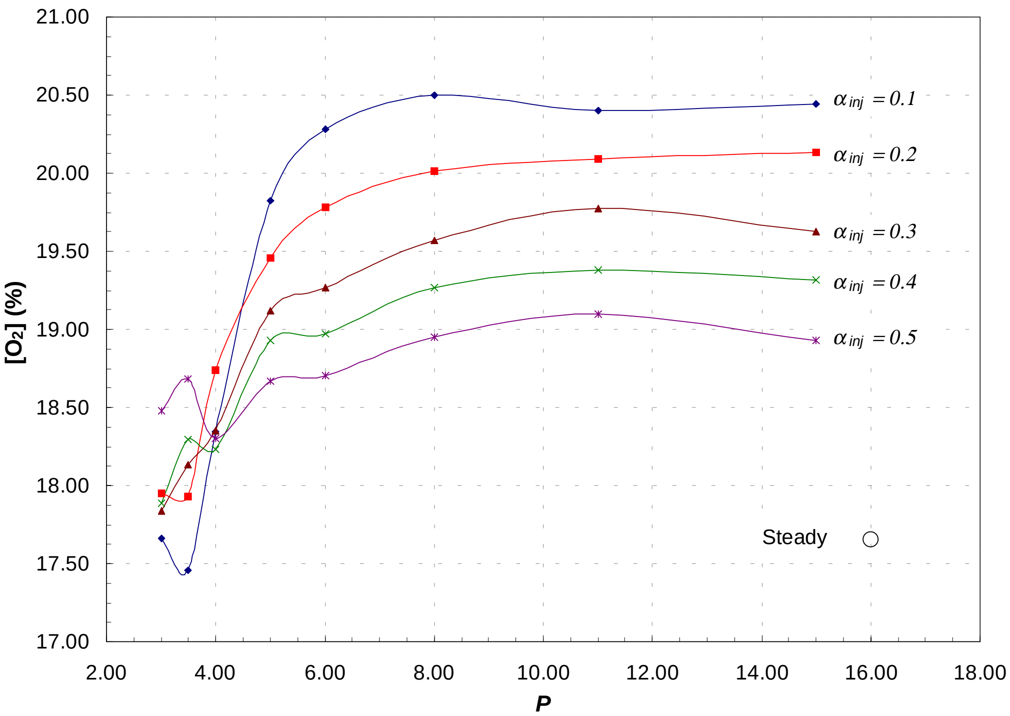

Figure 6.2: Average O_2 concentrations vs. pulse parameter, P

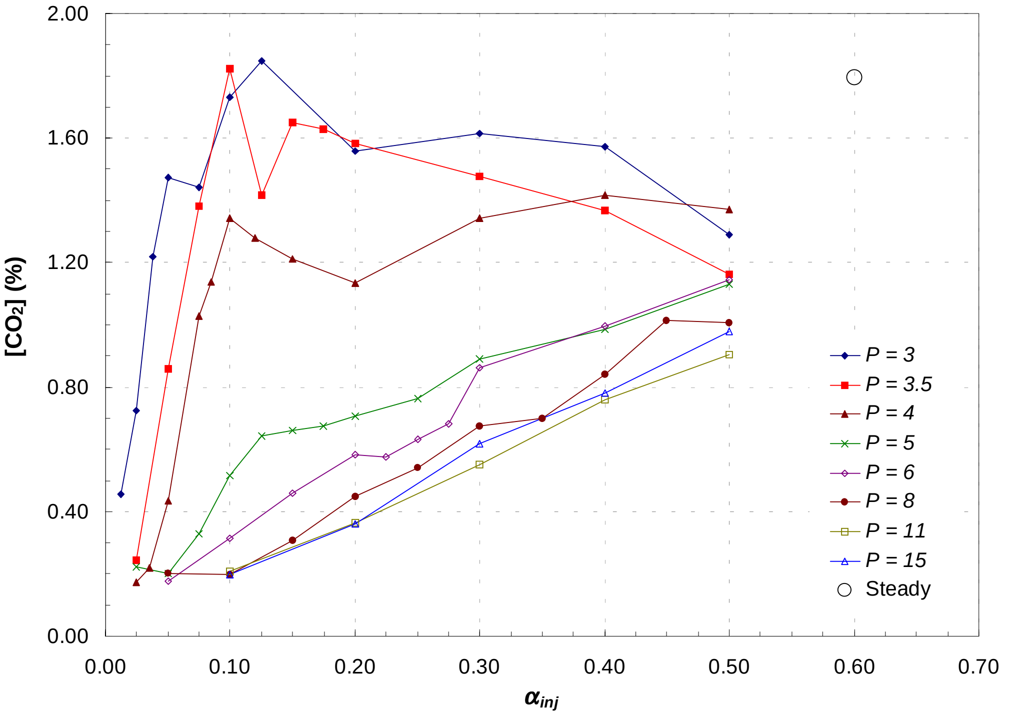

Figure 6.3: Average CO_2 concentrations

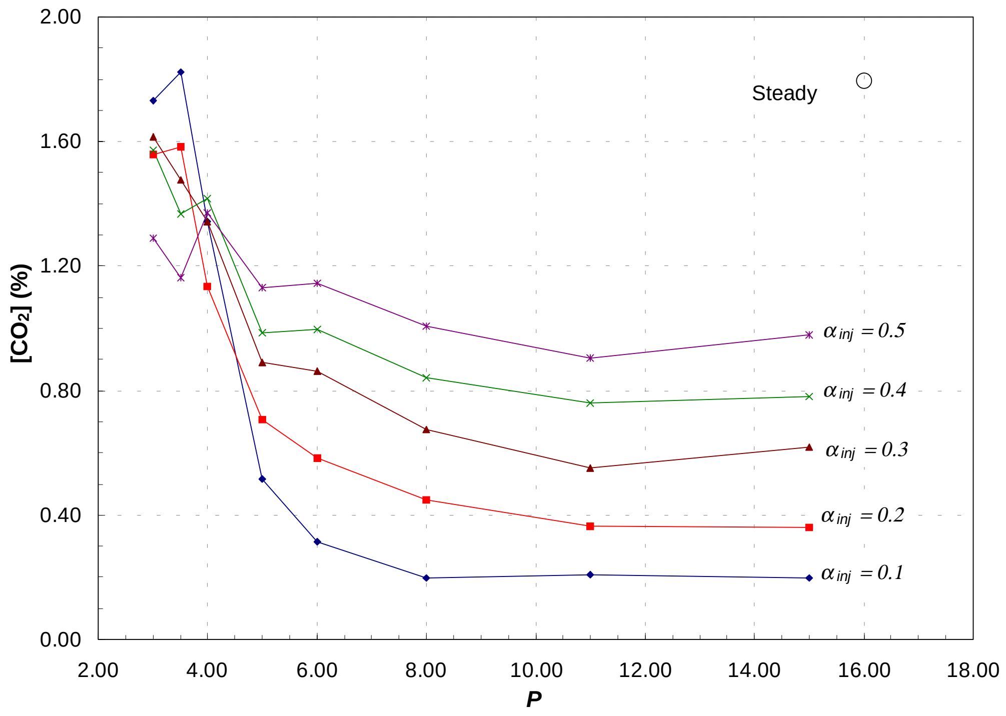

Figure 6.4: Average CO_2 concentrations vs. pulse parameter, *P*

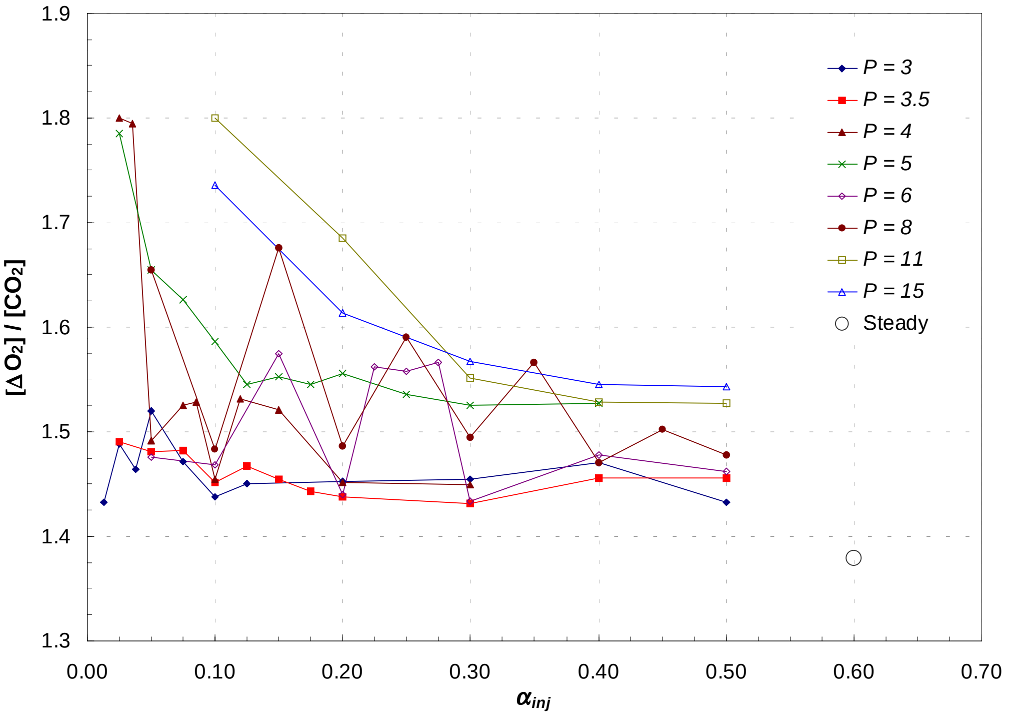

Figure 6.5: Normalized O_2 concentrations

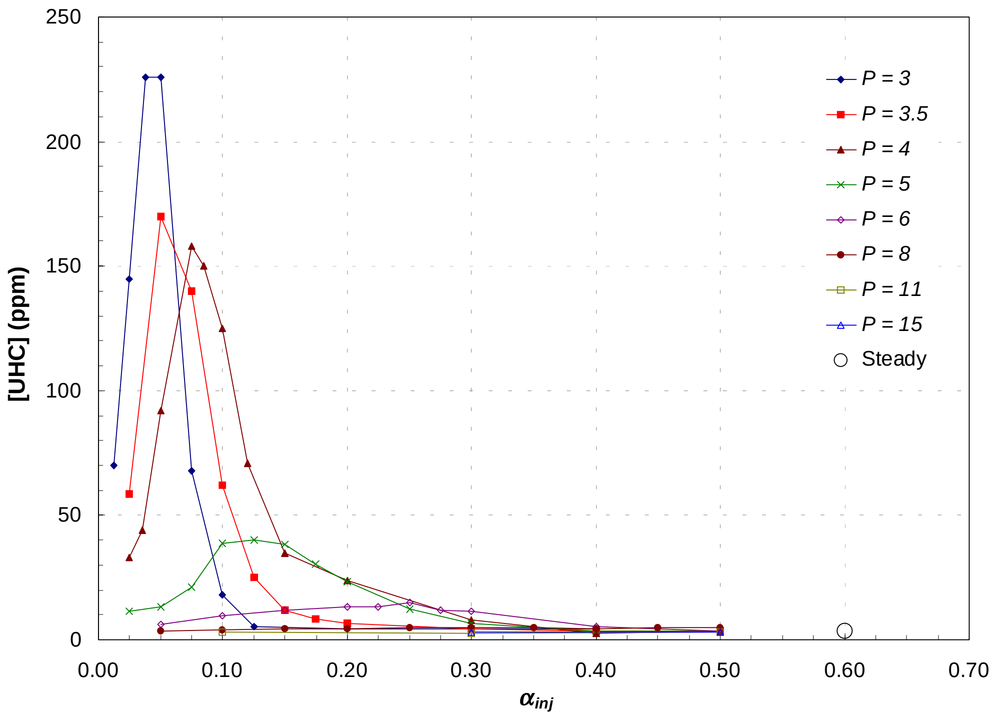

Figure 6.6: Average UHC concentration

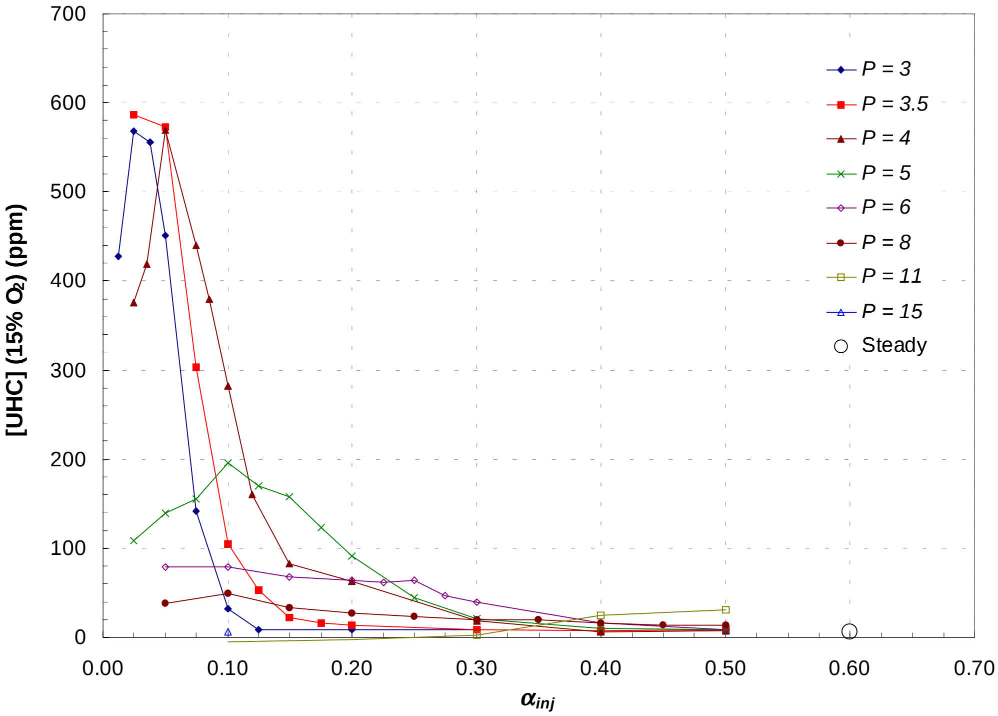

Figure 6.7: Corrected average UHC concentrations

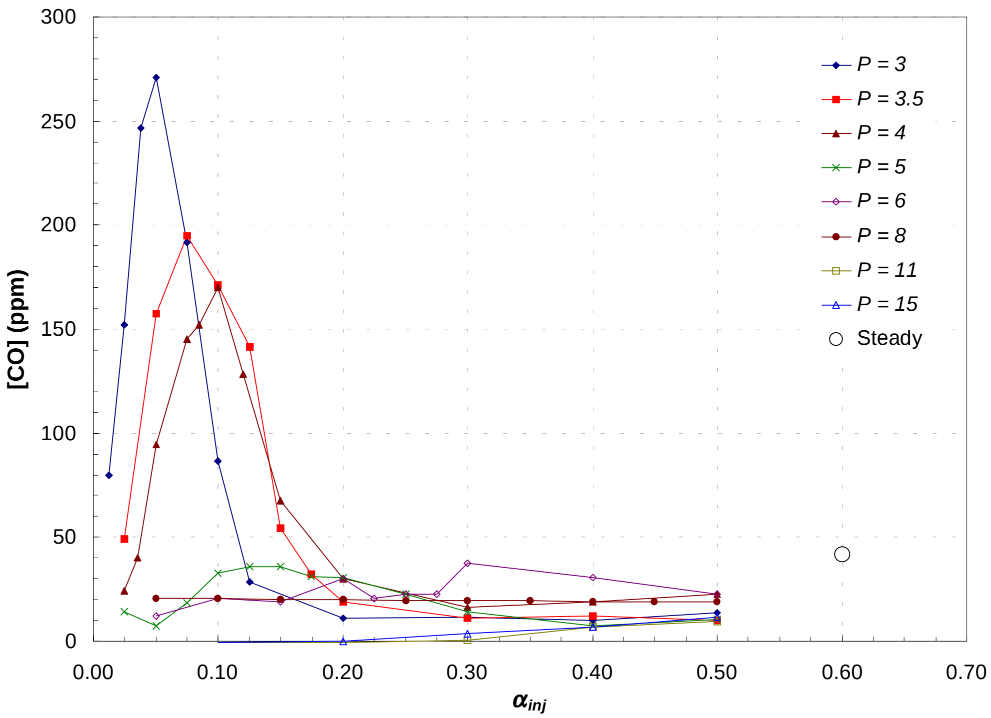

Figure 6.8: Average CO concentrations

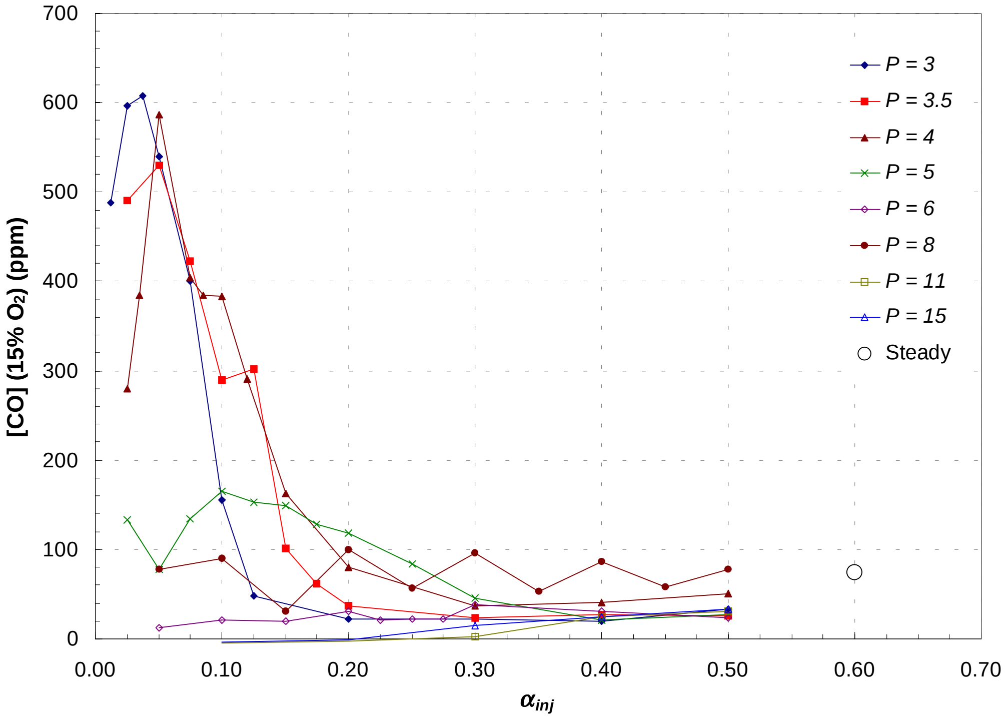

Figure 6.9: Corrected average
CO concentrations

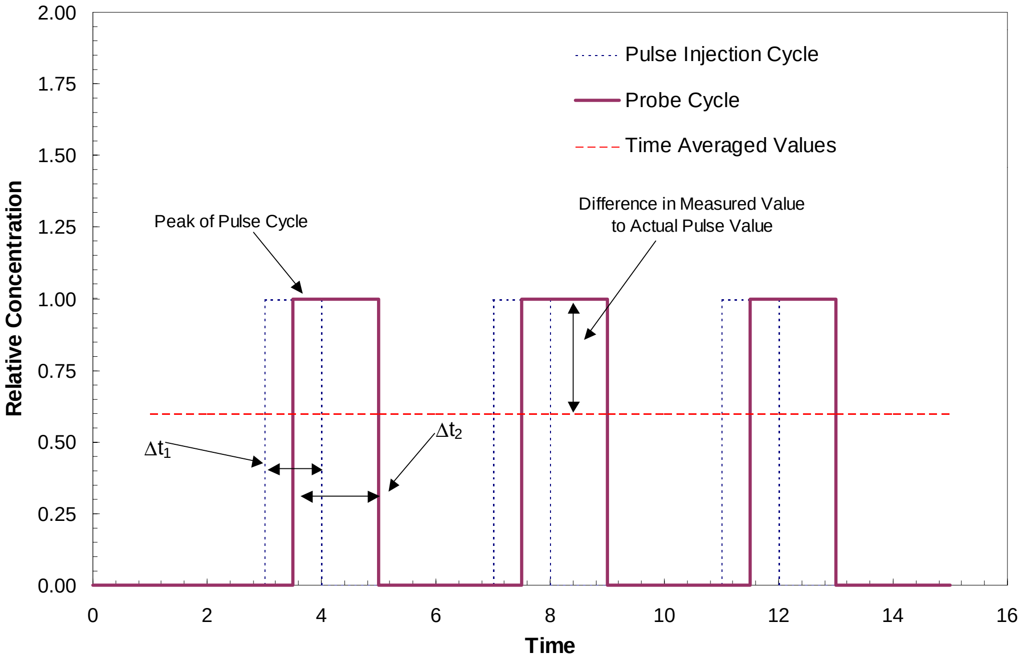

Figure 6.10: Graphic explanation of the difference between α_{inj} and α_{act}

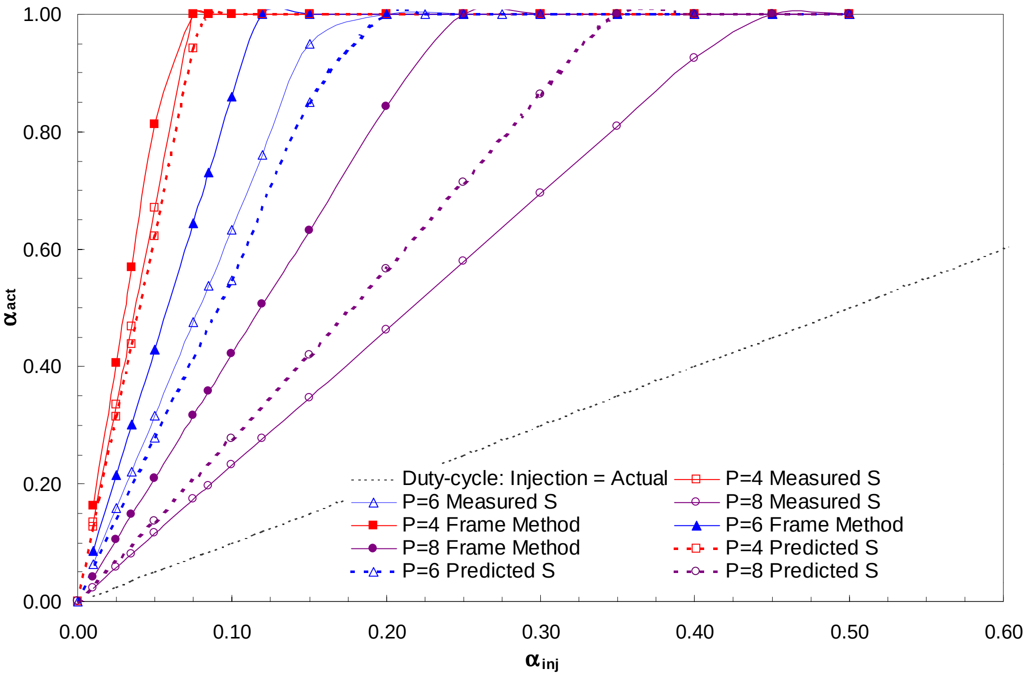

Figure 6.11: Comparison between the injection duty-cycle and the effective duty-cycle experienced by the probe

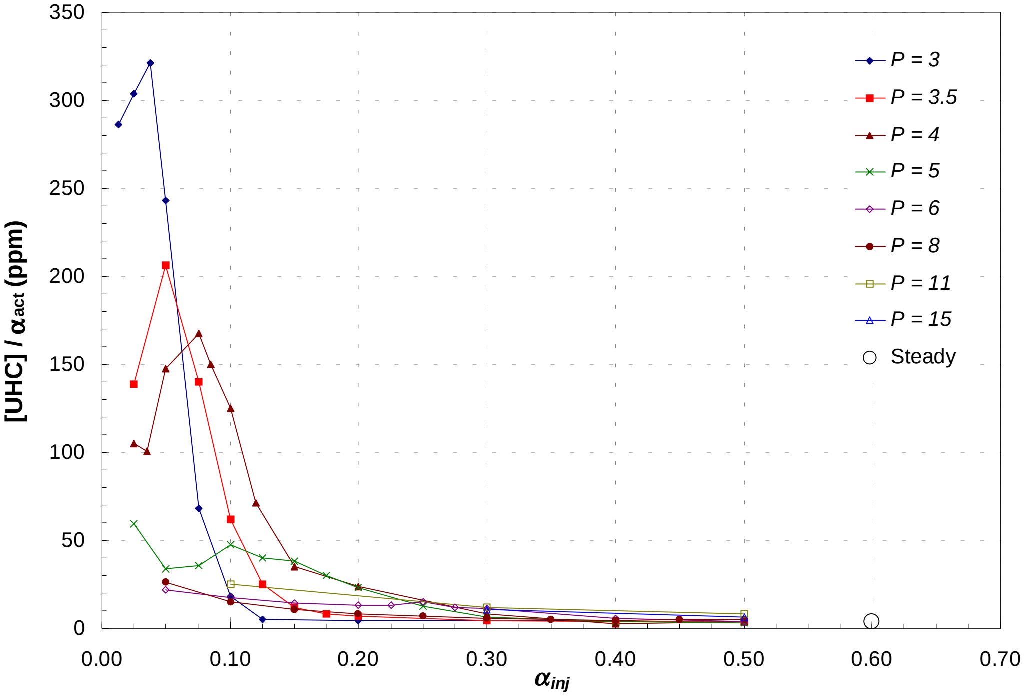

Figure 6.12: Duty-cycle corrected UHC concentrations

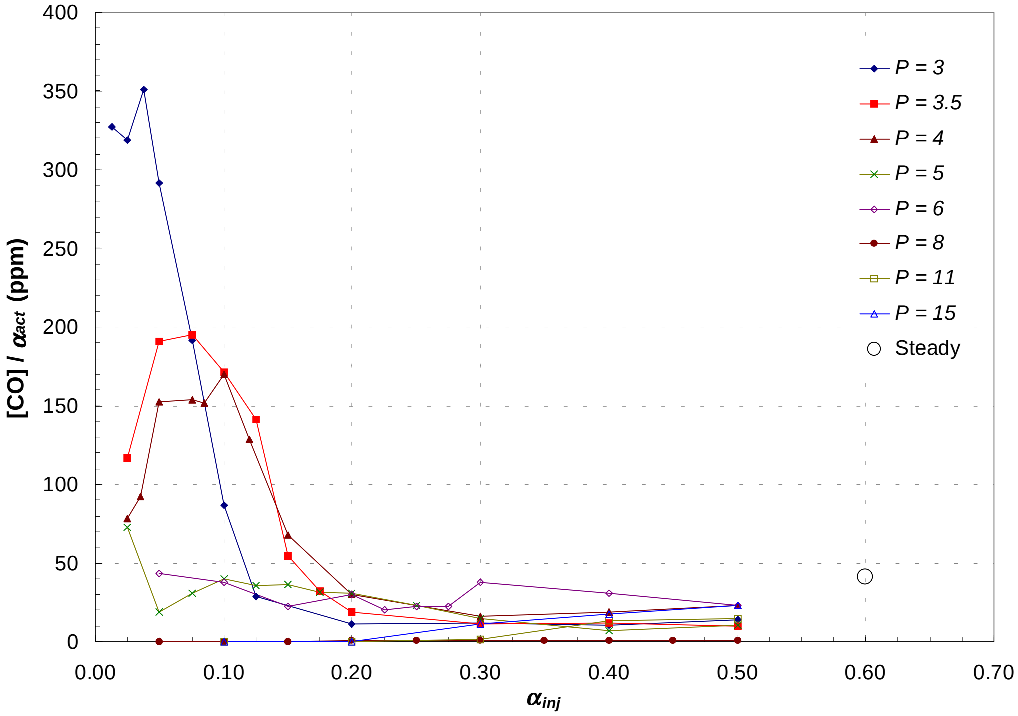

Figure 6.13: Duty-cycle corrected CO concentrations

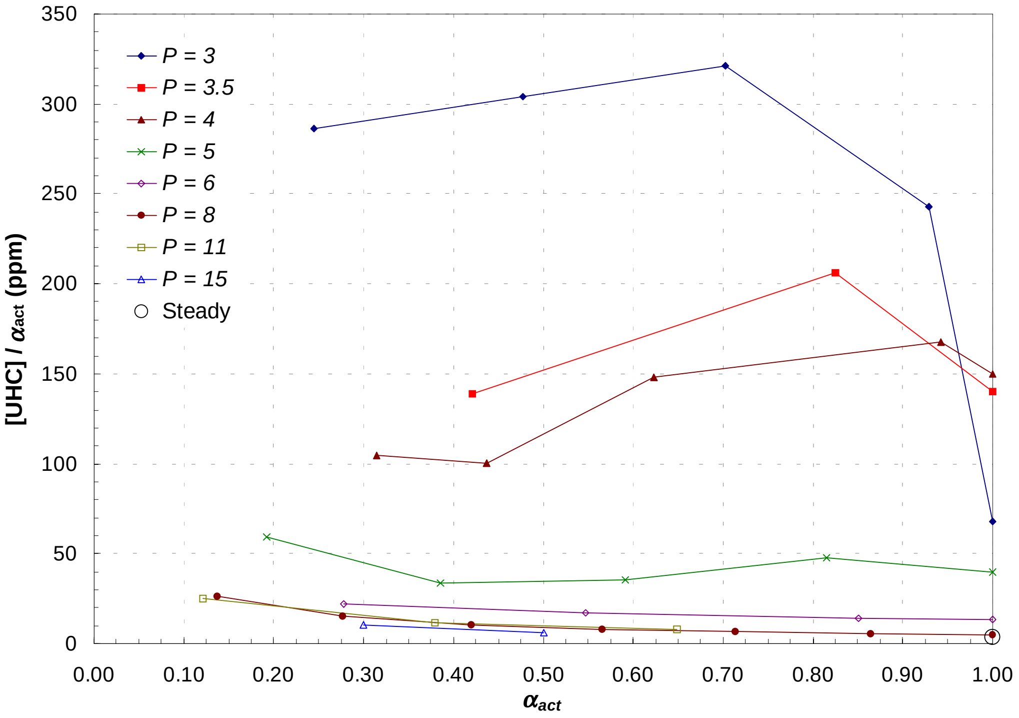

Figure 6.14: Duty-cycle corrected UHC concentrations of individual flame puffs

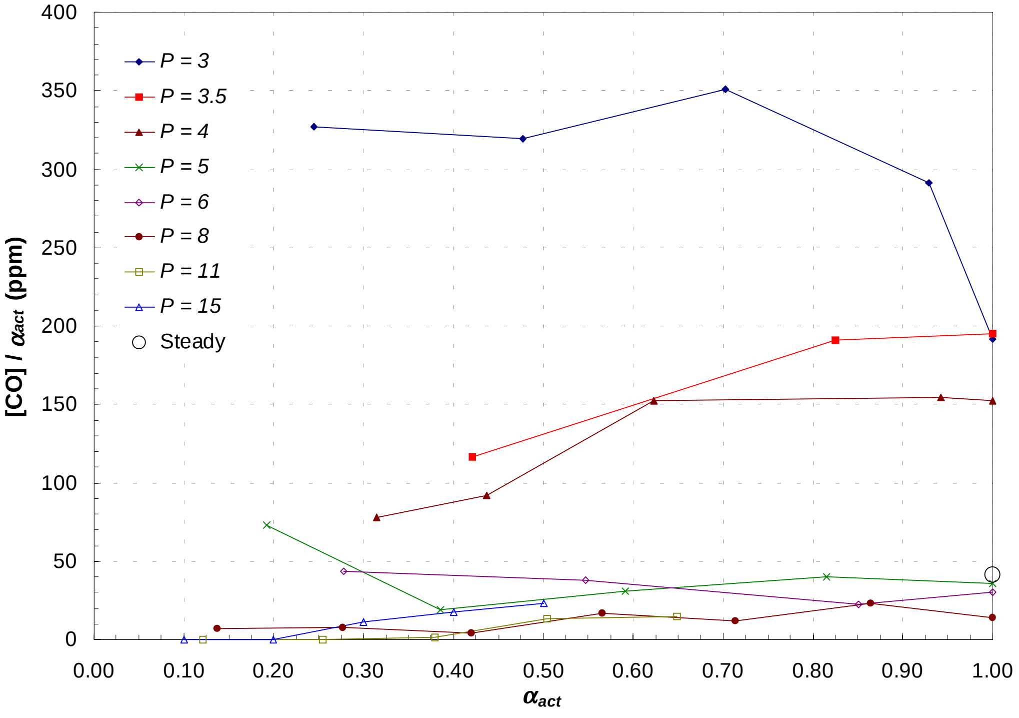

Figure 6.15: Duty-cycle corrected CO concentrations of individual flame puffs

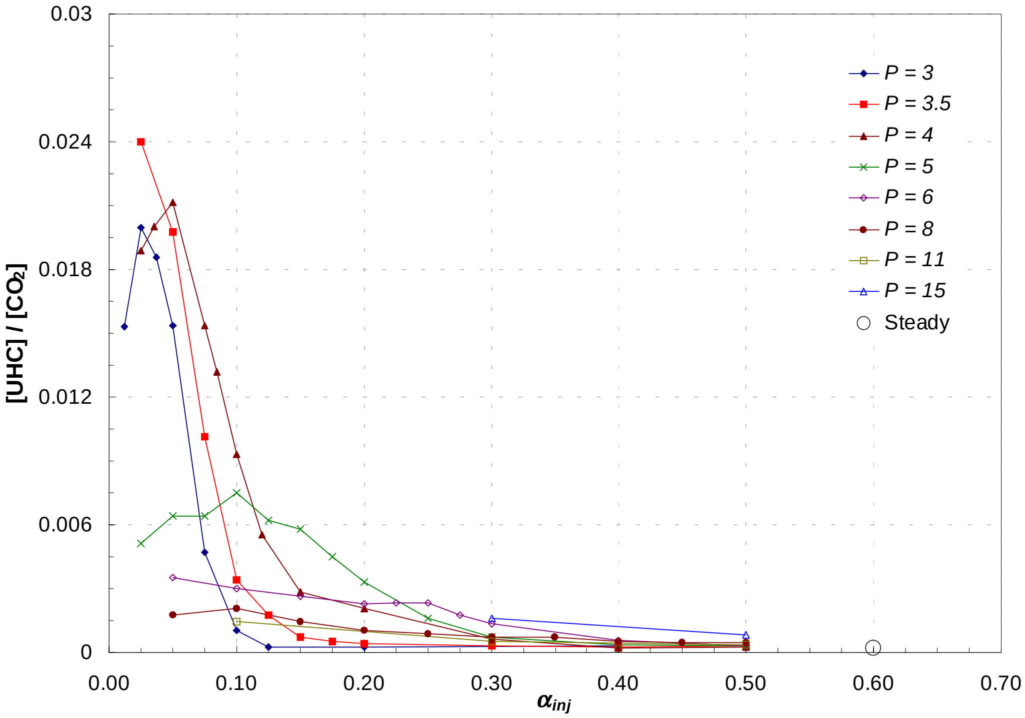

Figure 6.16: Normalized UHC concentrations

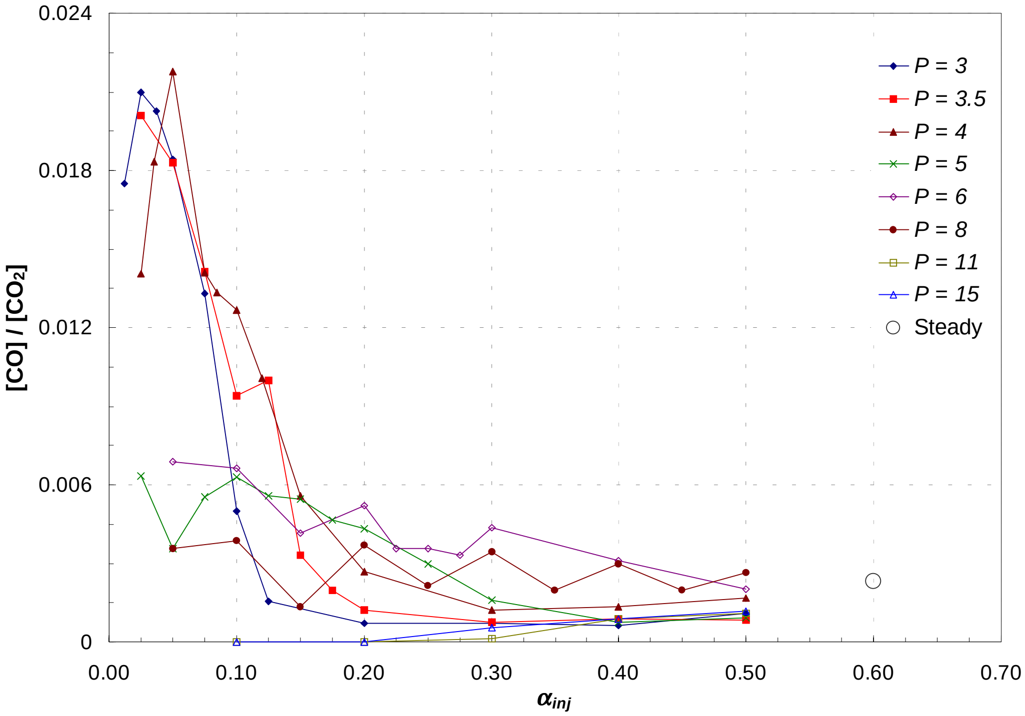

Figure 6.17: Normalized CO concentrations

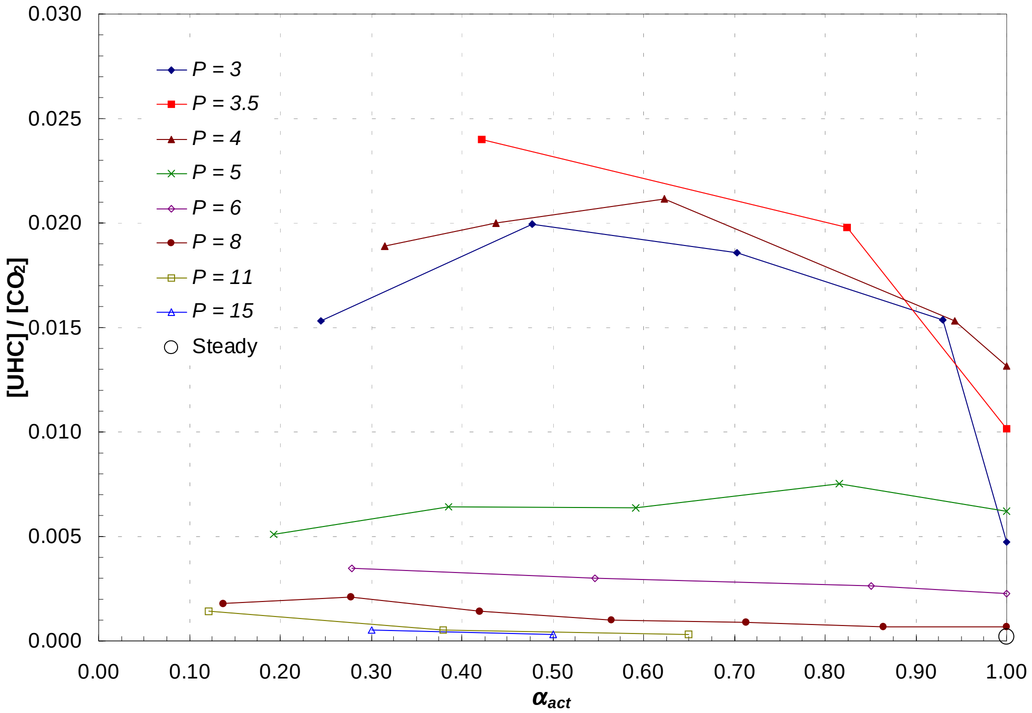

Figure 6.18: Normalized UHC concentrations of individual flame puffs

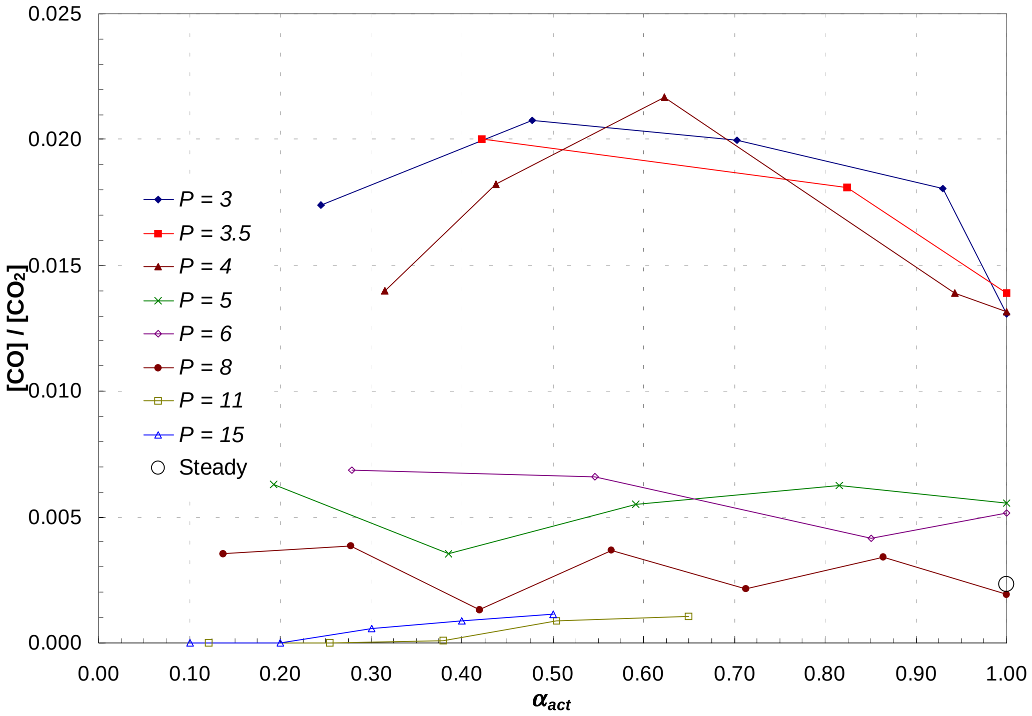

Figure 6.19: Normalized CO concentrations of individual flame puffs

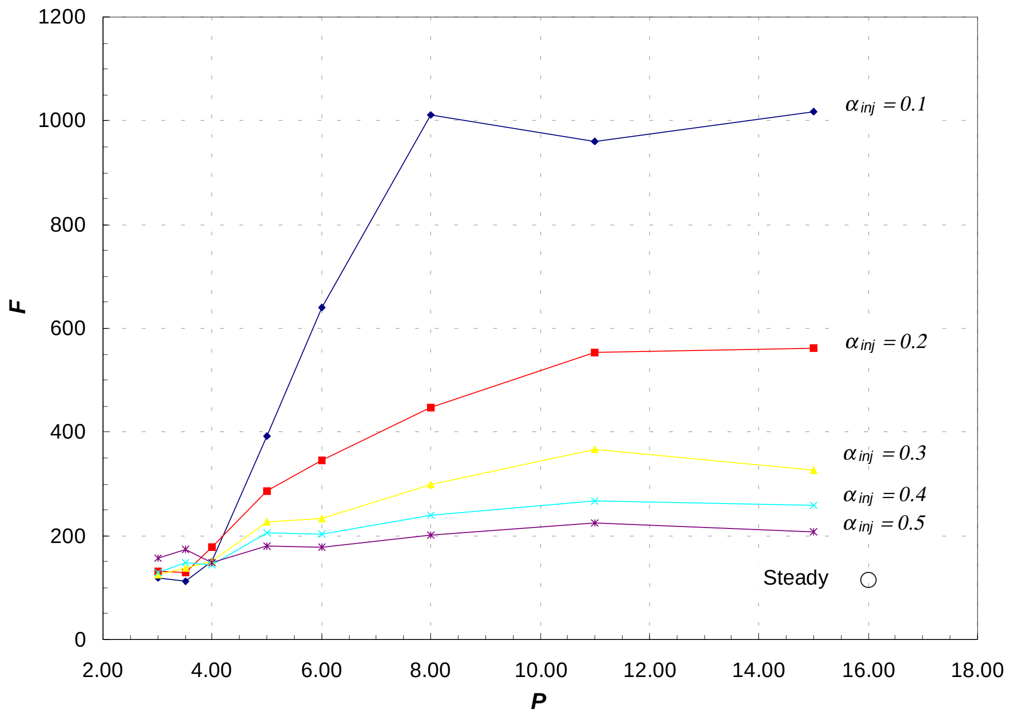

Figure 6.20: Centerline air/fuel ratio vs. pulse parameter, *P*

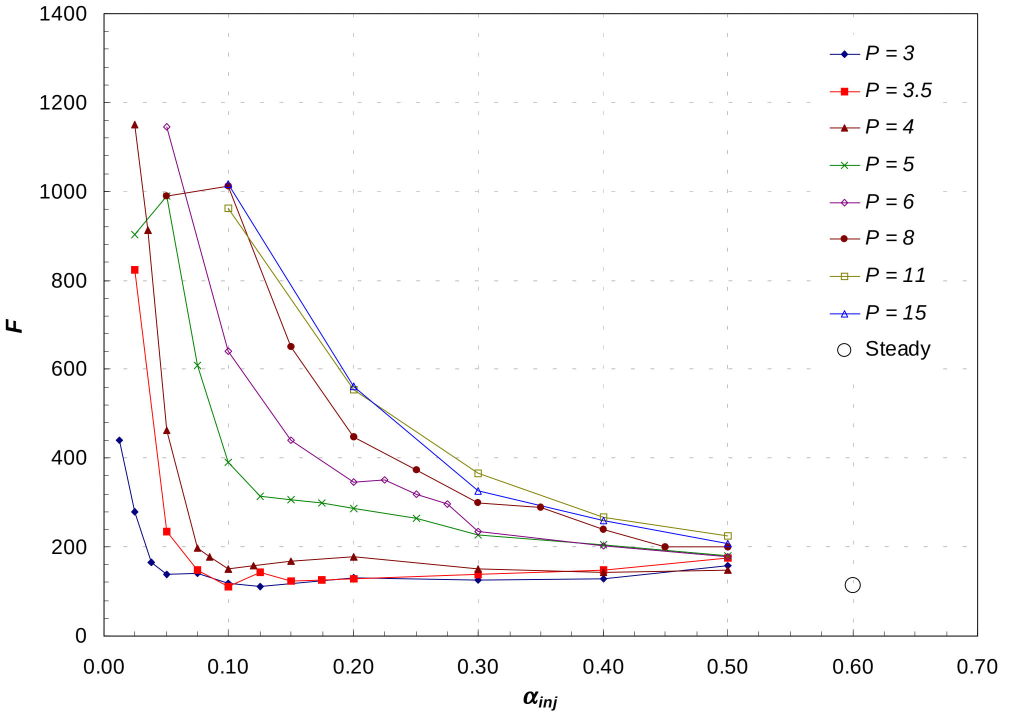

Figure 6.21: Centerline air/fuel ratio

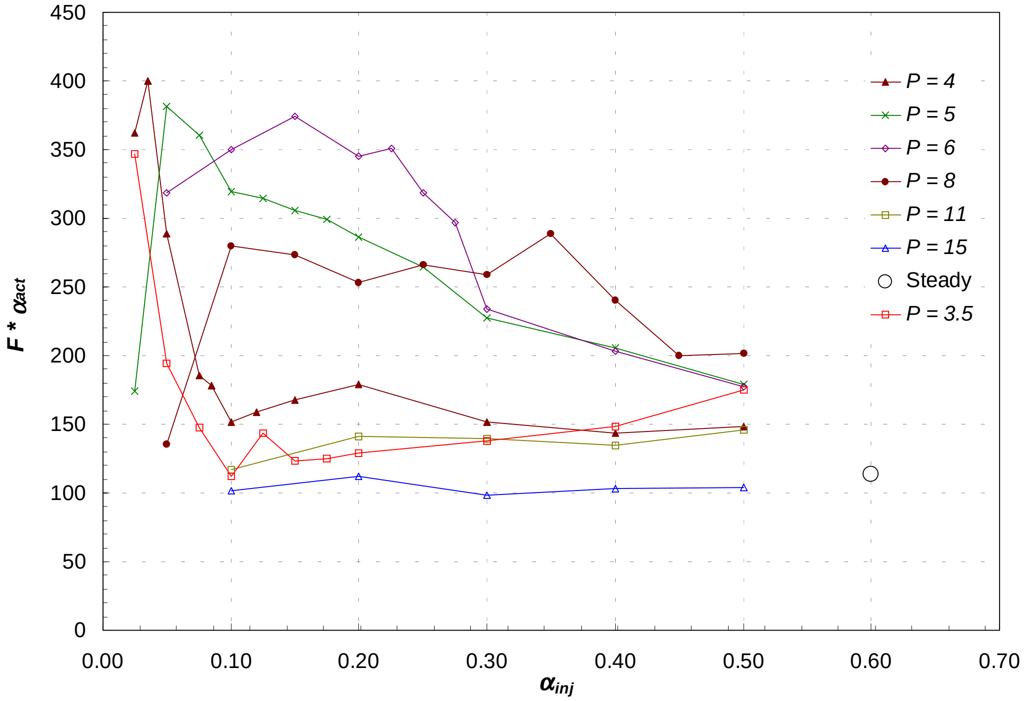

Figure 6.22: Duty-cycle corrected air/fuel ratio

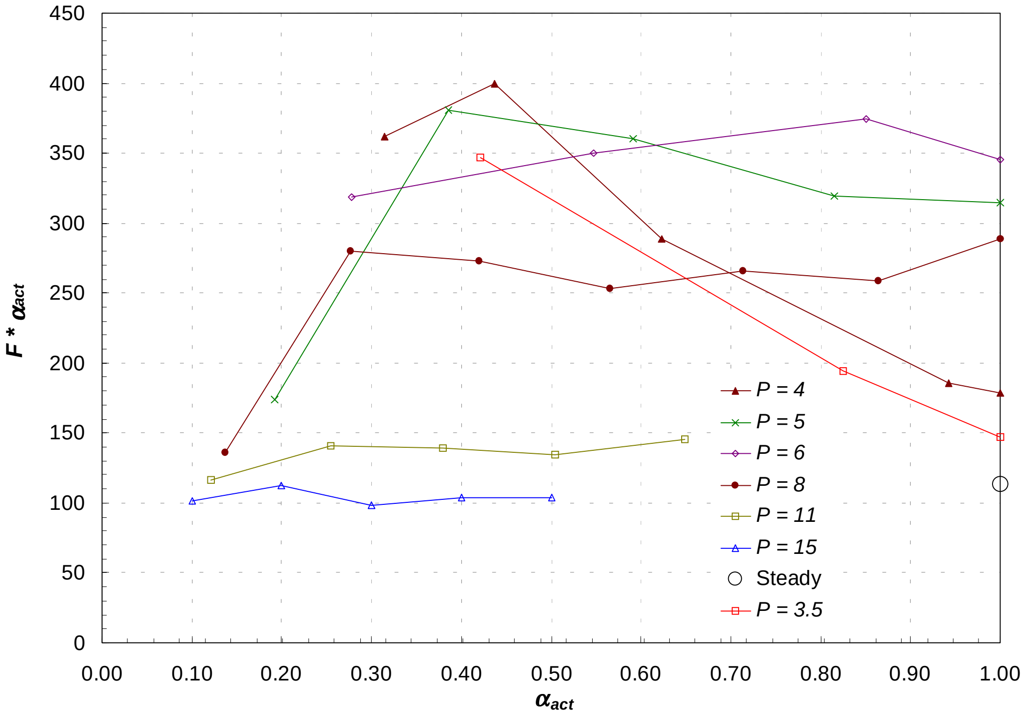

Figure 6.23: Duty-cycle corrected air/fuel ratio of individual flame puffs

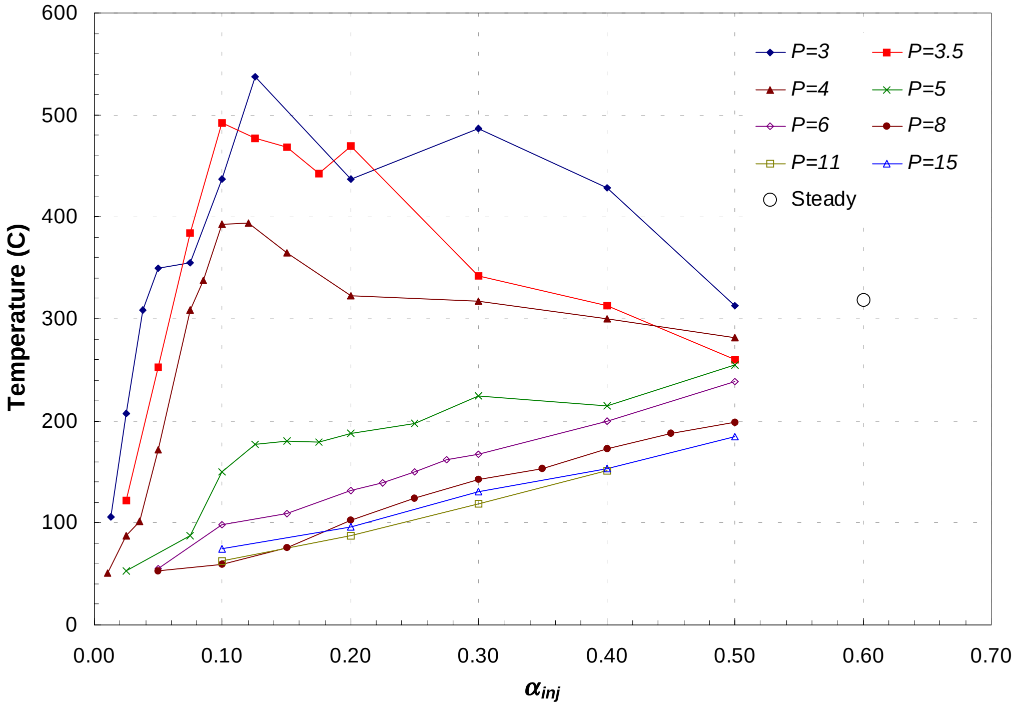

Figure 6.24: Average temperature

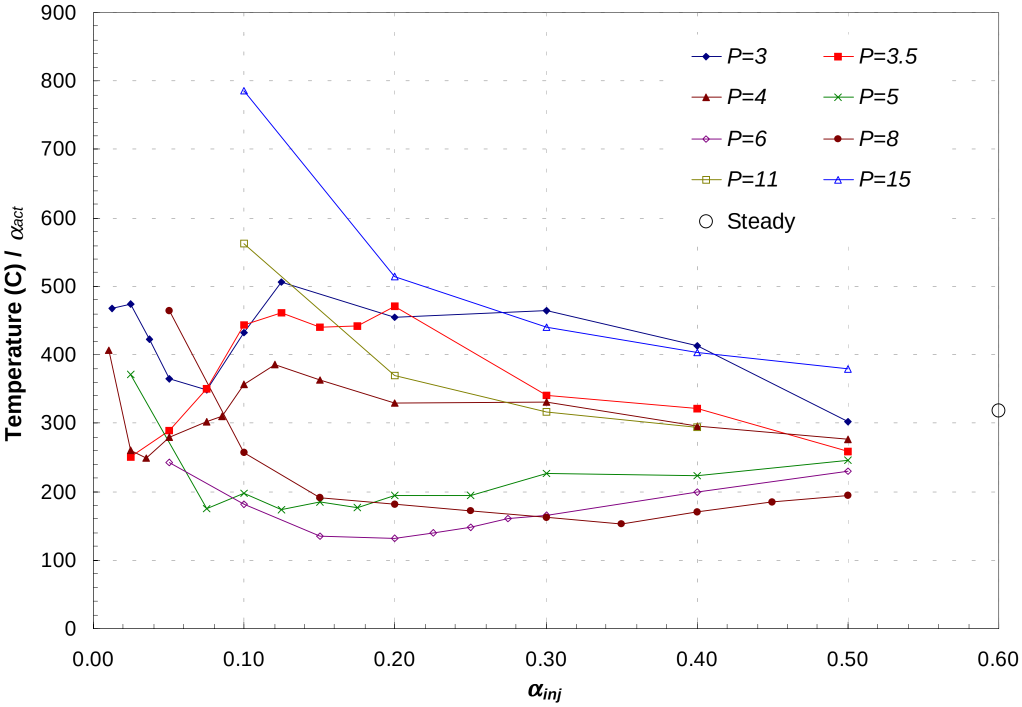

Figure 6.25: Duty-cycle corrected temperature

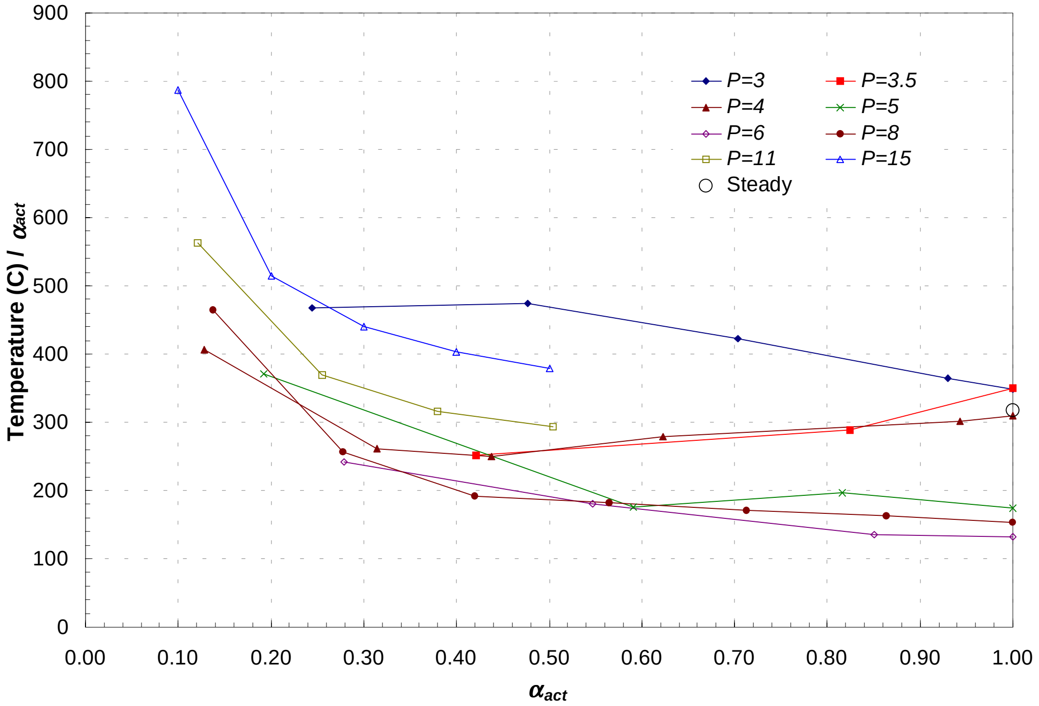

Figure 6.26: Duty-cycle corrected temperature of individual flame puffs

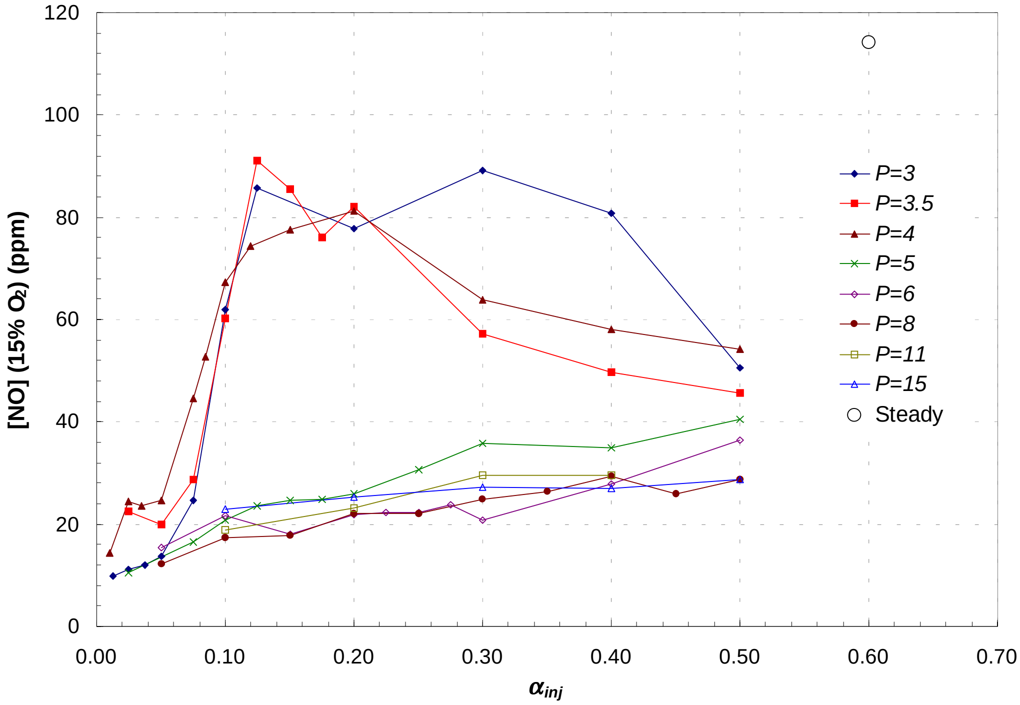

Figure 6.27: Corrected average NO concentrations

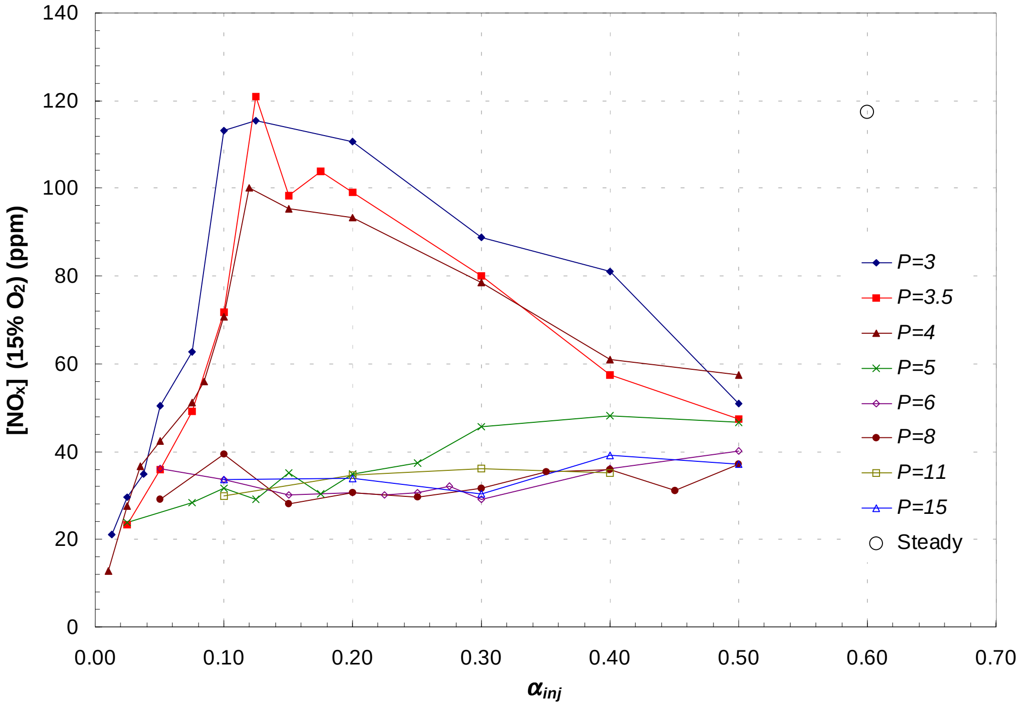

Figure 6.28: Corrected average NO$_x$ concentrations

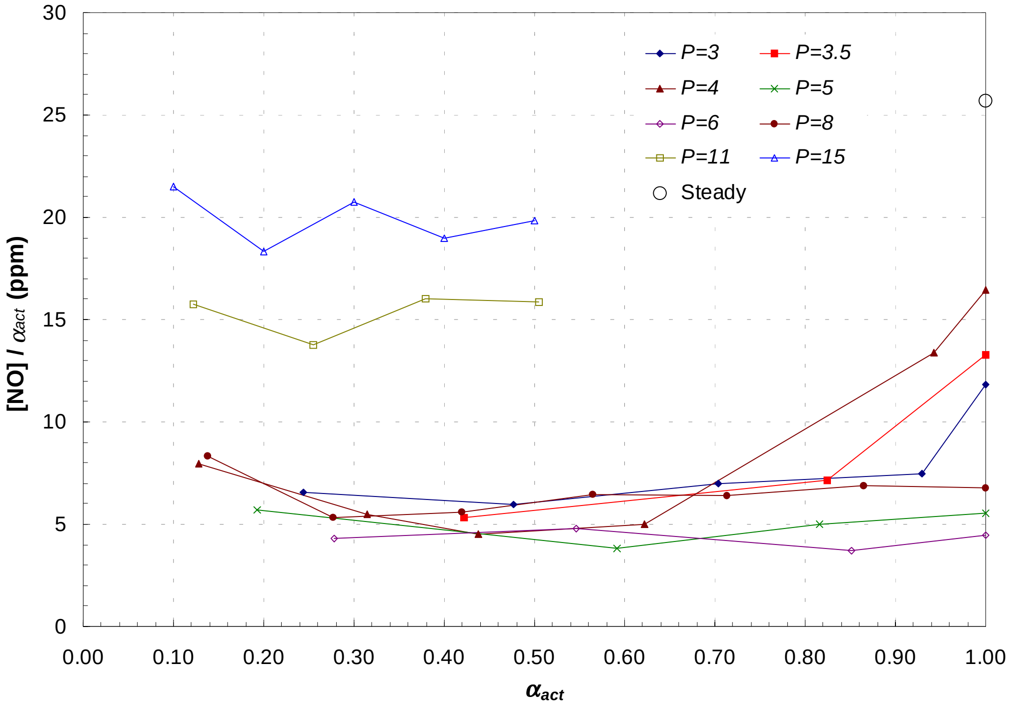

Figure 6.29: Duty-cycle corrected centerline NO of individual flame puffs

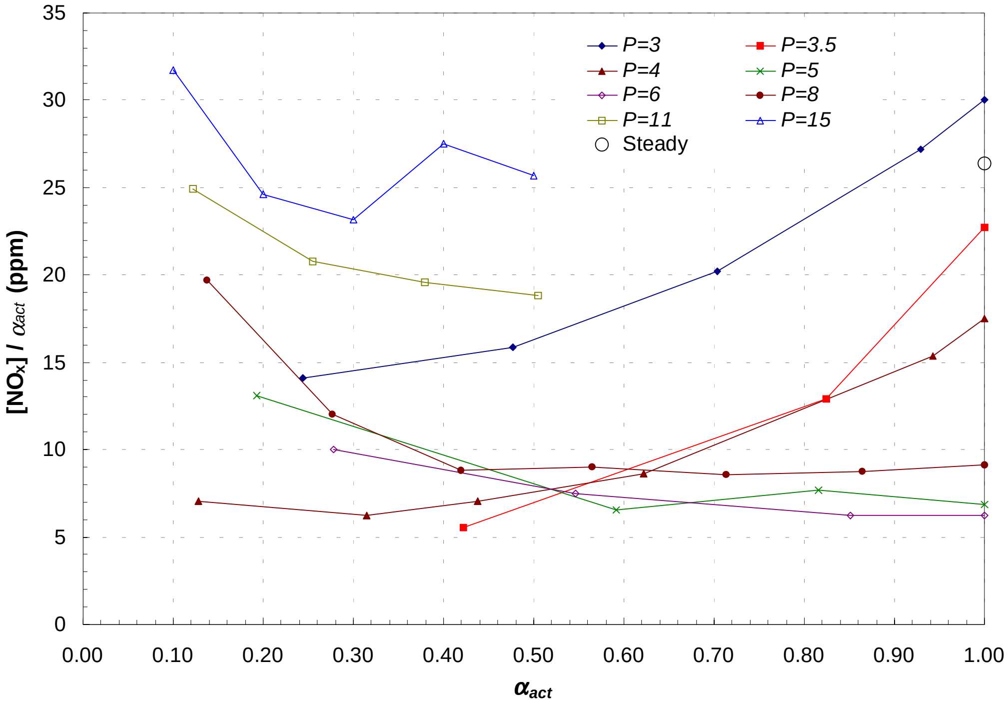

Figure 6.30: Duty-cycle corrected centerline NO_x of individual flame puffs

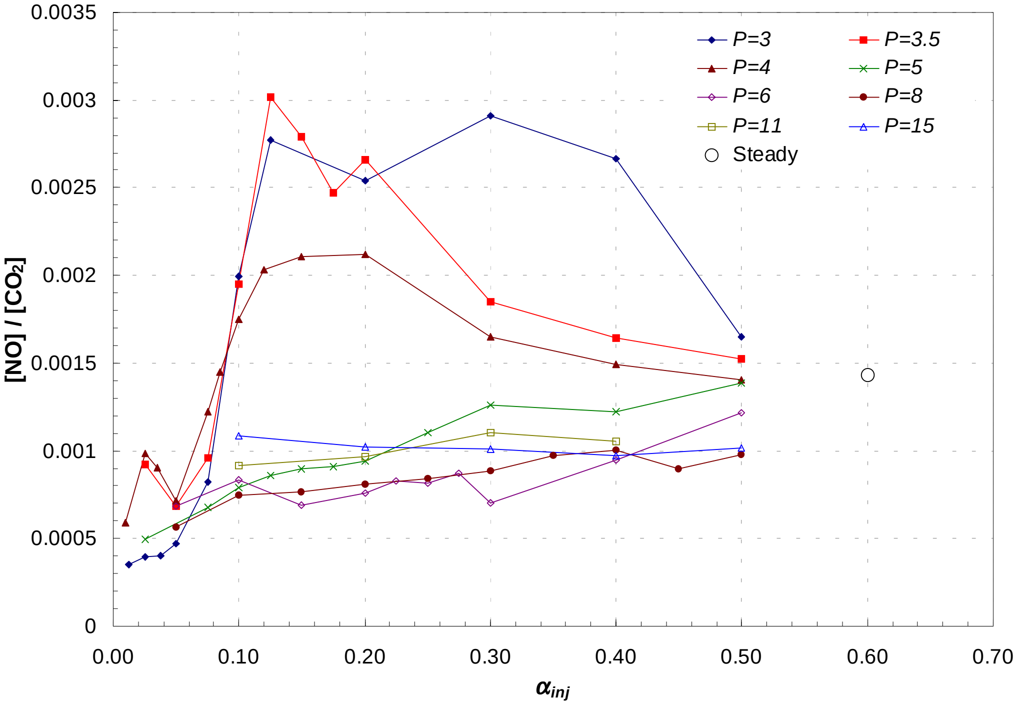

Figure 6.31: Normalized NO concentrations

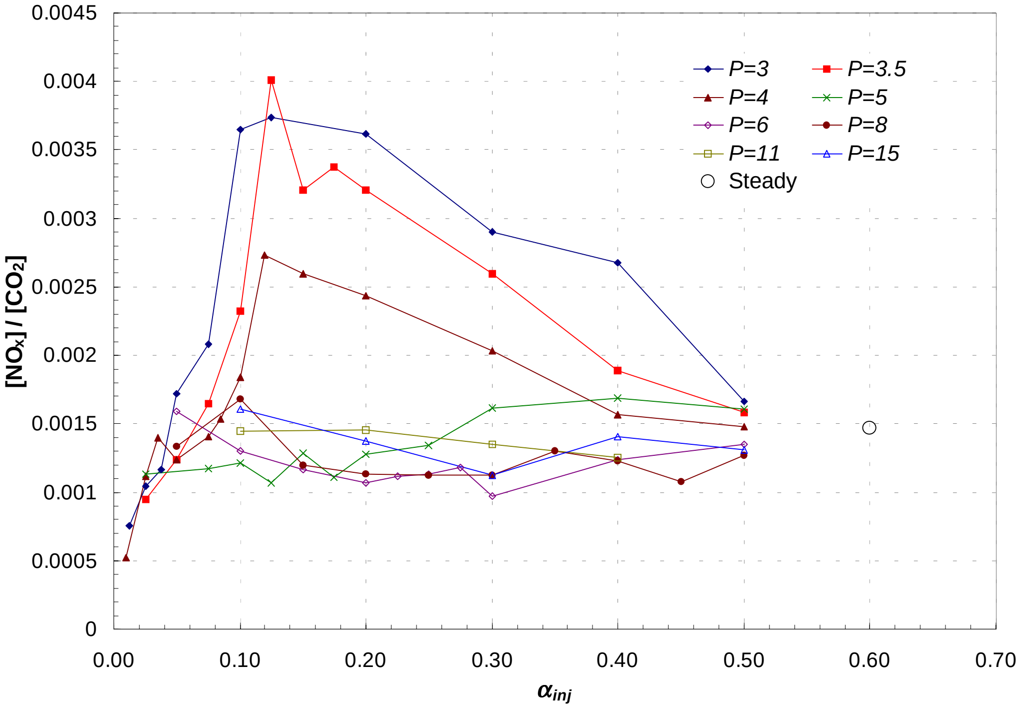

Figure 6.32: Normalized NO_x concentrations

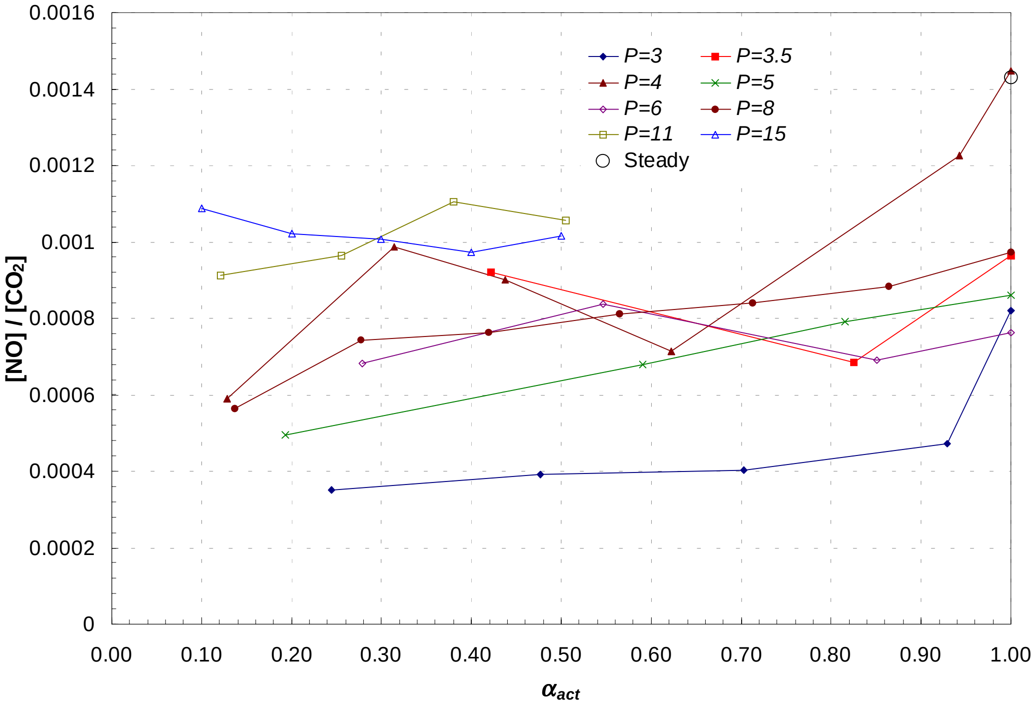

Figure 6.33: Normalized NO concentrations of individual flame puffs

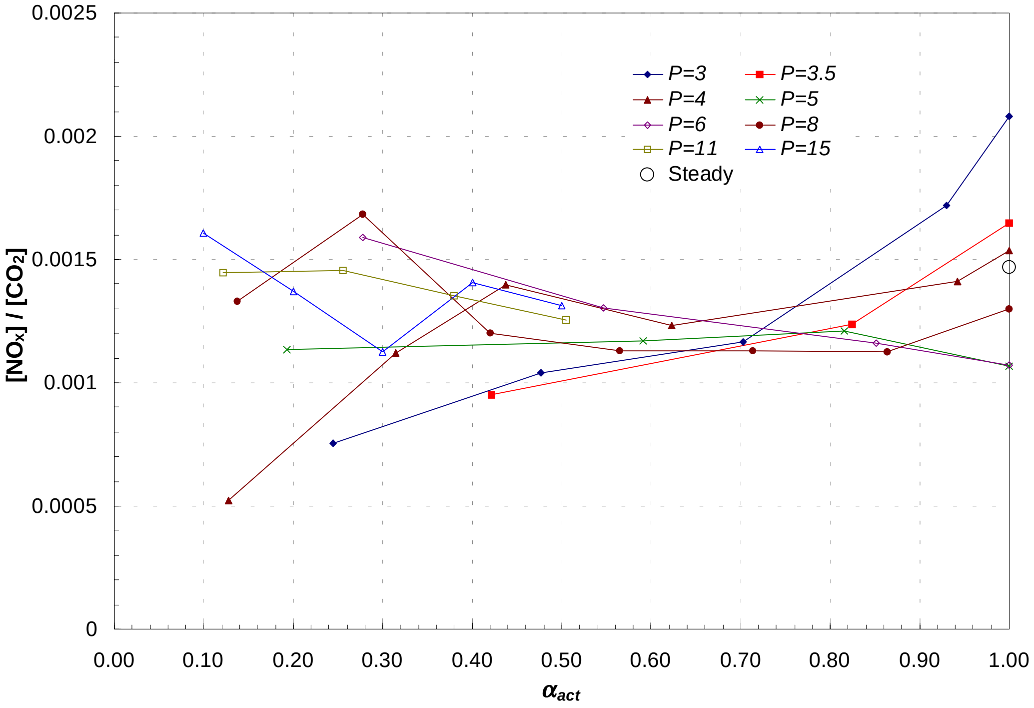

Figure 6.34: Normalized NO$_x$ concentrations of individual flame puffs

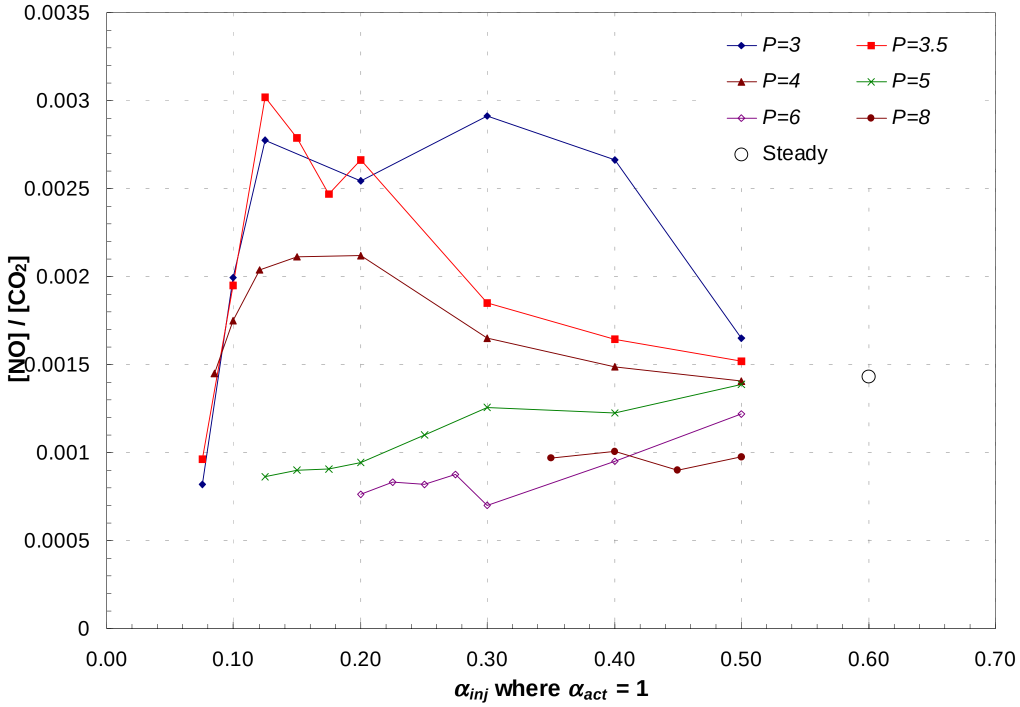

Figure 6.35: Normalized concentrations NO of interacting flame puffs

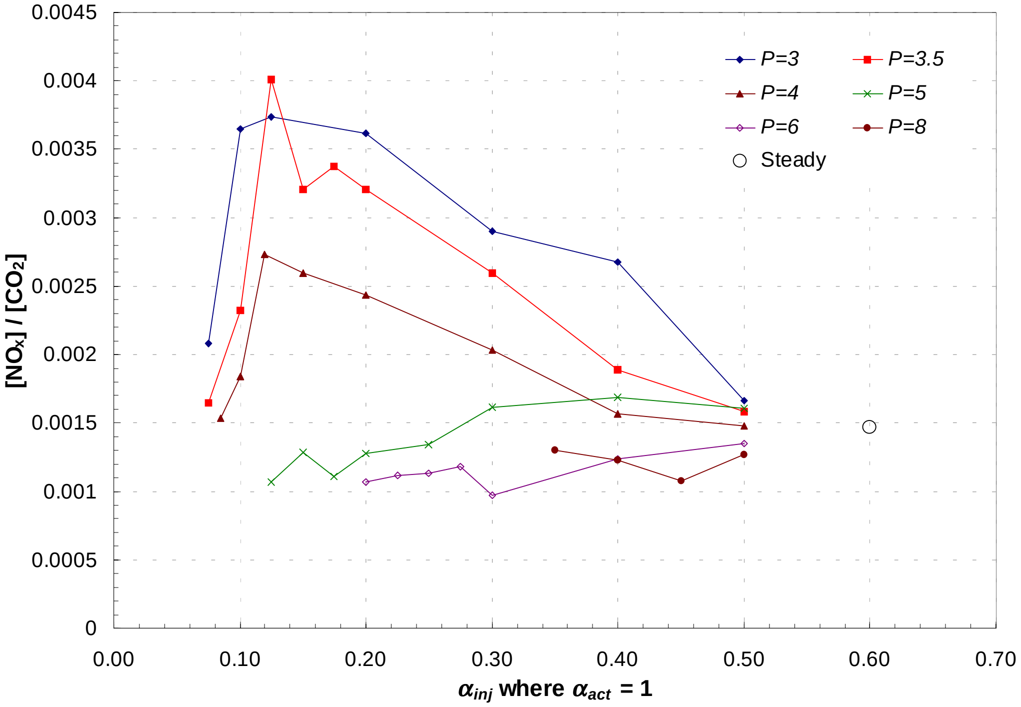

Figure 6.36: Normalized concentrations NO_x of interacting flame puffs

Appendices

APPENDIX A: Igniter Setup and Description

Figure A-1: Igniter Photograph

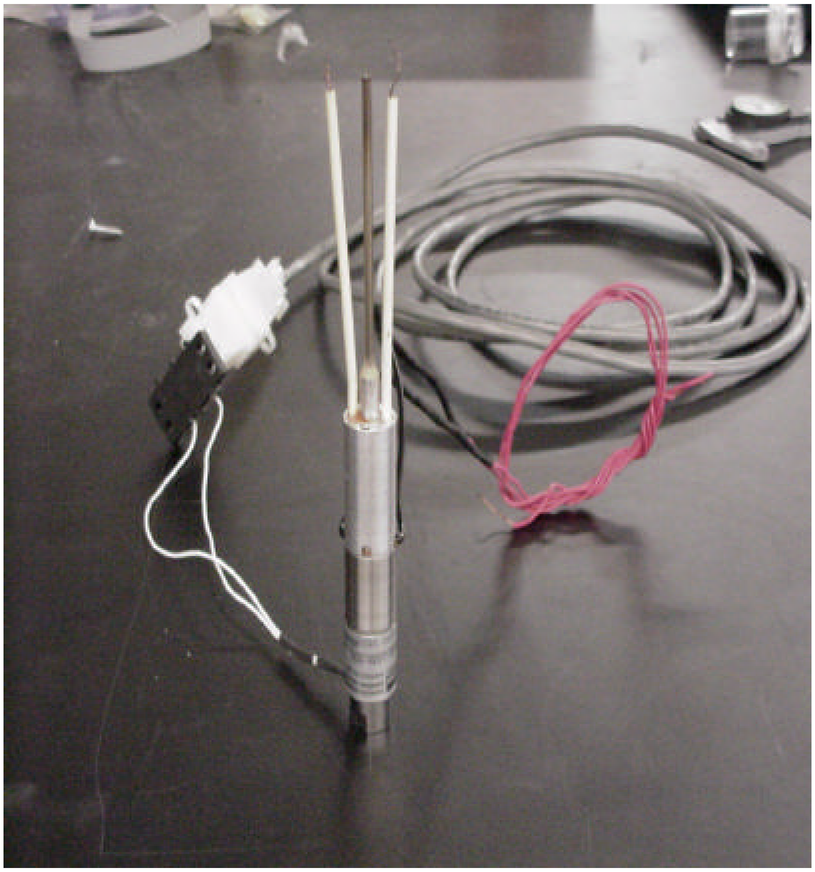

Figure A-2: Assembly Drawing

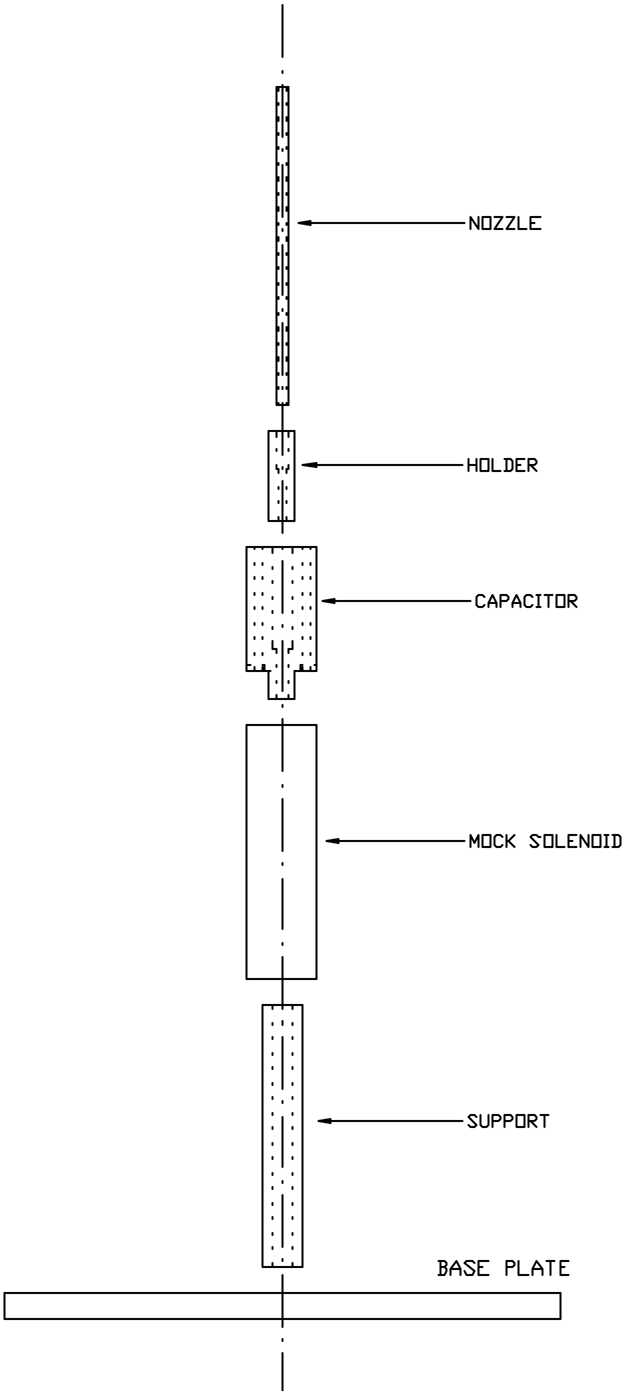

Figure A-3: Nozzle Holder Drawing

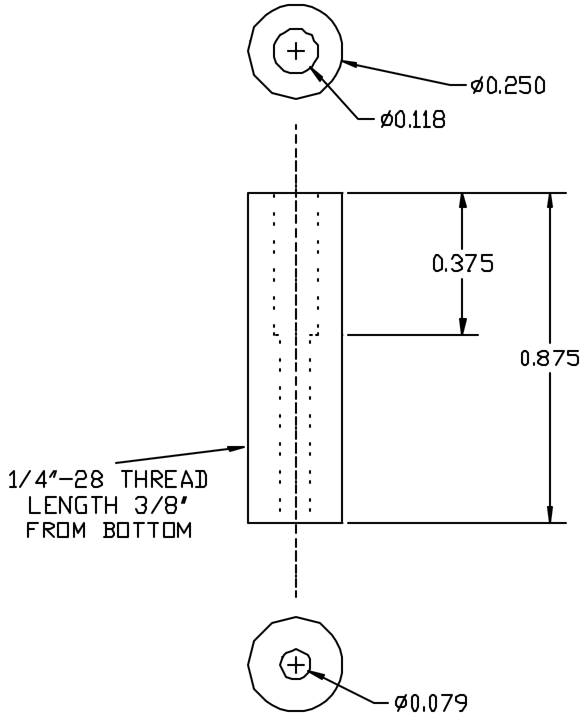

Figure A-4: Nozzle and Spacer Drawing

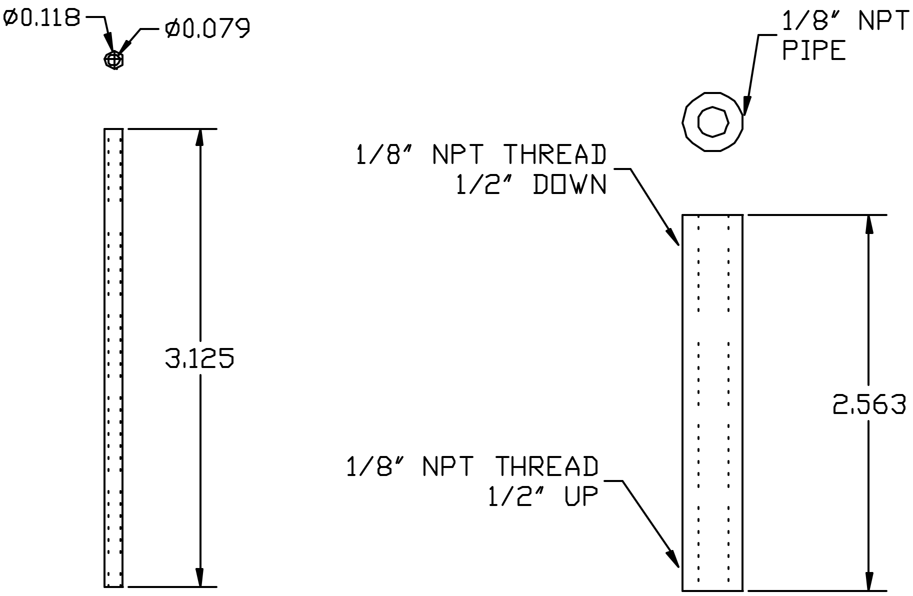

Figure A-5: Igniter Spacer Drawing

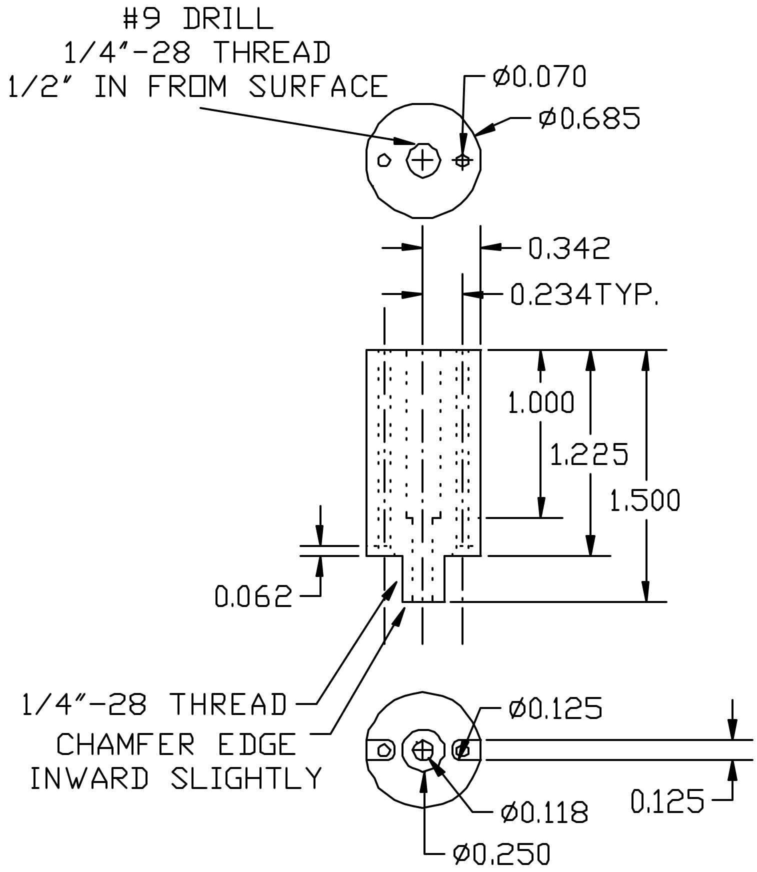

APPENDIX B: Gas Analyzers Flow Diagram

Figure B-1: UHC Analyzer Setup Schematic

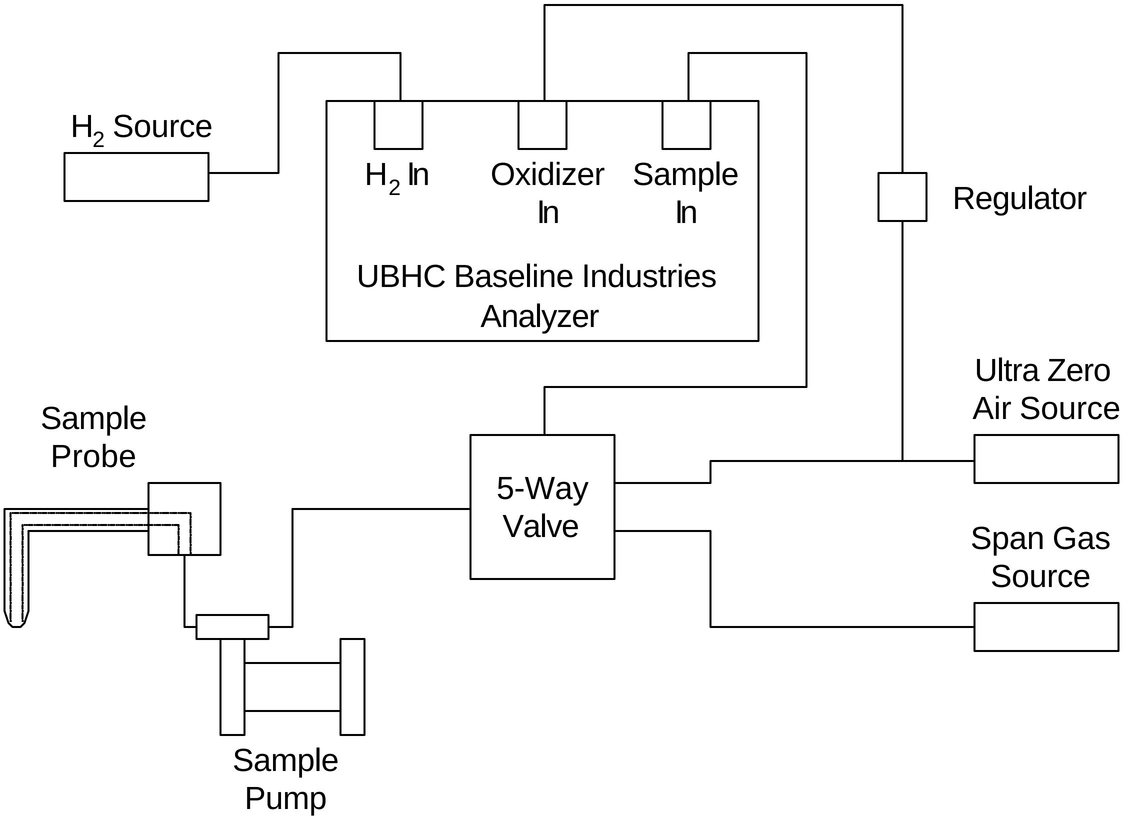

Figure B-2: NO_x / NO Analyzer Setup Schematic

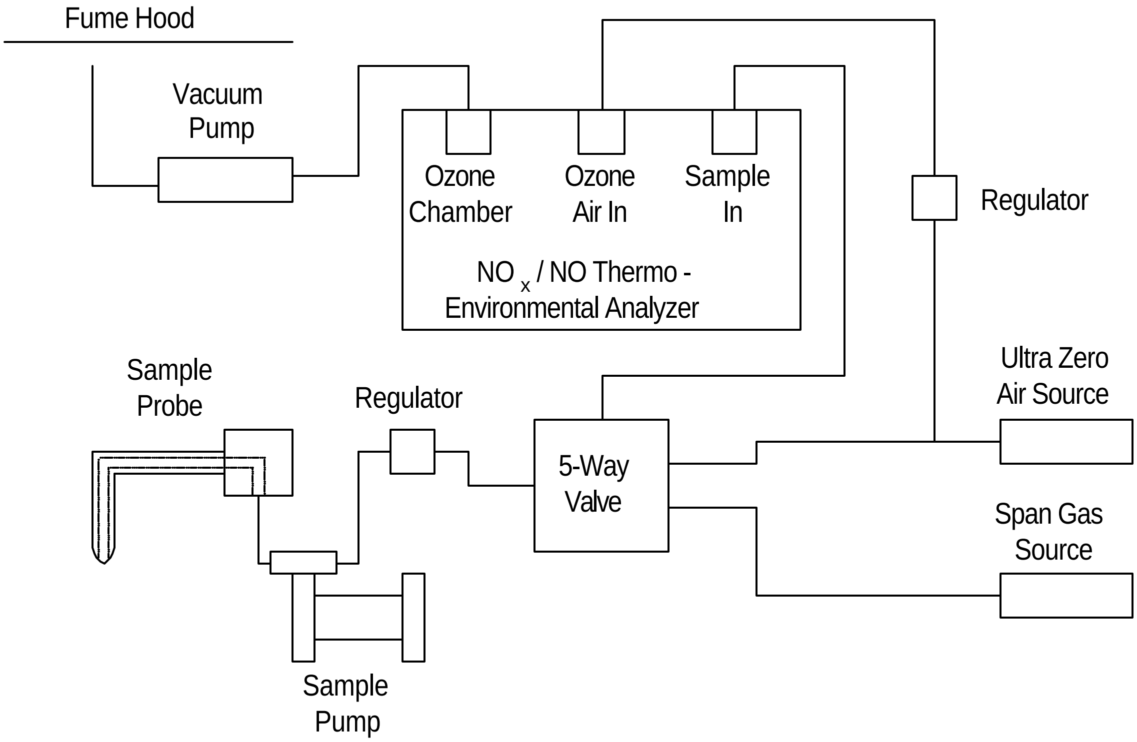

APPENDIX C: U_{cof} / U_{jet} vs. Actual Co-flow Rate

Figure C-1: Flow Rates For Re_{jet} = 3,000

U_{cof} / U_{jet} Values For Re_{jet} = 3,000				
Roto-Meter Reading (SCFM)	*Pressure Reading (psig)*	*Corrected Roto-Meter Reading (SCFM)*	*Co-Flow Velocity (ft/s)*	U_{cof} / U_{jet}
0	0.0000	0.0000	0.0000	0.0000
2	0.1224	2.0083	0.0753	0.0017
4	0.2792	4.0378	0.1514	0.0035
6	0.4704	6.0952	0.2286	0.0052
8	0.6960	8.1872	0.3071	0.0070
10	0.9560	10.3200	0.3870	0.0088
12	1.2504	12.5000	0.4688	0.0107
14	1.5792	14.7328	0.5525	0.0126
16	1.9424	17.0243	0.6385	0.0146
18	2.3400	19.3798	0.7268	0.0166
20	2.7720	21.8043	0.8177	0.0187
22	3.2384	24.3028	0.9114	0.0208
24	3.7392	26.8797	1.0081	0.0230
26	4.2744	29.5392	1.1078	0.0253
28	4.8440	32.2854	1.2108	0.0276
30	5.4480	35.1219	1.3172	0.0301
32	6.0864	38.0523	1.4271	0.0326
34	6.7592	41.0797	1.5406	0.0352
36	7.4664	44.2070	1.6579	0.0378
38	8.2080	47.4371	1.7791	0.0406
40	8.9840	50.7725	1.9042	0.0434

Figure C-2: Flow Rates For Re_{jet} = 5,000

U_{cof} / U_{jet} Values For Re_{jet} = 5,000

Roto-Meter Reading (SCFM)	*Pressure Reading (psig)*	*Corrected Roto-Meter Reading (SCFM)*	*Co-Flow Velocity (ft/s)*	U_{cof} / U_{jet}
0	0.0000	0.0000	0.0000	0.0000
2	0.1224	2.0083	0.0753	0.0010
4	0.2792	4.0378	0.1514	0.0021
6	0.4704	6.0952	0.2286	0.0031
8	0.6960	8.1872	0.3071	0.0042
10	0.9560	10.3200	0.3870	0.0053
12	1.2504	12.5000	0.4688	0.0064
14	1.5792	14.7328	0.5525	0.0076
16	1.9424	17.0243	0.6385	0.0087
18	2.3400	19.3798	0.7268	0.0099
20	2.7720	21.8043	0.8177	0.0112
22	3.2384	24.3028	0.9114	0.0125
24	3.7392	26.8797	1.0081	0.0138
26	4.2744	29.5392	1.1078	0.0152
28	4.8440	32.2854	1.2108	0.0166
30	5.4480	35.1219	1.3172	0.0180
32	6.0864	38.0523	1.4271	0.0195
34	6.7592	41.0797	1.5406	0.0211
36	7.4664	44.2070	1.6579	0.0227
38	8.2080	47.4371	1.7791	0.0243
40	8.9840	50.7725	1.9042	0.0261

APPENDIX D: NO and NO_x Additional Graphs

Figure D-1: NO average concentrations

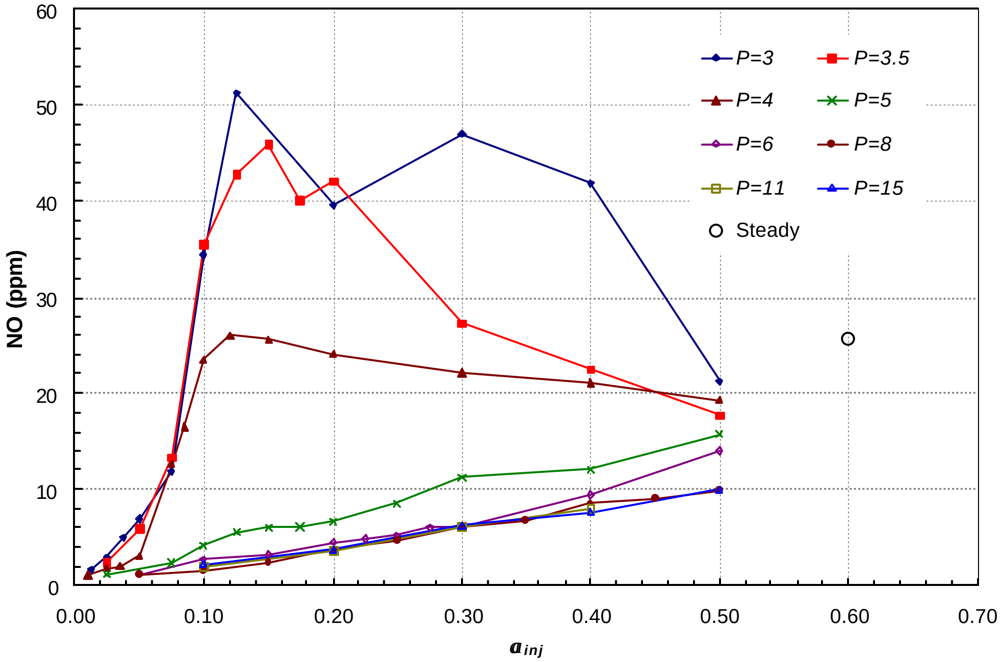

Figure D-2: NO_x average concentrations

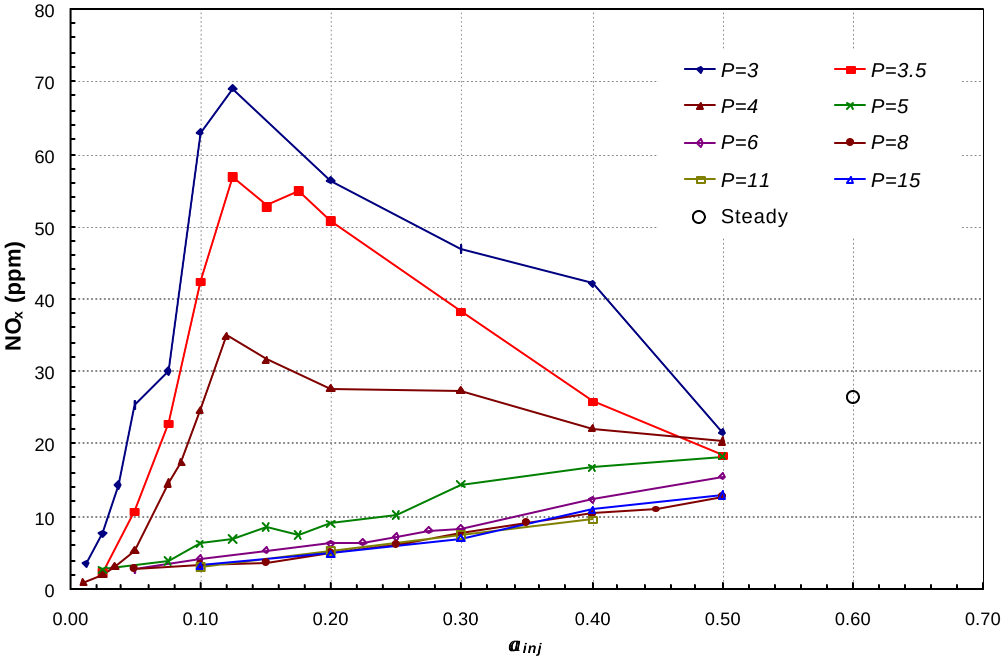

Figure D-3: Normalized NO$_x$ concentrations

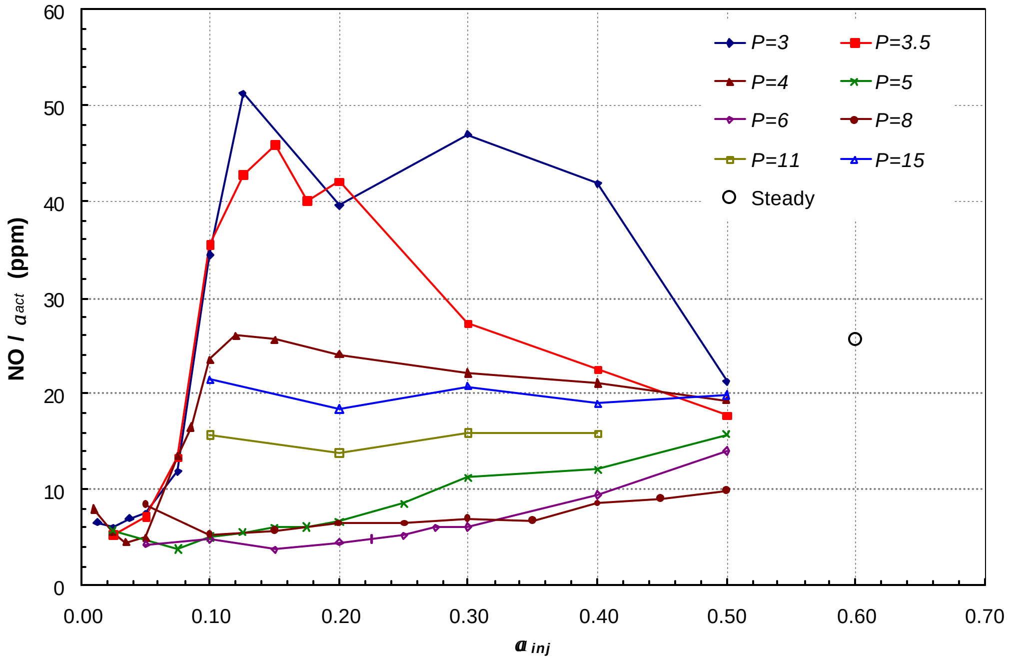

Figure D-4: Normalized NO$_x$ concentrations

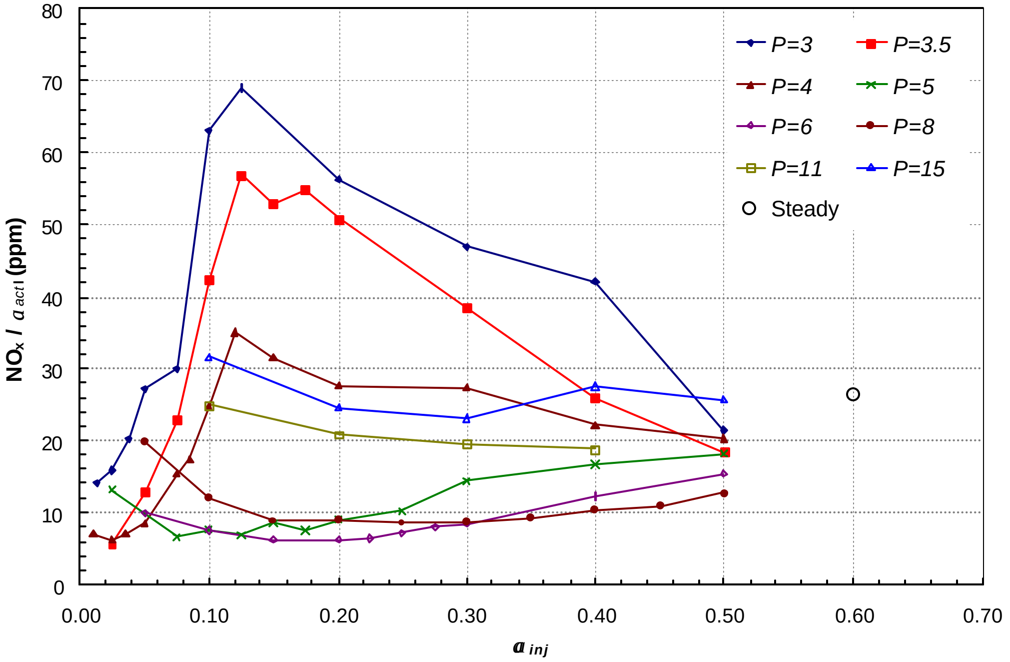

APPENDIX E: Injection / Actual Duty-Cycle Comparison

Figure E-1: Numerical Comparison of Injection and Actual Duty-Cycles

***P* = 3**		***P* = 3.5**		***P* = 4**		***P* = 5**	
a_{inj}	a_{act}	a_{inj}	a_{act}	a_{inj}	a_{act}	a_{inj}	a_{act}
0.0125	0.2445	0.0250	0.4215	0.0250	0.3147	0.0250	0.1927
0.0250	0.4771	0.0500	0.8247	0.0350	0.4375	0.0500	0.3850
0.0375	0.7031	0.0750	1	0.0500	0.6225	0.0750	0.5910
0.0500	0.9296	0.100	1	0.0750	0.9427	0.100	0.8157
0.0750	1	0.1250	1	0.0850	1	0.1250	1
0.1000	1	0.1500	1	0.1000	1	0.1500	1
0.1250	1	0.1750	1	0.1200	1	0.1750	1
0.2000	1	0.2000	1	0.1500	1	0.2000	1
0.3000	1	0.3000	1	0.2000	1	0.2500	1
0.4000	1	0.4000	1	0.3000	1	0.3000	1
0.5000	1	0.5000	1	0.4000	1	0.4000	1
				0.5000		0.5000	1

Figure E-1 cont.: Numerical Comparison of Injection and Actual Duty-Cycles

***P* = 6**		***P* = 8**		***P* = 11**		***P* = 15**	
a_{inj}	a_{act}	a_{inj}	a_{act}	a_{inj}	a_{act}	a_{inj}	a_{act}
0.0500	0.2782	0.0500	0.1372	0.1000	0.1215	0.1000	0.1000
0.1000	0.5469	0.1000	0.2771	0.2000	0.2550	0.2000	0.2000
0.1500	0.8509	0.1500	0.4197	0.3000	0.3797	0.3000	0.3000
0.2000	1	0.2000	0.5651	0.4000	0.5044	0.4000	0.4000
0.2250	1	0.2500	0.7132	0.5000	0.6492	0.5000	0.5000
0.2500	1	0.3000	0.8641				
0.2750	1	0.3500	1				
0.3000	1	0.4000	1				
0.4000	1	0.4500	1				
0.5000	1	0.5000	1				